2007

Advanced detection and separation methods: developments in surface-enhanced Raman scattering readout immunoassays and electrochemically modulated liquid chromatography

Betsy Jean Yakes
Iowa State University

Advanced detection and separation methods: Developments in surface-enhanced Raman scattering readout immunoassays and electrochemically modulated liquid chromatography

by

Betsy Jean Yakes

A dissertation submitted to the graduate faculty

in partial fulfillment of the requirements for the degree of

DOCTOR OF PHILOSOPHY

Major: Analytical Chemistry (Chemical Instrumentation)

Program of Study Committee:
Marc D. Porter, Major Professor
Patricia A. Thiel
Emily Smith
Andreja Bakac
Surya Mallapragada

Iowa State University

Ames, Iowa

2007

UMI Number: 3274821

ProQuest Information and Learning Company
300 North Zeeb Road
P.O. Box 1346
Ann Arbor, MI 48106-1346

TABLE OF CONTENTS

ACKNOWLEDGEMENTS iv

ABSTRACT vii

CHAPTER 1: General Introduction 1
DISSERTATION OVERVIEW 1
LITERATURE REVIEW 2
CONCLUSIONS 24
REFERENCES 24

CHAPTER 2: Detection of *Mycobacterium avium* subsp. *paratuberculosis* using Surface-Enhanced Raman Scattering: Part I – Sonicate Immunoassay 30
ABSTRACT 30
INTRODUCTION 31
MATERIALS AND METHODS 35
RESULTS 39
DISCUSSION 43
ACKNOWLEDGMENTS 45
REFERENCES 46
FIGURES 52

CHAPTER 3: Detection of *Mycobacterium avium* subsp. *paratuberculosis* using Surface-Enhanced Raman Scattering: Part II – Whole Cell Immunoassay and Protein Shedding 58
ABSTRACT 58
INTRODUCTION 59
MATERIALS AND METHODS 61
RESULTS 65
DISCUSSION 70
ACKNOWLEDGMENTS 72
REFERENCES 73
FIGURES 78

CHAPTER 4: Resonant Raman Labels for Improved Surface-Enhanced Raman Scattering Heterogeneous Immunoassays 85
ABSTRACT 85
INTRODUCTION 86
EXPERIMENTAL 89
RESULTS AND DISCUSSION 95
CONCLUSIONS 101
ACKNOWLEDGEMENTS 102
REFERENCES 102
FIGURES 104

CHAPTER 5: Electrochemically modulated liquid chromatographic separation of triazines and the effect of pH on their retention 115
ABSTRACT 115
INTRODUCTION 116
EXPERIMENTAL 118
RESULTS AND DISCUSSION 121
CONCLUSIONS 129
ACKNOWLEDGEMENTS 129
REFERENCES 129
FIGURES 132

CHAPTER 6: Conclusions 141

APPENDIX. Monolithic Carbon as a Novel Stationary Phase for Electrochemically Modulated Liquid Chromatography 144
INTRODUCTION 144
GLASSY CARBON PARTICULATE ROD 145
REDESIGNED EMLC COLUMN 146
MONOLITHIC CARBON 149
FUTURE DIRECTIONS 151
REFERENCES 152

ACKNOWLEDGEMENTS

When I graduated high school, I got the opportunity to encourage my classmates to "thank those who have helped you get here today." I am blessed to get to do so in my own life once again.

To list all the teachers and mentors who have influenced my life would take more space than I have here. Most specifically, thank you to Paul Roth, Carolyn Mottley, Kyle Strode, and Randy Robinson. I think I first fell in love with chemistry when Mr. Roth stated "Isn't that amazing!" during an in class color change demo and stayed in the field due to the exciting lectures, labs, and personal discussions with Dr. Mottley, Dr. Strode, and Dr. Robinson. To all of my teachers, your enthusiasm in chemistry and guidance has allowed me to become your colleague, and for that I am forever grateful.

Many thanks to the "Porterites." Marc, thank you for allowing me the freedom to pursue my research interests and guidance to help me become the scientist I am today. Bob Lipert, without your knowledge and patience much of this research would have stalled out long ago, the journey would have been far more difficult, and I would confuse singular and plural Latin forms more often. Thank you also to John Bannantine at the NADC for all of his insights on the MAP project and general encouragement during my graduate studies. Heather Bullen, thank you for always reminding me "It's a party!" Thank you, Becky, for always knowing what form I needed to fill out and exactly what I needed to hear to feel better – you're the best! My Arizona girls Jill and Karen, I can't imagine having done this without! Thank you to Jeremy Driskell who taught me everything I know about Raman (but any mistakes are truly my own). Thank you also to Jen and Mike Granger for all the words of

wisdom. My coffee and El Azteca cohorts, John and Rachel, thanks for the science talk and all the laughs!

Also, to the Physics kids (Shelbi, Raegan, Derek, Warren, Katie, and Larry). Thanks for all the fun times and distracting me from work. Looking forward to seeing you all soon (and might I add, Chemistry rocks!).

And of course, my family, how I ever got so lucky to have you all, I will never know. Thank you to my father, who probably has written a thesis in post notes over the last nine years. Looking forward to many more! I am so grateful to my mother who has always told me I could do it and has been a source of never ending support. Thank you for never doubting me and never letting me give up. To Melissa, Eric, and CJ – thank you for the "wine and whine" sessions and fashion advice. To Grandma and Grandpa Olsen, thank you for being excited about my research and the words of encouragement. To those who are no longer here to share this with me – Grandma Poskie and Lois – Thank you for all the times we shared and always believing in me.

My extended family – Ramona, Jim, Erin, Kellie, and Keenan – I am so thankful to be in your family, many thanks for all your support (and warm California vacations)! My friend Kathy, I am so glad that I took your tricycle back in preschool because then you were here with me through this journey from the start. My girl Emily, I am definitely ready for us to share a little of that "retail therapy" – thanks for being such a strong woman and supporting me being a nerd!

I dedicate this thesis to E. M. Pospychala, my grandfather and self proclaimed "#1 fan." Without your weekly letters in my early undergraduate years telling me you were with

me “win, lose, or draw”; your support through this graduate experience; and fun money, I would not be here today. Thank you.

And last, but never least, to my husband Michael. Thank you for always believing in me even when I didn’t believe in myself. Your encouragement and love is beyond what I could ever expect. Thank you for all the times you listened to me discuss my science, the many meals you brought to lab, so I could work late, and the support during my transition to ASU. I am so excited to start on the next journey with you!

This work was performed at Ames Laboratory under Contract No. DE-AC02-07CH11358 with the U.S. Department of Energy.

Finally, to all those who have helped me get here and to quote my grandfather (quoting Garrison Keillor), "Be well, do good work, and keep in touch."

ABSTRACT

This dissertation explores the use of novel detection methods for biological and chemical components commonly found in the environment. It encompasses two techniques: surface-enhanced Raman scattering (SERS) and electrochemically modulated liquid chromatography (EMLC).

Immunoassays using SERS as a readout tool have been developed in this laboratory and have shown low levels of detection (i.e., pico- to femtomolar and single binding event detection) for disease and biowarfare agents. This thesis seeks to further the performance of this platform for bacteria detection and explore strategies to increase the SERS response. Specifically, the first section of this dissertation focuses on the detection of a common, economically devastating, bovine bacterium. By the judicious design of the assay platform, a selective assay for the bacteria was developed, and low levels of detection (~500 bacilli/mL) were achieved. Further examination of these results led to the exciting discovery of an amplification phenomenon based on protein shedding from the surface of the bacteria. The last portion of the SERS readout immunoassay research focuses on fundamental studies employing resonant, dye molecules to create enhanced SERS signals. Full immunoassay results for four dyes, when compared with our standard, non-resonant reporter, yielded SERS signals ~300 times more intense. Implications of signal enhancement with respect to limits of detection are elucidated, and future work towards decreasing nonspecific binding briefly introduced.

The second part of this dissertation introduces research development in EMLC, specifically the use of mobile phase pH regulation and incorporation of novel stationary phases. By expanding upon current EMLC techniques, novel separations of weakly

basic/acidic compounds were achieved. These studies revealed the potential power of EMLC with mobile phase pH control to improve resolution while simultaneously reducing elution time for seven compounds. These results, which are in contrary to other reversed phase LC systems, are based on the ability to "pull apart" a chromatogram. In addition, the capability to perform a titration with EMLC, and thus determine the pK_a of a compound, is discussed in context of acid-base equilibria. This dissertation also introduces work underway for a redesigned column for testing monolithic carbon materials as an EMLC stationary phase. Finally, insights gained during this project are used to formulate further column redesign and in-situ monolith formation for improved EMLC separations.

CHAPTER 1: General Introduction

DISSERTATION OVERVIEW

This dissertation represents work aimed at advancing two areas of analytical chemistry. Detection of chemical and biological pathogens that cause illness and affect the environment is of the utmost importance not only for economic purposes but also for the improvement of life. This dissertation is organized into six sections. Chapter 1 starts with a discussion of detection techniques for bacteria, highlighting the advantages and disadvantages to each system. In addition, this literature review will introduce surface-enhanced Raman scattering (SERS) with emphasis on signal origin and instrumentation. Four original research chapters, each presented as a separate manuscript, and one appendix follow. Chapters 2 through 4 develop techniques for improving antigen detection, while Chapter 5 and the Appendix discuss investigations into electrochemically modulated liquid chromatography (EMLC) with respect to mobile phase and stationary phase composition.

As improvements in immunoassays and their detection methods have been pivotal in the advancement of bioanalytical science, the first three research chapters focus on important developments for a heterogeneous, two-site immunoassay.[1-3] In Chapter 2 and 3, this immunoassay is applied to the detection of *Mycobacterium avium subspecies paratuberculosis* (MAP). Current techniques to identify this bacteria lack the sensitivity, selectivity, or speed necessary for reliable detection. Specifically, the immunoassay optimization and results for MAP lysate are introduced in Chapter 2 through application of a recently developed antibody specific to a MAP surface protein.[4-6] Next, the assay system is further characterized, and a possible internal amplification mechanism for the heat-killed, whole cell bacteria is presented in Chapter 3. In Chapter 4, methods are developed for

incorporating resonance Raman molecules into extrinsic Raman labels (*ERL*s). The stable colloids are then used in a heterogeneous, two-site immunoassay for mouse IgG. Comparison of resonant versus nonresonant reporter molecules is made with enhancement factors, and limits of detection are evaluated.

Chapter 5 and the Appendix have introductions appropriate to their EMLC studies. As such, EMLC background will not be part of this literature review. Chapter 5 extends the versatility of EMLC by evaluating how mobile phase conditions, specifically pH, affect retention mechanisms and techniques developed are then applied to triazines, a class of harmful herbicides. After the Conclusions and Prospects section, the Appendix offers a brief introduction to monolithic stationary phases by focusing on their potential and challenges associated with their integration into a standard EMLC column.

LITERATURE REVIEW

Detection of Bacteria

The detection of pathogenic bacteria is crucial for identification of diseases in the healthcare, defense, food, and environmental arenas. In addition, by rapidly and correctly distinguishing the bacteria, appropriate measures to limit the spread of disease and actions to counteract infection can be taken. Analytical methods to detect, identify, and quantitate bacteria must be able to not only rapidly analyze a sample, but also do so selectively and sensitively. Moreover, because of the vast number of bacterial pathogens and varied areas where evaluation is needed, the techniques must be universally transferable to multiple bacteria types while also being cost effective. Finally, a low maintenance, continuous operation, easy-to-use system would be desirable.

The food industry accounts for the largest area of research in pathogen detection followed by the clinical, water, environmental, and defense fields.[7] In addition, the complexity of food matrices can complicate pathogen detection.[8] Many food borne illness events have made headlines in the popular press, with recent U.S. bacterial threats including *Escherichia coli* O157:H7 contamination in spinach (205 confirmed illnesses, three deaths)[9] and *Salmonella* tainted peanut butter (329 illnesses, 51 hospitalizations).[10]

In addition to the above pathogens, the human respiratory disease tuberculosis was recently a target antigen for detection studies in our research group. This organism is a part of the *Mycobacterium* genus which includes bacteria that cause the human ailments of leprosy and ulcers.[11, 12] In order to study this family of bacteria, a collaboration with the National Animal Disease Center (Ames, Iowa) was launched that employed *Mycobacterium avium subsp. paratuberculosis* (MAP). The pathogencity of MAP, a bacteria that is detected by a SERS-readout immunoassay in Chapter 2 and 3, has recently been reviewed.[13] Most importantly, this bacterium is responsible for Johne's disease which causes chronic enteritis of the intestines that leads to malabsorption of nutrients and death in cattle.

MAP can reside in domestic ruminants (e.g., cattle, sheep,[14, 15] and goats[16, 17]) and wildlife (e.g., deer,[18-20] antelope,[21, 22] bison,[23] and rabbits[24, 25]). Serological surveys conducted by the National Animal Health Monitoring System in 1996 and 2002 indicated that 20-40% of the U.S. cattle herds are afflicted at some level by MAP.[26, 27] In addition, it has been estimated that this disease imparts a economic loss of $220 million annually to the U.S. dairy industry,[27] with an overall impact of up to $1.5 billion to the U.S. cattle industry.[28] Furthermore, this disease is characterized by intermittent, low levels of bacterial shedding that can slowly contaminate the surrounding environment and lead to the spread of infection.

However, existing methods cannot reliably detect MAP at low levels. Many of the current detection techniques for this and other bacteria (e.g., *E. coli*, *Salmonella)* are introduced below with emphasis placed on the benefits and drawbacks of each method.

Traditional Methods

Clinical/Symptomatic Diagnosis. A hallmark of bacteria infection in humans, animals, or plants is symptoms that are associated with the particular disease. At the forefront of disease detection then is clinical diagnosis through visual inspection or simple medical tests. For example, in tuberculosis, a respiratory disease caused by *Mycobacterium tuberculosis*, a patient will experience chest pain, coughing, weight loss, and fever.[29] A medical professional will perform a routine examination to listen for fluid buildup in the lungs and obtain x-rays of the chest to look for abnormal cavities, lesions, nodules, or fibrotic scars that signify areas where bacteria have digested the tissue.[30] In the case of MAP infection, the animal will have rapid weight loss and chronic diarrhea during late stages of infection.[31] Clearly, symptoms in both diseases could be indicative of a variety of infections and many simple clinical procedures fall far short in yielding an exact diagnosis. Laboratory tests, like those introduced below, are common place and attempt to determine the bacteria type and strain in order to correctly identify the disease and implement treatment.

Smear Examination. Perhaps the simplest method of detection involves smearing a specimen (e.g., sputum, urine, pus, pleural, cerebrospinal or biopsy) onto a glass slide.[32] The slide can then be stained with an appropriate agent (e.g., auramine-rhodamine), viewed under a light microscope, and the number of bacteria enumerated (Figure 1).[30] While these tests are generally rapid and inexpensive, the results are based on characteristics shared by multiple

bacteria (e.g., acid-fast bacilli staining, size, and shape) and are therefore only confirmation of a genus of bacteria. In addition bacteria levels must be high enough to be enumerated, with 10^4 bacilli/mL necessary, for example, with the Ziehl-Neelsen method when applied to gram-positive rods of *Mycobacteria*.[30] For this reason, improvements in the identification of bacterium type are needed.

Figure 1: *Mycobacterium tuberculosis* (~3 μm rods) stained red in a sputum sample (from CDC, Public Health Image Library).

Culture and Colony Counting. Culturing a bacterial sample is the oldest and most popular detection technique. This standard method relies on growing a bacteria on a selective media, liquid or solid, that can either inhibit growth of non-targeted strains or that changes physical appearance (color or degradation) of the substrate due to growth of the specified colony.[33] Observation of colonies (e.g., size, shape, color, surface appearance, and odor) followed by enumeration (Figure 2) or optical density (OD) determination are used to classify bacteria type and evaluate the concentration. However, many of the criteria are subjective which can lead to errors in strain identification.[34] This technique, while well-established and sensitive, also suffers from long incubation (a few days to multiple weeks), with MAP requiring 12-16 wks.[35] In addition, colonies may grow on top of each other thus complicating identification and enumeration. If two or more bacilli produce indistinguishable colonies, gross underestimation of the actual concentration occurs. As such, results are designated as colony forming units (CFU) per mL instead of bacilli/mL.[32]

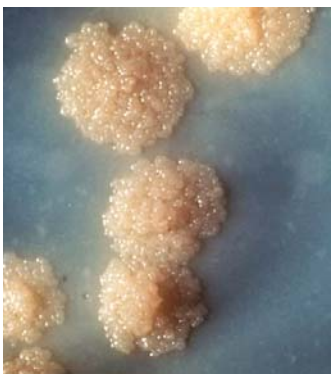

Figure 2: Colonies of *Mycobacterium tuberculosis* (from CDC, Public Health Image Library).

Advances that improve sensitivity and decrease incubation time include the use of radiometric labeling. For example, the BACTEC Radiometric System detects $^{14}CO_2$ that is given off as the bacteria grow on a radiolabeled, palmitic acid substrate.[36] While this method improves upon colony counting and is more rapid, the use of radioactive materials and high cost limit widespread use.[35] Recent advances towards the development of more specific, strain based tests that are sensitive and rapid are now beginning to displace these methods.

Recent Advances

Polymerase Chain Reaction (PCR). PCR was developed in 1985, and Kary Mullis received the 1993 Nobel prize for this invention.[37] Since then, this technique has been widely applied to detection of bacteria.[38] PCR is less time consuming than culturing, and when not including enrichment steps, takes only 5 to 24 h to produce results.[7] In this method, DNA is first extracted from the source and purified. The isolated DNA is denatured by heat and then amplified at a cooler temperature by specific primers and polymerization enzymes (Figure 3). These heating and cooling cycles are repeated several times, creating an exponential amplification of the original strand.[39] This material is then quantified, for example, through the use of gel electrophoresis, which in many cases is a detection technique on its own.[40] In gel electrophoresis, the charged fragments are subjected to an electrical filed that forces them to

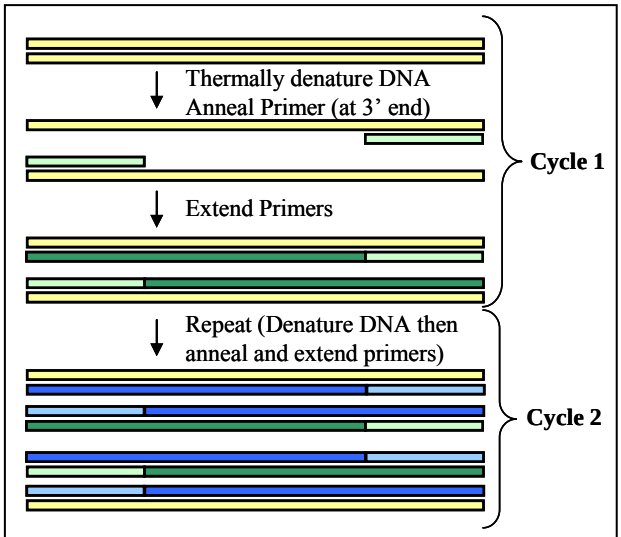

Figure 3: Basic PCR procedure, usually performed in a thermocycler.

move through the gel.[34] Different masses migrate at different rates, with smaller proteins moving faster through the pores of the gel.[41] This separation is detected by staining the fragments and comparing the bands to size standards.

Variations in this basic principle include real-time PCR, multiplexed PCR, and reverse transcriptase PCR (RT-PCR). In real-time PCR, the sample is interrogated by fluorescence measurements of dye-tagged DNA. These measurements are used to follow the progression of the amplification process since the signal intensity is proportional to the amount of product.[42, 43] RT-PCR has the ability to detect viable bacteria[7] and can be used without pre-enrichment steps,[44] although bacteria concentrations may need to be quite high (10^7 CFU/mL).[45] In multiplexed PCR, several DNA genes, corresponding to different bacteria, are amplified at the same time thus allowing for simultaneous detection of several pathogens.[46, 47] All PCR techniques have limitations[48, 49] and can lack specificity if the probe hybridizes with DNA from similar bacteria[50] or other proteins in a complex matrix. However, PCR can be strain specific and sensitive.

Gamma Interferon (INF-γ). In this recently developed procedure, whole blood is tested for an immunological response to a specific antigen. A blood sample is mixed with the antigen and incubated for a specified period of time, usually 24 h. If the person or animal is infected, T-cells in the blood will recognize the antigen and release INF-γ in response (Figure 4), which is measured by ELISA.[51] This test is becoming more integrated into medical laboratories, with a commercially available kit for tuberculosis serving as a recent example.[52] However, INF- γ tests suffer from false positives because of cross reactivity with similar bacteria.[53] Furthermore, Stabel and coworkers found that only 50 to 75% of cows in bovine herds that had low levels of MAP infection were identified when using an ELISA-based test

for INF-γ.[54] Other studies have found this method to be unreliable for people who have been vaccinated against the disease, young children[55] and calves under one year.[56, 57]

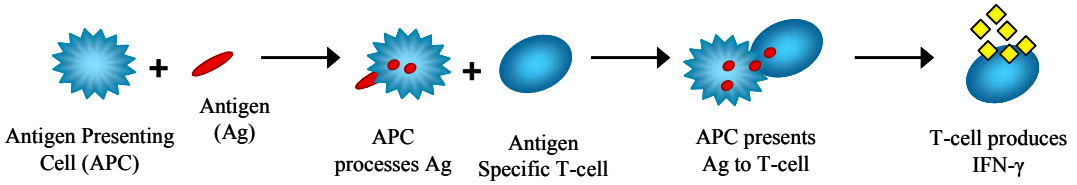

Figure 4: Premise of QuantiFERON® which tests for IFN-γ response to an antigen (adapted from Cellestis).

Other Methods. Common serological tests, including complement-fixation (CF) and agar gel immunodiffusion (AGID), have been commonplace in bacterial testing but are falling out of favor due to their lack of sensitivity.[58-60] Faster, more sensitive serological methods have been developed, including enzyme immunoassays that will be discussed in more detail later. In addition, flow cytometry has become a well accepted method for counting bacteria as well as determining the cell viability.[61, 62] By using a flow system in which bacteria are individually detected by a sensor, sensitive and rapid concentration measurements can be obtained. Cells are identified via fluorescent tags which can be based on a fluorophore-labeled antibody or viability stains.[63, 64] Viability stains (e.g., carboxyfluorescein diacetate for green fluorescence of viable cells and propidium iodide for red fluorescence of dead cells) lend an added dimension to classifying a sample. Other analytical instrumentation including chromatography and mass spectrometry, operating in solo or in tandem, are emerging as powerful techniques for separation and strain identification,[65] but hardware size and cost presently limit the widespread use of these techniques. Modern immunological methods, most specifically biosensors, are emerging as

competitive techniques through incorporation biorecognition elements for selectivity combined with the use of sensitive readout methods as discussed below.

Biosensors for Bacteria Detection

A newer area of bacteria detection utilizes biosensors that rely on antibodies or DNA probes to discriminate against interferences and cross reactivity found in the previous methods. The sensors are formed using well characterized immunoassay technology and then transduction is carried out through radiometric, optical, electrochemical, or other methods. The immunoassay platform will be briefly introduced, and then some of the most common readout techniques will be presented in this section.

Immunoassay Formats. Immunoassays represent a diverse area of biotechnology and have achieved widespread use due to the range of substances that are detected, the specificity that is enabled by the platform, and the sensitivity that is achieved with common detection methods.[66] Immunoassays were developed in the late 1950's by Berson and Yalow for the radiometric detection of insulin[67] and then in the early 1960's by Ekins for measuring thyroxine levels.[68] Many assay conformations and biorecognition elements are currently in use, but the general techniques consist of a competitive or noncompetitive format using an enzyme, antibody, or nucleic acid recognition element.

Two of the most common assays are shown in Figure 5. In the competitive immunoassay (Figure 5a), the analyte is mixed with labeled antigen, and the mixture is allowed to incubate with a capture substrate. The labeled antigen competes with the analyte for a limited number of binding sites, and after rinsing excess reagent, the signal for the labeled antigen is determined. Since the signal is inversely proportional to analyte

concentration, low analyte concentration yields a large signal. As a consequence, the detection limit is dominated by the affinity constant of the antibody with respect to the antigen and errors in measurement.[69]

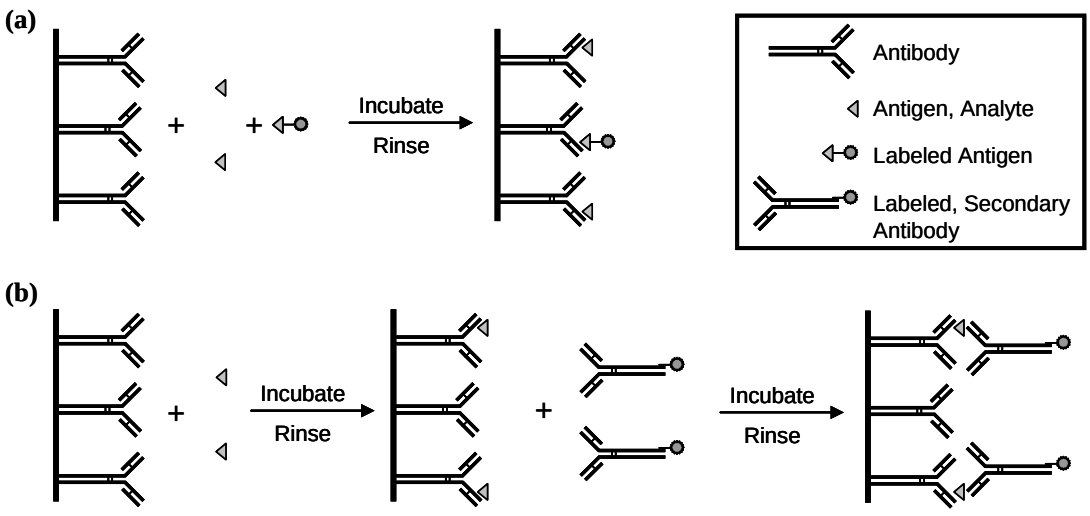

Figure 5: (a) Competitive and **(b)** Noncompetitive, two-site immunoassay formats.

In the noncompetitive immunoassay (Figure 5b), an excess of binding sites are available to potentially capture all available analyte. The antigen-antibody complex is then incubated with a secondary antibody containing the label. This sandwich, or two-site, immunoassay is read out with the signal directly related to analyte concentration. In this case, the detection limit is governed by the affinity constant of the antibody, experimental error, and signal intensity of the label. In theory, using a "brighter" label should lead to a more sensitive assay, with theoretical detection limits two orders of magnitude better than competitive immunoassays.[69] In practice, limits of detection can be hindered by the nonspecific interactions of the labeled antibody to the surface when no antigen is present. As expected, research continues to focus on approaches to minimize, and ideally eliminate, nonspecific binding through the use of surfactants, small proteins, blocking agents, or special surface coatings.

After optimization, the assay is carried out, and the antigen is quantified. In either the competitive or noncompetitive immunoassay, the scope of labels for readout is vast. The most common techniques are tied to enzymatic reactions, radiotracers, chromophores, or redox couples, and each will be explored further below.

Radiotracer Detection. Radioisotope detection is usually based on the isotopic labeling of an antibody. Commonly used radiotracers include ^{14}C, ^{3}H, ^{32}P, ^{35}S, and ^{125}I. Once labeled, the decay of the isotope is monitored and quantitated. While γ-rays (i.e., ^{125}I) or β-particles (i.e., ^{3}H or ^{14}C) can be employed, γ-emitters are more readily used because of their high penetrating power.[70] This method is not affected by environmental conditions or background from biological samples,[69] and the read out requires only a simple counter. However, radioisotopes are hazardous and have high disposal costs which, coupled with the performance of emerging techniques, have lead to a decline in usage.

Optical Detection Methods. There are many options for optical detection with enzymatic-generated chromophores and luminescence being the most common. Advances in surface plasmon resonance (SPR), quantum dots (QDs), and surface-enhance Raman scattering (SERS) are leading to the incorporation of these methods into immunoassay readout as well. Since SERS detection is used throughout this dissertation, it will be explored in a separate section.

In enzyme immunoassays, one of the most used approaches for pathogen detection is enzyme-linked immunosorbent assay (ELISA).[71, 72] In a typical sandwich ELISA, antibodies are immobilized on a platform (usually a microtitre plate), antigen is extracted from solution, and an enzyme-labeled antibody is then specifically bound to the captured antigen. When the system is exposed to the enzymatic substrate, a colored product is produced that has an

intensity proportional to the amount of antigen present.[73] Although ELISA may only takes a few hours to complete, it can suffer from poor sensitivity[74-77] which can be problematic during early stages of infection.[78] In addition, factors such as the pH, ionic strength, and temperature of the solution[69] affect assay performance and limit universal detection.

Luminescent methods have come to the forefront of quantification of analytes in immunoassays. Improvement in sensitivity and safety are achieved by using probes that absorb light energy at shorter wavelengths and emit at longer wavelengths (fluorescence), emit light during a chemical oxidation reaction (chemiluminescence), or naturally produce light (bioluminescence). These quantitative methods can achieve detection limits on the order of 10^{-12} M.[79] Nonetheless, the instrumentation is more complex than radioisotope detection with the need for a light source, filters or monochromators, lenses, and detectors. While these readout methods are popular, there are limitations to their utility. In general, the chromophores have broad emission peaks that complicate their use in multiplexed scenarios. In addition, biological samples have a fluorescence background and scatter incident radiation thus interfering with the analytical signal. Furthermore, quenching of fluorescence and photobleaching are commonplace.[69]

A new area of optical detection employs SPR sensors. When incident light is at a specific wavelength and angle, an evanescent electromagnetic field is produced at the surface of a thin metal. By scanning the incident angle and monitoring the reflected light intensity, a minimum reflectivity occurs when the light is coupled to the surface plasmon oscillation.[80] This condition is sensitive to the dielectric properties of the surface which are affected by a surface immobilized species. Shown in Figure 6 is a simplified schematic of a common SPR sensor configuration. In this case, a gold surface/prism interface contains adsorbed antibodies

that can extract antigen from flowing solution.[81] The binding of antigen to the sensor chip results in a change in the refractive index of the metal/dielectric interface which is detected as a shift in the resonance angle.[82] This optical method is then label-free, yielding a change in signal upon antigen capture. In addition to its use in label-less, real time analysis, SPR sensors have limits of detection ranging from ppb and nanomolar levels to 10^4 organisms/mL.[80] Disadvantages arise from refractive index changes that are not due to the desired complex formation and can include false-positives due to nonspecific binding, solution inhomogeneity, or temperature fluctuation. Furthermore, as the sensitivity is based on changes in refractive index at the sensor, small molecules pose a greater challenge.[73]

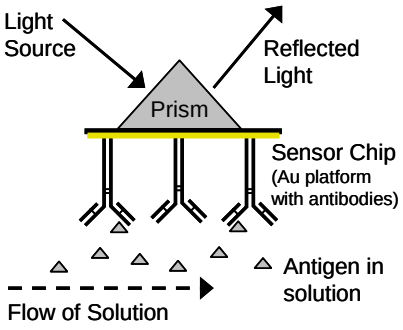

Figure 6: Basic SPR, flow channel sensor that detects antibody-antigen binding by measuring changes in the reflected light.

Another recent advancement in detection stems from the use of quantum dots. QDs are composed of semiconductor nanocrystals, with the CdSe-ZnS core-shell being very popular, that are used as the label in immunoassays.[83] These photostable nanoparticles are highly luminescent, and their emission maximum to lower energies as the size increases.[84] In addition, these particles have bands that are both narrower and more intense than common molecular fluorophores. In addition, the size of the particles can be tuned for multiplexing. When incorporated into an assay, detection limits rival many of the available techniques, with 10^4 CFU/mL levels reached for the concurrent readout of *E. coli* and *Salmonella* in only 2 hours.[85] The biggest drawback to this technology has been the lack of biocompatible semiconductor surfaces,[86] though advances in this area to coat and stabilize the QDs[87] are ongoing.

Electrochemical Detection. Two general categories of electrochemical biosensors exist. The first is based on biocatalysis, while the second method is focused on affinity sensors.[88] In the former method, an enzyme is coupled to an electrode through polymer entrapment, surface adsorption, covalent binding, electrostatics, or biospecific interactions. When an antigen is present that reacts with an enzyme-labeled antibody, an electrochemical response is detected. This technique is generally limited by the ability to create a stable layer of the enzyme. In the case of affinity biosensors, the immobilization of antigen and antibody follow the general procedures used in immunoassays. The detection is usually performed by interrogating a sample that has either an electrochemically tagged antigen (competitive) or antibody (noncompetitive).[88]

After performing an assay, the ensuing change in current, potential, or impedance can be measured.[73] In amperometric methods, the antigen concentration is linearly related to current, but this trend is an indirect measurement of an enzymatic reaction. With potentiometeric transducers, a logarithmic concentration response is often obtained, but this easy-to-use system can suffer from electrode fouling and low sensitivity. Impedimetric techniques can be used for real-time, label-free capacitance measurements due to changes in the thickness and dielectric properties of the electrode. These methods benefit from rapid readout of antigens while using inexpensive instrumentation. In addition, it is sometimes possible to work in turbid environments or repeat measurements,[73] but these benefits are only possible when electrode fouling does not occur in the case of the former, and the sample/redox chemistry is marked by reversibility in the latter situation. Furthermore, electrochemical methods can be limited by low sensitivity due to nonspecific interactions and interferences from other solution components.[7]

Other Developments. The application of other technologies to the advancement of pathogen detection has been vast. In addition to those methods outlined above, force, magnetic, and mass detection methods have been researched. Atomic force microscopy and functionalized microcantilevers can be used to evaluate intermolecular interactions and immunosensors.[89] Also, techniques that rely on scanning probe microscopy can be used to visually interrogate a sample substrate and enumerate the number of antigens bound.[90] Giant magnetoresistance technology, commonly found in computer hardrives, has been applied to detection of magnetically labeled antigens.[91] Furthermore, as piezoelectric devices advance, the direct detection of bacteria due to specific binding to a platform and then measuring the frequency change (based on mass accumulation) is being explored.[92]

Many of the techniques currently being developed involve combining multiple methods or implementing advanced sample preparation prior to detection. With respect to the former, research is expanding upon using PCR to first copy the DNA present in a sample and then applying this amplified solution in an assay with common readout technologies to further improve limits of detection. For the latter, one area of growing research is the application of immunomagnetic beads for separation and concentration of antigens.[7] Another technique utilizes antibody-coated paramagnetic beads to extract the analyte from solution prior to detection.[63]

Surface-enhanced Raman Scattering (SERS)

Raman Background. When particles have dimensions comparable to or smaller than an incident electromagnetic field and are randomly distributed in a medium of differing refractive index light scattering can occur. An induced secondary emission takes place from a

subtle distortion when the positively charged nuclei of a molecule are attracted toward the negative pole of the incident radiation, and the electrons are attracted toward the positive pole.[93] This charge separation produces an induced dipole in the particle and secondary, elastic radiation. Another type of light scattering was first observed by C.V. Raman in 1928.[94, 95] Named Raman scattering on his behalf, this inelastic scattering is characterized by frequency shifts that are independent of the scattering angle and are based on vibrational or rotational transitions in a molecule.

The photon origin of this process is illustrated in Figure 7. When an incident photon is adsorbed by a molecule into a virtual state, the excited electron can either relax by scattering elastically (Rayleigh) or inelastically (Raman). Raman scattering is much weaker (10^{-6} of the incident radiation intensity) than the Rayleigh scattering and has a frequency of the original photon shifted with respect to the vibrational frequency of the molecule/functional group. At room temperature, the Stokes lines are more intense than the anti-stokes lines because the ground-state population is greater than that of the excited state.[93] It is therefore more customary to measure the Stokes side of the spectrum.

The closer the virtual state is to a real energy level, the higher the adsorption probability. When the virtual state approaches the lowest excited electronic state, pre-resonance is achieved. When the frequency of an incident photon lies within the contour of an electronic adsorption band, resonant Raman scattering is obtained. This higher adsorption probability leads to a larger number of scattered electrons and stronger Raman signals.[96]

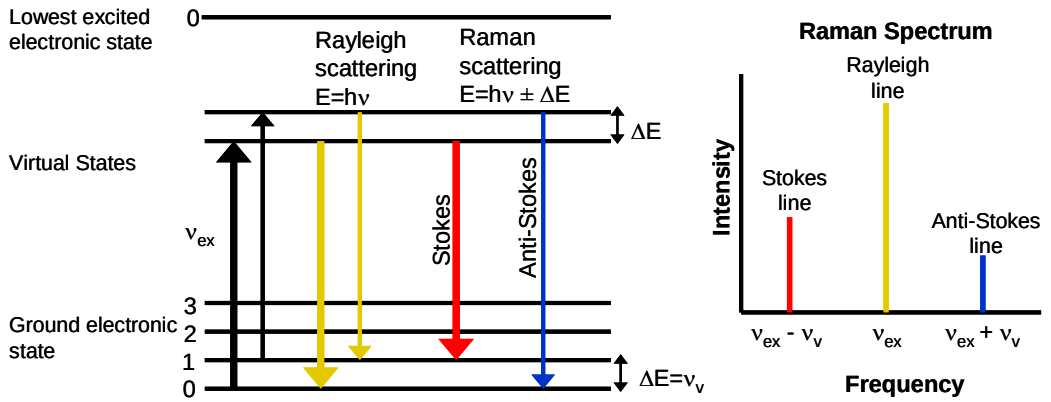

Figure 7: Photon origin of Rayleigh and Raman scattering.

Classic theory leads to an equation to define the Raman effect:

$$\mu_{in} = \alpha_0 \mathbf{E}_m \cos(2\pi\nu_{ex}t) + \frac{\mathbf{E}_m r_m}{2}\left(\frac{\partial\alpha}{\partial r}\right)_e \cos 2\pi(\nu_{ex}+\nu_\upsilon)t + \frac{\mathbf{E}_m r_m}{2}\left(\frac{\partial\alpha}{\partial r}\right)_e \cos 2\pi(\nu_{ex}-\nu_\upsilon)t \quad \textbf{(1)}$$

with μ_{in} the induced dipole of a polarizable molecule, α_0 the polarizability at equilibrium, $\mathbf{E}_m$ the amplitude of the incident wave, ν_{ex} the excitation frequency, t the time, r_m the maximum bond separation, and ν_υ the vibrational frequency.[93] This expression leads to the three scattering events, with the first term representing the Rayleigh line and the second and third terms representing the anti-Stokes and Stokes lines, respectively. Equation 1 also shows that for a mode to be Raman active there must be a change in polarizability at the equilibrium bond distance.

In addition, Raman intensities can be characterized by:

$$\Phi_R \propto \sigma(\nu_{ex})\nu_{ex}^4 E_0 n_i e^{-E_i/kT} \quad \textbf{(2)}$$

which defines the radiant power (Φ_R) with respect to Raman scattering cross section $\sigma(\nu_{ex})$, source irradiance as E_0, number density in the initial state as n_i, and the Boltzmann factor as the exponential term. As the signal strength is based on irradiation intensity, laser sources have become popular. Also, with intensity proportional to the fourth power of the laser

frequency (ν_{ex}), using short wavelength (i.e., UV) lasers can be advantageous. In addition, increasing the cross section leads to more intense signals, so methods to optimize this term have been considered. However, even when optimizing these conditions, Raman is a weak spectroscopic technique not applicable to detection limits demanded by immunoassays. The advent of SERS opened the door toward a more feasible use of Raman scattering for immunoassay detection.

SERS Theory. In 1974, Fleishman and coworkers observed large Raman signals when pyridine was adsorbed at the surface of electrochemically roughened silver electrodes.[97] However, they described the intensities as being due to a high number of adsorbates. Independently, Jeanmarie and Van Duyne[98] and Albrecht and Creighton[99] proposed that the signals were not merely due to surface concentration and defined the phenomenon as SERS. This enhancement occurs when the incident radiation couples with the localized surface plasmon oscillation of a coinage metal surface (e.g., gold, silver, or copper) and is also dependent on the shape, asperity size, and dielectric properties of the material.[100, 101]

Raman scattering can be described by the simple equation of:

$$\mu_{in} = \alpha \mathbf{E} \qquad \textbf{(3)}$$

where the induced dipole moment (μ_{in}) is proportional to the product of the polarizability (α) and the electric field (**E**). In order to obtain enhanced signals, the electric field and/or polarizability must be increased. These two aspects lead to the basis of SERS theoretical mechanisms which are a combination of chemical (increase in α of the molecule) and electromagnetic enhancements (increase in **E** at a surface) that experimentally yield enhancements of 10^6 to 10^8. The chemical enhancement mechanism is based on short ranged

effects and has a smaller contribution (100 times) to the overall enhancement. The two main models, adatom[102] and charge-transfer,[101, 103] are based on an increase in the polarizability of the molecule as a consequence of adsorption onto a metal surface.[104] Many contributions to the electromagnetic theory extist,[101, 105-107] and all are based on enhanced local electric fields experienced by the Raman active molecule and account for at least 10^5 enhancement. The image field model,[108] surface field calculations,[109] and distance dependence[107] of d^{-12} have been recently reviewed by Driskell *et. al*.[110]

In SERS, the signal intensity is a combination of effects represented by:

$$I_{SERS}(\nu_{sc}) = N' \times I(\nu_L) \times A(\nu_L)^2 \times A(\nu_{sc})^2 \times \sigma_{adsorbed} \quad \textbf{(4)}$$

with the number of adsorbates (N') and the cross section ($\sigma_{adsorbed}$) leading to the chemical enhancement and the laser field enhancement $A(\nu_L)$ and the scattered field enhancement $A(\nu_{sc})$ contributing to the electromagnetic effects.[111] Based on equations 2 through 4, increasing the molecular parameters of polarizability or Raman scattering cross section would further increase the intensity of scattered radiation. This situation is the case with resonant molecules because there is a large change in molecular geometry during the electronic transition.[93, 96] This method is the basis of Chapter 4 for achieving detection limits of 10^{-12} M.

SERS Instrumentation

Recent advances in Raman instrumentation are allowing for highly portable, low cost instruments that yield high sensitivity. Previously, Raman instrumentation required high power lasers, double and triple monochromators, specialized detectors, and vibration isolation at costs and sizes that complicated field deployment. With the advent of fiber optics,

diode lasers, improved optical filters, and advanced array detectors, Raman spectroscopy is now taking its place in modern analytical equipment with applicability to varied environments at affordable costs.[112]

General Components. A Raman instrument consists of a laser source, a sample cell or platform, a wavelength selector, a radiation transducer, and a signal processor/readout system.[93] The selection of the laser source is highly dependent on the sample, with helium-neon (632.8 nm), argon ion (488.0, 514.5 nm), and krypton ion (530.9, 647.1 nm) lasers being among the most widely used. In addition, deep-UV lasers are coming into popularity for resonance measurements of biological samples,[113] along with diode lasers for low-cost and versatility.[114] As Raman theory states (Equation 2), the scattered intensity increases with respect to ν_{ex}^4, so using lower wavelength lasers can yield higher signals. However, red laser light from a HeNe laser, for example, can be used to reduce fluorescence background from some samples. In addition, if a sample is photosensitive, the wavelength of the laser and power density in the irradiated sample area must be considered. As a rule, the best choice is a compromise between high signal intensity, low interference (fluorescence), and minimal photodegradation.

As Raman spectroscopy is amenable to many sample states (solid, liquid, or gas), the cells and platforms are quite varied.[93] For liquid samples, capillary tubes or cuvettes made of glass or quartz are generally used, with research into design flow-through systems underway in many groups.[115-117] An advantage of Raman over other vibrational spectroscopy techniques (i.e., IR) is that water is a very weak Raman scatterer, so measurements can be made in aqueous solutions thus allowing *in situ* studies of biological samples. Solid powders

can be placed in standard capillary tubes, in potassium bromide pellets, or on a level platform.

Wavelength selectors in Raman spectroscopy are employed to achieve a spectral resolution on the order of 5 cm^{-1} and to separate the weak Raman lines from the intense Rayleigh radiation. For this purpose, double or triple monochromators with ruled gratings have been incorporated into Raman instrumentation. Advances in holographic grating technology, as well as improvements in filters, have allowed simplification of Raman instrumentation and greater signal throughput. While traditional Raman instrumentation uses photomultiplier tubes or dc signal processing, diode arrays are becoming popular for their rapid and complete spectrum acquiring capabilities. Other advances in Raman instrumentation include the combing techniques such as Raman microprobes[118] in which a spectrometer is combined with optical microscopy and Fourier transform Raman spectroscopy.[119]

NanoRaman^{TM}I. In our laboratory, the standard Raman instrument is a NanoRaman^{TM}I. This instrument, manufactured by our collaborator Concurrent Analytical and shown in Figure 8, consists of no moving parts and is light weight (14 lbs, 16×8×8 in. footprint), which allows integration into many laboratory and industrial settings.

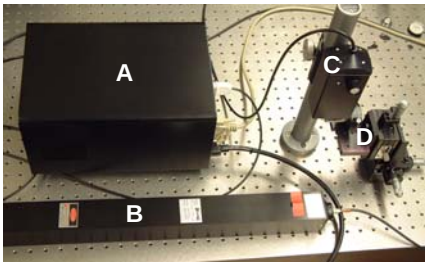

Figure 8: NanoRamanTMI configuration with the spectrometer (A), HeNe laser (B), fiber probe head (C), and sample platform (D) on an optical table with 1" between holes.

The light source is a 30 mW HeNe laser with a wavelength of 632.8 nm. To transmit the laser excitation and collect the scattered radiation from the sample, a bifurcated fiber optic cable (50 μm) is attached to a fiber-optic probe head (Figure 9). The laser light enters

the fiber and is collimated by a spherical lens. After traveling through a bandpass filter (OD 4) that removes any spontaneous Raman or fluorescence from the fiber but passes the laser wavelength, the light is sent through a mirror and focused onto the sample via an objective. The objective can either be set for solution measurements (numerical aperture (NA) of 0.40 and working distance (WD) of 6.24 mm) or solid substrate detection (NA of 0.68 and WD of 3.1 mm). With the latter objective, a 25-μm diameter laser spot size is incident on the substrate with a power of ~3 mW. The scattered radiation that is then collected reflects off a gold-coated mirror and is sent through a longpass filter (OD 6) that rejects the Rayleigh and anti-Stokes scattering. The Stokes scattered radiation is then collimated and transferred to the spectrometer.

The spectrograph is an *f*/2.0 Czerny-Turner imaging spectrometer as shown in Figure 10. Light enters from the 50-μm diameter fiber and is collimated by the first achromat. The gold mirrors that follow are used to optimize the scattered radiation angle to the grating and allow the system to be compact. After passing through another achromat to remove chromatic aberration, the scattered radiation reaches the detector, a thermoelectrically cooled (Kodak 0401E) charge coupled device that has a spectral resolution of 6 to 8 cm^{-1} (2 cm^{-1}/pixel). This small chip (8.4×5.5 mm) has a low dark current (less than 10 pA/cm^2 at 25°C) and has high signal collection. Spectral integration times can be varied with most acquisitions at one second, controlled by a PC with Windows Visual Basic program.

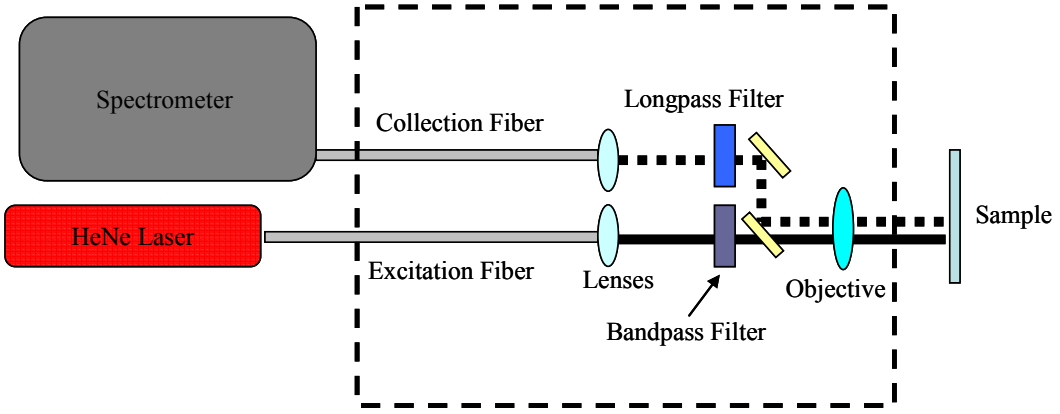

Figure 9: Schematic of instrument configuration with fiber optic probe head optics shown in black dashed box.

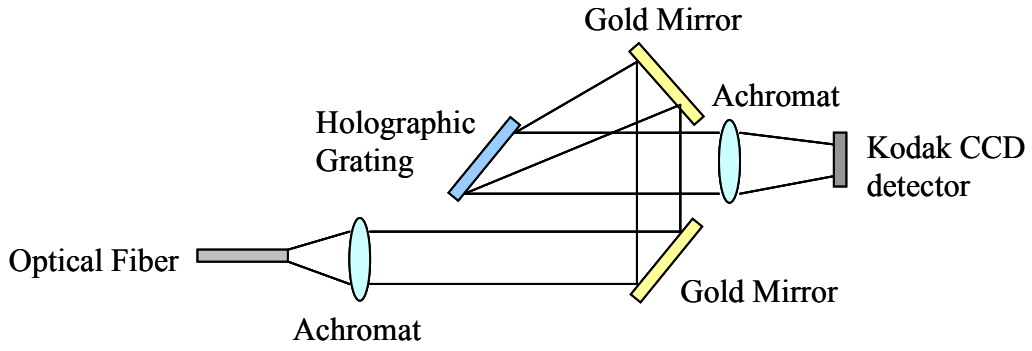

Figure 10: Modified Czerny-Turner imaging spectrometer.

As a final consideration for this instrumentation, CCD performance was evaluated for linearity throughout the dynamic range of the detector. For the current system, the CCD becomes nonlinear when it reaches half-capacity (Figure 11a), and a simple equation can be used to determine the percentage that the observed signal deviates from the true signal (Figure 11b). This model can be to used better evaluate antigen concentration, especially for the intense Raman scatters that were investigated in Chapter 4 where the signal reported by the CCD can be adjusted to the actual value of scattering.

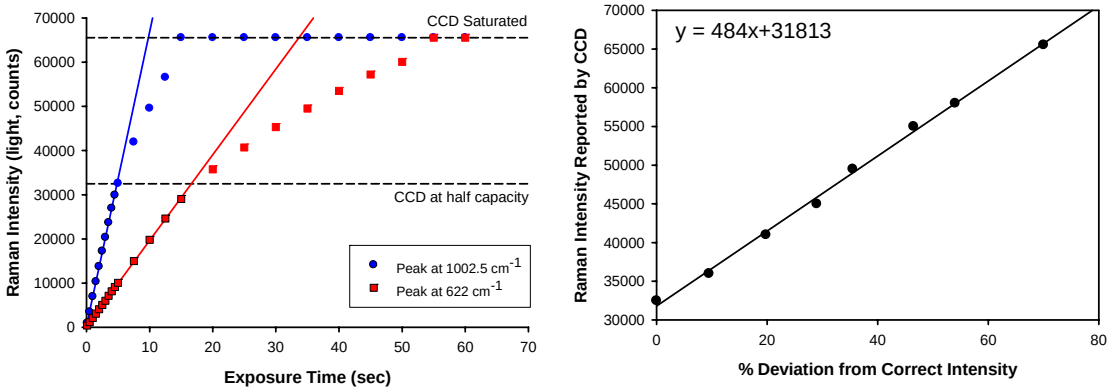

Figure 11: Evaluation of CCD performance. **(a)** Raman light signal in counts obtained a various exposure times observed for two peaks of a solid polystyrene standard with **(b)** the corresponding percent deviation from expected intensity. (Data taken and evaluated by B. J. Yakes)

CONCLUSIONS

In conclusion, many modern techniques can be used to develop sensitive, selective, and rapid detection methods for interrogating bacteria laden samples. Evaluation of these pathogens is important in multiple fields, with food safety and disease detection the motivation for research presented in this dissertation. At the forefront of the most recent advances, SERS-readout of two-site immunoassays has recently been developed and has been shown to allow for low levels of detection. In addition, SERS instrumentation offers the reliability, sensitivity, and ease-of-use demanded by laboratories and industry. With these considerations in mind, continued research and improvement could allow this technique to be integrated in diagnostic laboratories and field-monitoring for the screening of bacteria leading to timely measures for containment of contamination and correct therapeutics for those infected.

REFERENCES

(1) Driskell, J. D.; Kwarta, K. M.; Lipert, R. J.; Porter, M. D.; Neill, J. D.; Ridpath, J. F. *Anal. Chem.* **2005**, *77*, 6147-6154.

(2) Grubisha, D. S.; Lipert, R. J.; Park, H.-Y.; Driskell, J.; Porter, M. D. *Anal. Chem.* **2003**, *75*, 5936-5943.
(3) Ni, J.; Lipert, R. J.; Dawson, G. B.; Porter, M. D. *Anal. Chem.* **1999**, *71*, 4903-4908.
(4) Bannantine, J. P.; Baechler, E.; Zhang, Q.; Li, L.; Kapur, V. *J. Clin. Microbiol.* **2002**, *40*, 1303-1310.
(5) Bannantine, J. P.; Huntley, J. F.; Miltner, E.; Stabel, J. R.; Bermudez, L. E. *Microbiology* **2003**, *149*, 2061-2069.
(6) Bannantine, J. P.; Radosevich, T. J.; Stabel, J. R.; Berger, S.; Griffin, J. F.; Paustian, M. L. *Clinical and Vaccine Immunology* **2007**, *in press*.
(7) Lazcka, O.; Del Campo, F. J.; Munoz, F. X. *Biosens Bioelectron* **2007**, *22*, 1205-1217.
(8) Feng, P. C. H. *ACS Symposium Series* **2006**, *931*, 14-27.
(9) FDA *Finalizes Report on 2006 Spinach Outbreak*
U. S. Food and Drug Administration News, http://www.fda.gov/bbs/topics/NEWS/2007/NEW01593.html. accessed: May 5, 2007
(10) FDA *Update on Salmonella Outbreak Linked to All Peter Pan Peanut Butter and Certain Lot Numbers of Great Value Brand Peanut Butter*, U. S. Food and Drug Administration News, http://www.fda.gov/bbs/topics/NEWS/2007/NEW01569.html. accessed: May 5, 2007
(11) Oliveira, M. S.; Fraga, A. G.; Torrado, E.; Castro, A. G.; Pereira, J. P.; Longatto Filho, A.; Milanezi, F.; Schmitt, F. C.; Meyers, W. M.; Portaels, F.; Silva, M. T.; Pedrosa, J. *Infection and Immunity* **2005**, *73*, 6299-6310.
(12) Scollard, D. M.; Adams, L. B.; Gillis, T. P.; Krahenbuhl, J. L.; Truman, R. W.; Williams, D. L. *Clinical Microbiology Reviews* **2006**, *19*, 338-381.
(13) Chacon, O.; Bermudez, L. E.; Barletta, R. G. *Annual Review Microbiology* **2004**, *58*, 329-363.
(14) Lambeth, C.; Reddacliff, L. A.; Windsor, P.; Abbott, K. A.; McGregor, H.; Whittington, R. J. *Aust Vet J* **2004**, *82*, 504-508.
(15) Muskens, J.; Bakker, D.; de Boer, J.; van Keulen, L. *Vet Microbiol* **2001**, *78*, 101-109.
(16) Storset, A. K.; Berg, I.; Djonne, B. *Vet Immunol Immunopathol* **2005**, *107*, 87-94.
(17) Storset, A. K.; Hasvold, H. J.; Valheim, M.; Brun-Hansen, H.; Berntsen, G.; Whist, S. K.; Djonne, B.; Press, C. M.; Holstad, G.; Larsen, H. J. *Vet Immunol Immunopathol* **2001**, *80*, 271-287.
(18) Godfroid, J.; Delcorps, C.; Irenge, L. M.; Walravens, K.; Marche, S.; Gala, J. L. *J Clin Microbiol* **2005**, *43*, 4640-4648.
(19) Machackova-Kopecna, M.; Bartos, M.; Straka, M.; Ludvik, V.; Svastova, P.; Alvarez, J.; Lamka, J.; Trcka, I.; Treml, F.; Parmova, I.; Pavlik, I. *Vet Microbiol* **2005**, *105*, 261-268.
(20) Mackintosh, C. G.; de Lisle, G. W.; Collins, D. M.; Griffin, J. F. *N Z Vet J* **2004**, *52*, 163-174.
(21) Burton, M. S.; Olsen, J. H.; Ball, R. L.; Dumonceaux, G. A. *J Zoo Wildl Med* **2001**, *32*, 242-244.
(22) Dukes, T. W.; Glover, G. J.; Brooks, B. W.; Duncan, J. R.; Swendrowski, M. *J Wildl Dis* **1992**, *28*, 161-170.

(23) Whittington, R. J.; Marsh, I. B.; Whitlock, R. H. *Molecular and Cellular Probes* **2001**, *15*, 139-145.
(24) Beard, P. M.; Rhind, S. M.; Buxton, D.; Daniels, M. J.; Henderson, D.; Pirie, A.; Rudge, K.; Greig, A.; Hutchings, M. R.; Stevenson, K.; Sharp, J. M. *Journal of Comparative Pathology* **2001**, *124*, 290-299.
(25) Judge, J.; Kyriazakis, I.; Greig, A.; Allcroft, D. J.; Hutchings, M. R. *Appl Environ Microbiol* **2005**, *71*, 6033-6038.
(26) USDA: http://www.aphis.usda.gov/vs/ceah/ncahs/nahms/dairy/dairy02/Dairy02_Johnes_highlights.pdf, February 2005.
(27) USDA; Garry, F., Wells, S., Ott, S., Hansen, D., Eds.: http://www.aphis.usda.gov/vs/ceah/ncahs/nahms/dairy/dairy96/johnsart.htm, March 1999.
(28) Stabel, J. R. *J Dairy Sci* **1998**, *81*, 283-288.
(29) WHO *Tuberculosis Fact sheet N°104 - Global and regional incidence*, World Health Organization. accessed: May 4, 2007
(30) CDC *Interactive Core Curriculum on Tuberculosis: What the Clinician Should Know, version 1.0*, October 2004.
(31) http://www.aphis.usda.gov/vs/nahps/johnes/ *Johne's Disease*, USDA - Animal and Plant Health Inspection Services. accessed: May 4, 2007
(32) Dart, R. K. *Microbiology for the Analytical Chemist*; The Royal Society of Chemistry: Cambridge, UK, 1996.
(33) Leoni, E.; Legnani, P. P. *J Appl Microbiol* **2001**, *90*, 27-33.
(34) Forbes, B. A.; Sahm, D. F.; Weissfeld, A. S. *Bailey and Scott's Diagnostice Mircrobiology*, 12th ed.; Mosby Elsevier: St. Louis, 2007.
(35) http://johnes.vetmed.wisc.edu/ *Johne's Information Center*, University of Wisconsin - School of Veterinary Medicine. accessed: May 28, 2007
(36) Piersimoni, C.; Scarparo, C.; Callegaro, A.; Tosi, C. P.; Nista, D.; Bornigia, S.; Scagnelli, M.; Rigon, A.; Ruggiero, G.; Goglio, A. *J Clin Microbiol* **2001**, *39*, 651-657.
(37) Saiki, R. K.; Scharf, S.; Faloona, F.; Mullis, K. B.; Horn, G. T.; Erlich, H. A.; Arnheim, N. *Science* **1985**, *230*, 1350-1354.
(38) Bej, A. K.; Mahbubani, M. H.; Dicesare, J. L.; Atlas, R. M. *Appl Environ Microbiol* **1991**, *57*, 3529-3534.
(39) Newton, C. R.; Graham, A. *PCR* 2nd ed.; BIOS Scientific Publishers: Oxford, UK, 1997.
(40) Costas, M. *Advances in Electrophoresis* **1992**, *5*, 351-408.
(41) Berg, J. M.; Tymoczko, J. L.; Stryer, L. *Biochemistry*, 5th ed. ed.; W. H. Freeman and Company: New York, 2001.
(42) Cockerill, F. R.; Uhl, J. R. In *Rapid Cycle Real-Time PCR - Methods and Applications, Microbiology and Food Analysis*; Reischl, U., Wittwer, C., Cockerill, F., Eds.; Springer: New York, 2002, pp 3-27.
(43) Tenover, F. C. *Clinical Infectious Diseases* **2007**, *44*, 418-423.
(44) Deisingh, A. K.; Thompson, M. *J Appl Microbiol* **2004**, *96*, 419-429.
(45) Yaron, S.; Matthews, K. R. *J. Appl. Microbiol.* **2002**, *92*, 633-640.

(46) Kox, L. F. F.; Jansen, H. M.; Kuijper, S.; Kolk, A. H. J. *Journal of Clinical Microbiology* **1997**, *35*, 1492-1498.
(47) Touron, A.; Berthe, T.; Pawlak, B.; Petit, F. *Res Microbiol* **2005**, *156*, 541-553.
(48) Cheng, V. C.; Yam, W. C.; Hung, I. F.; Woo, P. C.; Lau, S. K.; Tang, B. S.; Yuen, K. Y. *J Clin Pathol* **2004**, *57*, 281-285.
(49) Ridderhof, J. C.; Williams, L. O.; Legois, S.; Shult, P. A.; Metchock, B.; Kubista, L. N.; Handsfield, J. H.; Fehd, R. J.; Robinson, P. H. *J Clin Microbiol* **2003**, *41*, 5258-5261.
(50) Ellingson, J. L. E.; Stabel, J. R.; Bishai, W. R.; Frothingham, R.; Miller, J. M. *Molecular and Cellular Probes* **2000**, *14*, 153-161.
(51) Schroder, K.; Hertzog Paul, J.; Ravasi, T.; Hume David, A. *J Leukoc Biol* **2004**, *75*, 163-189.
(52) http://www.cellestis.com/ *QuantiFERON® technology*, Cellestis. accessed: May 5, 2007
(53) Harris, N. B.; Barletta, R. G. *Clin Microbiol Rev* **2001**, *14*, 489-512.
(54) Stabel, J. R.; Whitlock, R. H. *Vet Immunol Immunopathol* **2001**, *79*, 69-81.
(55) Mazurek, G. H.; Villarino, M. E. *MMWR Recomm Rep* **2003**, *52*, 15-18.
(56) Huda, A.; Lind, P.; Christoffersen, A. B.; Jungersen, G. *Vet Immunol Immunopathol* **2003**, *94*, 95-103.
(57) McDonald, W. L.; Ridge, S. E.; Hope, A. F.; Condron, R. J. *Aust Vet J* **1999**, *77*, 113-119.
(58) Clarke, C. J.; Patterson, I. A.; Armstrong, K. E.; Low, J. C. *Vet Rec* **1996**, *139*, 618-621.
(59) Colgrove, G. S.; Thoen, C. O.; Blackburn, B. O.; Murphy, C. D. *Vet Microbiol* **1989**, *19*, 183-187.
(60) Sergeant, E. S.; Whittington, R. J.; More, S. J. *Prev Vet Med* **2002**, *52*, 199-211.
(61) Caron, G. N.-v.; Badley, R. A. *Flow Cytometry Applications in Cell Culture* **1996**, 257-290.
(62) Steen, H. B. *J Microbiol Methods* **2000**, *42*, 65-74.
(63) Alvarez, A. M. *Annual Review of Phytopathology* **2004**, *42*, 339-366.
(64) Edwards, C. *Flow Cytometry Applications in Cell Culture* **1996**, 291-310.
(65) Fox, A. *Journal of Clinical Microbiology* **2006**, *44*, 2677-2680.
(66) Wild, D. *The Immunoassay Handbook, Second Edition*, 2001.
(67) Yalow, R. S.; Berson, S. A. *Nature* **1959**, *184*, 1648-1649.
(68) Ekins, R. P. *Clinica Chimica Acta* **1960**, *5*, 453-459.
(69) Diamandis, E. P.; Christopoulos, T. K., Eds. *Immunoassay*; Academic Press: San Diego, 1996.
(70) Law, B.; Editor *Immunoassay: A Practical Guide*, 1996.
(71) Sergeant, E. S.; Marshall, D. J.; Eamens, G. J.; Kearns, C.; Whittington, R. J. *Prev Vet Med* **2003**, *61*, 235-248.
(72) Sockett, D. C.; Conrad, T. A.; Thomas, C. B.; Collins, M. T. *J Clin Microbiol* **1992**, *30*, 1134-1139.
(73) Gorton, L., Ed. *Biosensors and Modern Biospecific Analytical Techniques*; Elsevier: New York, 2005.

(74) Collins, M. T.; Wells, S. J.; Petrini, K. R.; Collins, J. E.; Schultz, R. D.; Whitlock, R. H. *Clin Diagn Lab Immunol* **2005**, *12*, 685-692.
(75) Garg, S. K.; Tiwari, R. P.; Tiwari, D.; Singh, R.; Malhotra, D.; Ramnani, V. K.; Prasad, G. B.; Chandra, R.; Fraziano, M.; Colizzi, V.; Bisen, P. S. *J Clin Lab Anal* **2003**, *17*, 155-163.
(76) Imaz, M. S.; Comini, M. A.; Zerbini, E.; Sequeira, M. D.; Latini, O.; Claus, J. D.; Singh, M. *J Clin Microbiol* **2004**, *42*, 884-887.
(77) Whitlock, R. H.; Wells, S. J.; Sweeney, R. W.; Van Tiem, J. *Vet Microbiol* **2000**, *77*, 387-398.
(78) Dargatz, D. A.; Byrum, B. A.; Barber, L. K.; Sweeney, R. W.; Whitlock, R. H.; Shulaw, W. P.; Jacobson, R. H.; Stabel, J. R. *J Am Vet Med Assoc* **2001**, *218*, 1163-1166.
(79) Butler, J. E. *Immunochemsitry of Solid-Phase Immunoassay*; CRC Press: Boca Raton, FL, 1991.
(80) Shankaran, D. R.; Gobi, K. V.; Miura, N. *Sensors and Actuators, B: Chemical* **2007**, *B121*, 158-177.
(81) Shalaev, V. M.; Bozhevolnyi, A. U. *Photonics Spectra* **2006**, *Februray 2006*, 66-72.
(82) Smith, E. A.; Corn, R. M. *Applied Spectroscopy* **2003**, *57*, 320A-332A.
(83) Cooper, M. A. *Analytical and Bioanalytical Chemistry* **2003**, *377*, 834-842.
(84) Bruchez, M., Jr.; Moronne, M.; Gin, P.; Weiss, S.; Alivisatos, A. P. *Science* **1998**, *281*, 2013-2016.
(85) Yang, L.; Li, Y. *Analyst* **2006**, *131*, 394-401.
(86) Chan, W. C.; Nie, S. *Science* **1998**, *281*, 2016-2018.
(87) Clapp, A. R.; Goldman, E. R.; Mattoussi, H. *Nature Protocols* **2006**, *1*, 1258-1267.
(88) Wang, J. *Analytical Electrochemistry*, 3rd ed. ed.; John Wiley and Sons, Inc: Hoboken, NJ, 2006.
(89) Jin, Y.; Wang, K.; Jin, R. *Progress in Natural Science* **2006**, *16*, 445-451.
(90) Porter, M. D.; Driskell, J. D.; Kwarta, K. M.; Lipert, R. J.; Neill, J. D.; Ridpath, J. F. *Developments in biologicals* **2006**, *126*, 31-39.
(91) Millen, R. L.; Kawaguchi, T.; Granger, M. C.; Porter, M. D.; Tondra, M. *Analytical Chemistry* **2005**, *77*, 6581-6587.
(92) Shen, Z.; Huang, M.; Xiao, C.; Zhang, Y.; Zeng, X.; Wang Peng, G. *Analytical Chemistry* **2007**, *79*, 2312-2319.
(93) Ingle Jr., J. D.; Crouch, S. R. *Spectrochemical Analysis*; Prentice Hall: Upper Saddle River, NJ, 1988.
(94) Raman, C. V. *Nature* **1928**, *121*, 619.
(95) Raman, C. V.; Krishnan, K. S. *Nature* **1928**, *121*, 501-502.
(96) Long, D. A. *The Raman Effect: A Unified Treatment of the Theory of Raman Scattering by Molecules*; John Wiley and Sons, Ltd.: West Sussex, England, 2002.
(97) Fleischmann, M.; Hendra, P. J.; McQuillan, A. J. *Chemical Physics Letters* **1974**, *26*, 163-166.
(98) Jeanmaire, D. L.; Van Duyne, R. P. *Journal of Electroanalytical Chemistry and Interfacial Electrochemistry* **1977**, *84*, 1-20.
(99) Albrecht, M. G.; Creighton, J. A. *Journal of the American Chemical Society* **1977**, *99*, 5215-5217.

(100) Kelly, K. L.; Coronado, E.; Zhao, L. L.; Schatz, G. C. *Journal of Physical Chemistry B* **2003**, *107*, 668-677.
(101) Schatz, G. C. *Accounts of Chemical Research* **1984**, *17*, 370-376.
(102) Otto, A.; Timper, J.; Billmann, J.; Kovacs, G.; Pockrand, I. *Surface Science* **1980**, *92*, L55-L57.
(103) Vo-Dinh, T. *TrAC, Trends in Analytical Chemistry* **1998**, *17*, 557-582.
(104) Moskovits, M. *Reviews of Modern Physics* **1985**, *57*, 783-826.
(105) Garrell, R. L. *Analytical Chemistry* **1989**, *61*, 401A-402A, 404A, 406A-408A, 410A-411A.
(106) Kerker, M. *Accounts of Chemical Research* **1984**, *17*, 271-277.
(107) Kneipp, K.; Kneipp, H.; Itzkan, I.; Dasari, R. R.; Feld, M. S. *Journal of Physics: Condensed Matter* **2002**, *14*, R597-R624.
(108) Schatz, G. C.; VanDuyne, R. P. *Surface Science* **1980**, *101*, 425-438.
(109) Zeman, E. J.; Schatz, G. C. *Journal of Physical Chemistry* **1987**, *91*, 634-643.
(110) Driskell, J. D. *Surface-enhanced Raman scattering (SERS) for detection in immunoassays: applications, fundamentals, and optimization*, Doctoral Dissertation, Iowa State University, Ames, 2006.
(111) Kneipp, K.; Kneipp, H.; Itzkan, I.; Dasari, R. R.; Feld, M. S. *Chemical Reviews (Washington, D. C.)* **1999**, *99*, 2957-2975.
(112) Pitt, G. D.; Batchelder, D. N.; Bennett, R.; Bormett, R. W.; Hayward, I. P.; Smith, B. J. E.; Williams, K. P. J.; Yang, Y. Y.; Baldwin, K. J.; Webster, S. *IEE Proceedings: Science, Measurement and Technology* **2005**, *152*, 241-318.
(113) Grun, J.; Manka, C. K.; Bowles, J. H.; Corson, M. R. In *PCT Int. Appl.*; The United States of America, As Represented by the Secretary of the Navy, USA, 2005, 37 pp.
(114) McCreery, R. L. *Proceedings of SPIE-The International Society for Optical Engineering* **1992**, *1637*, 208-215.
(115) Doering, W. E.; Nie, S. *Journal of Physical Chemistry B* **2002**, *106*, 311-317.
(116) Luo, H.; Weaver, M. J. *Journal of Electroanalytical Chemistry* **2001**, *501*, 141-150.
(117) Weiszenbacher, N.; Frank, J.; Wanzenbock, H. D. *Analyst* **1998**, *123*, 1057-1060.
(118) Barbillat, J.; Dhamelincourt, P.; Delhaye, M.; Da Silva, E. *Journal of Raman Spectroscopy* **1994**, *25*, 3-11.
(119) Chase, B. *Applied Spectroscopy* **1994**, *48*, 14A-19A.

CHAPTER 2: Detection of *Mycobacterium avium* subsp. *paratuberculosis* using Surface-Enhanced Raman Scattering: Part I – Sonicate Immunoassay

Betsy Jean Yakes[1], Robert J. Lipert[1], John P. Bannantine[2] and Marc D. Porter[1,*]

[1] Departments of Chemistry and Chemical and Biological Engineering, Ames Laboratory-USDOE, and Institute for Combinatorial Discovery, Iowa State University, Ames, IA 50011

[2] USDA/ARS/National Animal Disease Center, Bacterial Diseases of Livestock Research Unit, Ames, IA 50010

* Corresponding author. Current address: Center for Combinatorial Sciences, Biodesign Institute, Arizona State University, Tempe, AZ 85287-6401. Phone: (480-727-8598). Fax: (480-727-9499). E-mail: Marc.Porter@asu.edu

A paper to be submitted to *Clinical and Vaccine Immunology* in companion with Part II

ABSTRACT

A sandwich immunoassay is developed for the rapid, low-level detection of *Mycobacterium avium* subsp. *paratuberculosis* (MAP). MAP is the causative agent of Johne's disease in cattle. One of the major obstacles in controlling the spread of this disease is the inability to rapidly detect small amounts of bacteria or other diagnostic makers shed during the subclinical stage of infection. This paper details the development and performance of an assay for sonicated MAP lysate that is based on surface enhanced Raman scattering (SERS). There are two key components of the assay: (1) using an immobilized layer of monoclonal antibodies that target a surface protein on the microorganism; and (2) tagging of captured proteins by extrinsic Raman labels (*ERL*s) that are designed to selectively bind to the captured protein and produce large SERS signals. By correlating the number of MAP bacilli present prior to sonication and the amount of total protein in the resulting sonicate, the

detection limit determined for total protein can be translated to the microorganism concentration. These findings yield detection limits of 500 and 1000 MAP/ml for sonicate spiked in phosphate buffer and in whole milk, respectively. Moreover, the time required to complete the assay, which includes sample preparation, antigen extraction, *ERL* incubation, and read out, is less than 24 h. The potential for incorporation of this assay into diagnostic laboratories is also briefly discussed.

INTRODUCTION

Johne's disease is responsible for devastating losses in worldwide dairy production (52). The causative agent of this disease is *Mycobacterium avium* subsp. *paratuberculosis*, referred to hereafter as MAP. MAP has been found in domestic ruminants (e.g., cattle, sheep (38, 43), and goats (53, 54)) and wildlife (e.g., deer (27, 40, 41), antelope (8, 23), bison (64), and rabbits (6, 7, 33)). Based on a serological survey conducted by the National Animal Health Monitoring System in 1996 and 2002 (58, 61), 20-40% of the cattle herds in the United States are afflicted at some level by MAP. Moreover, the 1996 report projected that the annual economic impact on the United States dairy industry from this disease exceeds $220 million (61).

Cattle are often exposed to MAP as calves (56). The disease develops through four stages and is generally diagnosed by symptomatic assessment and, when possible, quantification of shed bacteria. The four stages of progression are: silent, subclinical, clinical, and advanced cellular infection (63). During the silent stage, animals do not shed detectable amounts of the bacteria and are asymptomatic. In the subclinical phase, cattle shed small amounts of MAP in their feces and milk (e.g., 10 CFU per 50 ml of milk (29)) but still at

levels that are difficult to rapidly and reliably detect. This subtle level of shedding, nevertheless, can contaminate the surrounding habitat and spread MAP throughout a herd before its presence is detected. In the clinical phase of infection, the pathogen is shed at high levels, which can exceed 10^{10} organisms/g of feces (11). Symptoms during the terminal, advanced cellular infection stage of the disease are exemplified by chronic diarrhea, rapid weight loss, diffuse edema, reduced milk production, and infertility.

There is a wide range of tests for MAP. Bacteriologic culture is the most accepted method and benefits from easy-to-use hardware. When coupled with symptomatic evaluation, culturing provides data central to distinguishing between clinical and subclinical stages of Johne's disease. Culturing, however, typically requires 12 to 16 weeks of incubation (32). Serological tests, including complement fixation (CF), agar gel immunodiffusion (AGID), and enzyme-linked immunosorbent assay (ELISA), reduce testing time but can lack the sensitivity needed to detect MAP at subclinical levels (12-14, 16, 50, 51, 63). Methods that test for cellar immunity, such as the response to delayed-type hypersensitivity (DHT) and detection of elevated levels of gamma interferon (INF-γ), are also rapid but are indirect and can suffer from false-positives (31). Nucleic acid levels, after PCR amplification and gel electrophoresis analysis, can be determined in under three days (32) and can detect 10 MAP in a 2-ml milk sample when using immunomagnetic concentration (35). There are, however, challenges related to specificity (15, 24) and performance in complex sample matrices (35). It is therefore clear that improvements in sensitivity, selectivity, sample workup, speed, and detection are requisite in order to more effectively protect healthy animals against infection and the subsequent development and spread of Johne's disease (10).

This work explores the potential of surface-enhanced Raman scattering (SERS) to serve as a readout method for the low-level detection of MAP. Several laboratories, including our own, have demonstrated the merits of SERS readout in immunoassays (1, 19, 20, 30, 42, 44, 45, 49, 65, 67) and DNA detection (9, 25, 28). In SERS, roughened metal surfaces amplify the Raman scattering of an adsorbed organic molecule. This enhancement is mainly due to increases in the electromagnetic field at the nanometric asperities of roughened, coinage metals (e.g., silver and gold). The same mechanism is operative at the surface of metallic nanoparticles. Coupled with potential contributions from chemical effects, enhancements of up to 10^{14} have been reported (36).

Detection by SERS has several potentially valuable attributes with respect to traditional signal transduction methods such as radioisotope decay, colorimetry, and fluorescence (26, 39, 44). First, when employing gold nanoparticles, excitation in the red spectral region is used, which minimizes possible interference from native fluorescence. Second, SERS intensities for immobilized molecules are beginning to approach those of fluorescent dyes, and have the added feature of being less susceptible to photobleaching. Finally, the widths of Raman spectral bands are typically 10-100 times narrower than those of fluorescence, which reduces the potential for spectral overlap from multiple labels. The work herein seeks to take advantage of the first two attributes for the development of a rapid and highly sensitive assay for MAP.

Our SERS-based strategy uses extrinsic Raman labels (*ERL*s) as a means to quantitatively take advantage of amplified scattering (20-22, 30, 44-48). *ERL*s (Figure 1A) incorporate the intrinsically strong Raman scattering from aromatic compounds (i.e., reporter molecules). In this assay, the organic molecule is first immobilized on the gold nanoparticles,

and then the molecule is coupled to a molecular recognition element (e.g., an antibody). The preparation of the capture substrate (Figure 1B) employs the same chemistry, with the coupling molecule forming a gold-bound thiolate and then reacting with the primary amines on antibodies. We note that the depictions in Figure 1 are idealized with respect to the architectures of the immobilized antibodies. A more random distribution of orientations is expected because of the presence of amine residues throughout the structure of the protein (18). The sandwich immunoassay (Figure 1C) can then be carried out in fewer than 24 h by: (1) extracting the antigen from solution; (2) labeling with *ERL*s; and (3) quantitating the antigen by SERS. We have previously applied this platform to the detection of immunoglobulin G (44), free prostate specific antigen (PSA) (30), viruses (20), and simulants of biological warfare agents (45). These works have shown that our SERS-based immunoassay not only offers low-levels of detection (e.g., ~30 fM for PSA in human serum) but also can record single-binding events on a capture substrate (47).

This paper and the companion manuscript explore the adaptation of a highly sensitive SERS-based immunoassay system as a diagnostic platform for MAP. We use a recently developed antibody that selectively targets proteins located at the outer surface of MAP cells (2) and screen for activity and cross reactivity after immobilization. After optimizing blocking conditions and incorporating the most effective antibody into the capture substrate and *ERL*s, K-10 MAP sonicate is assayed. By correlating the number of MAP present prior to sonication with the amount of total protein in sonicate solution, detection limits of ~500 and ~1000 MAP/ml for sonicate spiked in phosphate buffer and in whole milk, respectively, are achieved. The companion paper extends detection to whole cell MAP and investigates the possibility of signal amplification from shed protein. Taken together, this method is a

specific, sensitive, and rapid test for Johne's disease that could efficiently track MAP infection. In addition, the quantitative nature of this technique could allow for more precise definitions of the disease stages (e.g., clinical versus subclinical) in terms of bacteria levels in feces and milk.

MATERIALS AND METHODS

Bacteria and sonicate preparation. Heat-killed, whole-cell MAP (K-10 bovine isolate) were grown at 37°C in Middlebrook's 7H9 medium (Becton Dickinson, Cockeysville, MD) that was supplemented with 2 mg of mycobactin J/l (Allied Monitor Inc., Fayette, MO), 10% oleic acid albumin-dextrose complex (Difco, Detroit, MI), and 0.05% Tween 80 (Sigma Aldrich, St. Louis, MO). The bacilli, harvested from the culture media by centrifugation at 10,000*g* for 20 min, were washed twice with cold phosphate buffered saline solution (PBS; 0.15 M, pH 7.2). Following washing, the bacteria were either heat treated (80°C for 30 min) or sonicated.

Whole-cell sonicated extracts of MAP (K-10 sonicate) in PBS (pH 7.4) were produced as described previously (62). After culturing MAP to an optical density of 0.2 to 0.4 at 540 nm (OD_{540}) and centrifuging, the pellet was resuspended in PBS and was sonicated. Sonication used a probe sonicator and consisted of three, 10-min cycles at 18 W on ice, with 10-min chilling periods between sonications. Debris was removed by centrifugation (12,000*g* for 5 min), and supernatants were harvested and stored at 20°C.

The concentrations of the stock solutions of heat-killed, whole-cell bacteria were determined by: (1) flow cytometry using LIVE/DEAD® Bac*Light*™ Bacterial Viability and Counting Kit (Molecular Probes, Eugene, OR); (2) bacterial enumeration through serial

dilution plating on Herrold's egg yolk slants containing mycobactin J (2 mg/l); and/or (3) OD_{540} measurements. The average value for the stock solutions used in immunoassay development was $1.3\pm0.3\times10^7$ bacteria/ml (six samples of MAP in PBS). For the stock solutions that were sonicated, the bacteria concentration (pre-sonication) was determined to be 5×10^6 MAP/ml. After sonicating, the solution had a total protein concentration of 1 mg/ml as determined by absorbance measurements at 280 nm with a ND-1000 Spectrophotometer (NanoDrop Technologies, Inc., Rockland, DE). This value was further confirmed by using the Bio-Rad protein assay (Richmond, CA).

Heat-killed *Salmonella typhimurium* and heat-killed *Escherichia coli* O157:H7 were gifts from Nancy Cornick (Department of Veterinary Microbiology and Preventive Medicine, Iowa State University, Ames, IA).

Preparation of Sonicate Spiked Samples in PBS and Whole Milk. Antigen solutions were prepared by serial dilution of the stock, K-10 sonicate with 10 mM PBS (pH 7.4, 10 mM phosphate buffered saline powder packs, Sigma-Aldrich) or pasteurized, whole milk. Between dilutions, solutions were mixed by vortexing. Distilled water, subsequently deionized with a Millipore Milli-Q system (18 MΩ, Billerica, MA), was used for the preparation of all aqueous reagents. For assays in a milk matrix, whole milk at room temperature was employed in place of PBS during serial dilution. Specifically, the first dilutions were prepared by adding 10 µl of 1 mg/ml sonicate in PBS to either 10 µl of whole milk (5×10^5 ng/ml) or 90 µl of whole milk (10^5 ng/ml), and serial dilutions with whole milk were continued from these concentrations.

Antibodies. Monoclonal antibodies (mAbs) to MAP2121c, a MAP surface protein, have recently been produced (4). Three monoclonal antibodies (8G2, 13E1, and 12C9), the

former two specific for the MAP2121c protein, were tested for performance after purification using Melon Gel (Pierce, Rockford, IL). This step removes extraneous proteins from the tissue culture supernatants that could potentially compete with mAb immobilization. The concentrations of the mAb solutions were determined spectrophotometrically (ND-1000, standard mass extinction coefficient of 13.7 L g^{-1} cm^{-1} for 10 mg/mL IgG solution), and all mAb dilutions employed 50 mM borate buffer (pH 8.3 borate buffer packs, Pierce).

***ERL* Preparation.** The design, preparation, and optimization of the *ERL*s were detailed in our previous work (20). Briefly, 1.0 ml of 60-nm gold particles (<8% variation in diameter, 2.6 x 10^{10} particles/ml, Ted Pella, Redding, CA) were added to a centrifuge vial. The pH of the suspension was adjusted with 40 µl of 50 mM borate buffer (pH 8.3). To this colloidal suspension, 10 µl of 1.4 mM DSNB (i.e., 5,5'-dithiobis (succinimidyl-2-nitrobenzoate)) in acetonitrile (HPLC-grade, Fisher, Pittsburgh, PA) were added. DSNB was synthesized according to previously described methods (30). DSNB coats the gold nanoparticles through chemisorption as the corresponding thiolate. After 7 h, 20 µg of one of the three mAbs were added to the mixture and incubated for ~14 h. At pH 8.3, the amines on the mAb are deprotonated and form an amide linkage upon reaction with the succinimidyl esters of the DSNB-based monolayer. Finally, to block unreacted succinimidyl esters, as well as stabilize the colloidal solution, 100 µL of 10% bovine serum albumin (BSA, Sigma-Aldrich) in 2 mM borate buffer were added to the suspension and allowed to react for 7 h.

Next, the colloidal suspension was centrifuged (Eppendorf MiniSpin, Westbury, NY) at 2,000*g* for 10 min at room temperature to remove excess reagents. After decanting the clear supernatant, the loose colloidal gold pellet was resuspended in 1000 µl of 2 mM borate buffer containing 1% BSA. This centrifugation/resuspension procedure was repeated twice to

maximize excess reagent removal. The volume after the last resuspension step was 500 µL. Finally, 50 µL of 10% sodium chloride (Sigma-Aldrich) were added to the suspension which was then passed through a Costar 0.22-µm syringe filter (Fisher) in order to remove any aggregates.

Capture Surface Preparation. The fabrication of the capture substrate followed past procedures (20, 30, 44, 45). Template stripped gold (TSG) was prepared by resistively evaporating ~300 nm of gold (99.9%) at 0.1 to 0.2 nm/s onto a 4-in, p-type, test grade silicon [111] wafer (University Wafer, South Boston, MA) using an Edwards 306A evaporator. After applying cleaned 1 × 1 cm glass chips to the gold surface via two-part epoxy (Epo-tek 377, Billerica, MA) and oven curing at 150°C for 1.75 h, the glass slides were carefully separated from the wafer, exposing a smooth gold surface.

A poly(dimethyl siloxane) (PDMS, Dow Corning, Midland, MI) stamp with a centered, 3.2-mm diameter hole was soaked in a 2 mM octadecanethiol (ODT, Sigma-Aldrich) ethanolic solution. The stamp was dried under a stream of high purity nitrogen. The TSG substrates were then inked (~30 s) with the ODT coated-PDMS stamp. This procedure formed a hydrophobic barrier that surrounded a 3.2-mm assay address. These samples were subsequently exposed to a 1 mM ethanolic (Aaper, Shelbyville, KY) solution of dithiobis(succinimidyl propionate) (DSP, Sigma-Aldrich) for ~14 h which formed a DSP-derived monolayer within the address area. After rinsing with ethanol and drying under a stream of nitrogen, 20 µl of capture antibody (100 µg/ml) were dispensed onto each substrate. This step couples the antibody to the DSP-based monolayer by the same mechanism as that for DSNB. After incubation for 7 h in a humidity chamber, the substrates were rinsed three times with 2 ml of 10 mM PBS buffer. Unreacted succinimdyl endgroups

of the monolayer were "capped" with a 20 µl drop of blocking buffer ~14 h (i.e., SuperBlock and StarterBlock (Pierce); 5% BSA in PBS, 2% Carnation dry milk in PBS, or Casein blocking solution (Sigma-Aldrich)).

Immunoassay Procedure. After blocking, the capture surface was exposed for 7 h to either heat-killed, whole-cell 1.0×10^7 MAP/ml or varying concentrations of K-10 sonicate in 10 mM PBS (pH 7.4) at room temperature in a humidity chamber. After rinsing three times with 2 mM borate buffer (pH 8.3, 150 mM NaCl), a 20-µl drop of the *ERL*s was placed on the substrates and allowed to react ~14 h. The substrates were again washed with the 2 mM borate solution, gently dried with nitrogen, and the SERS spectra collected. This procedure follows that depicted in Figure 1C.

SERS Measurements with a *NanoRaman*™ I Spectrometer. Raman spectra were collected using a *NanoRaman*™ I spectrometer (Concurrent Analytical, Waimanalo, HI). This instrument consists of a HeNe laser (632.8 nm, 30 mW, 25-µm diameter spot size), fiber-optic-based probe head, an *f*/2.0 Czerny-Turner imaging spectrometer (6-8 cm^{-1} resolution), and a thermoelectrically cooled CCD (0°C, Kodak 0401E). The laser light was focused as a 25-µm spot (2-3 mW) onto the substrate surface at normal incidence via an objective with a numerical aperture of 0.68, which also collected the scattered radiation. Exposure times of 1-s were employed with an average of four or five measurements, as noted in the Results section, collected from different locations on each sample.

RESULTS

Antibody Screening. As shown in our previous work on feline calicivirus (37), candidate antibodies should be screened in order to determine those that are the most

effective at binding the antigen after immobilization on the capture substrate (34). As such, Dot Blot reactivity with heat-killed, whole cell MAP was used to narrow a pool of eight mAbs, selected from an ongoing Johne's Disease Integrated Program (JDIP) project (4, 5), to three. These three were designated 13E1, 12C9, and 8G2. Both 13E1 and 8G2 react with different epitopes on MAP2121c (4) and 12C9 binds to an unidentified MAP protein (5). After purification, each antibody was tested by performing an immunoassay with an antigen concentration of 1.0×10^7 MAP/ml and a PBS blank.

Using the sensor platform depicted in Figure 1, the SERS spectra shown in Figure 2 were obtained. The strongest feature in each spectrum (1336 cm^{-1}) is assigned to a symmetric nitro stretch ($\nu_s(NO_2)$), while the less intense band (1588 cm^{-1}) is diagnostic of an aromatic ring mode. These and all the other spectral features that are present are consistent with those expected for the DSNB-derived monolayer. Furthermore, the evolution of the intensities of the these features is indicative of the amount of *ERL*s and thus antigen bound to the surface; that is, a larger SERS signal is diagnostic of a higher level of captured antigen. The signal for $\nu_s(NO_2)$ in each assay, as obtained from measurements at four locations per sample, was 293±75 cts/s for 8G2, 223±80 cts/s for 12C9, and 1611±63 cts/s for 13E1. The blank, performed with 13E1, had a signal of 256±21 cts/s. Thus, 13E1, with the largest SERS intensity and approximately the same blank signal as for 12C9 and 8G2, was the most effective of the mAbs for our heterogeneous immunoassay.

These samples were also examined by light microscopy. The images showed that only 13E1 substrates captured an observable amount of MAP, which is roughly a 1.5×0.5 μm rod. In contrast, the substrates coated with 12C9 or 8G2 exhibited little evidence for binding (data not shown). Based on the combined weight of these two sets of results, 13E1 was

chosen for the remainder of the studies. It is important to note that while 12C9 and 8G2 mAbs had higher titers and stronger immunoblot responses (J. P. Bannantine, unpublished data), 13E1 was more effective when immobilized on the capture substrate. This exemplified the importance of screening mAbs after being tethered to substrates in a heterogeneous immunoassay (17, 37).

Cross Reactivity. Specificity is another important figure of merit for diagnostic methods. Cross reactivity studies of 13E1 with other closely related *Mycobacteria* have recently been performed via immunoblots (4). Those studies revealed 13E1 also reacted with *Mycobacterium avium* complex (MAC) members. However, and more importantly, there was a lack of detectable cross reactivity with *M. bovis,* the other *Mycobacterial* pathogen in cattle, as well as non-MAC *Mycobacteria* which could also be present in bovine feces or milk.

To further assess the specificity of 13E1, especially after immobilization on the substrate, cross reactivity studies were performed by using two commonly occurring bacteria in bovine milk and feces: *E. coli* O157:H7 (57) and *Salmonella typhimurium* (59, 60). These assays were therefore carried out with 13E1 platforms and either *E. coli* or *S. typhimurium* as a potential cross reactor. After exposing the samples to *ERL*s, the intensity for $\nu_s(NO_2)$ was obtained. As shown in Figure 3, the results yielded 231 ± 16 cts/s for the PBS blank (no bacteria), 279±23 cts/s for 1.0×10^8 cfu of *E. coli* O157:H7/ml, and 135±15 cts/s for 7.3×10^9 cells of *S. typhimurium*/ml. While more exhaustive cross reactivity studies remain to be performed, these results indicate there is no loss in selectively when 13E1 is immobilized on the capture substrate.

Blocker Optimization. As part of an optimization protocol, studies were performed to determine which blocking agent would minimize the blank signal while maximizing the response for MAP. To this end, solutions of SuperBlock, StartingBlock, 5% BSA in PBS, 2% dry milk in PBS, Casein based blocker, or PBS (no blocker) were placed on separate 13E1 substrates. These substrates were then exposed to PBS (blank) or to a solution containing 1.0×10^5 MAP/ml. The results from the SERS readout of each sample are summarized in Figure 4. The samples treated with StartingBlock had the highest signal for MAP but, according to the blank response, also had the highest level of nonspecific adsorption of *ERL*s. Moreover, the blocking solutions of 5% BSA, 2% dry milk, and Casein failed to remain confined in the 3.2-mm sample address because of their low surface tension. This "drop spreading" led to low signals for the MAP-containing samples. While PBS (no blocker) and SuperBlock have roughly the same blank and MAP signals, the precision of the measurement was three times better for SuperBlock. Based on these results, SuperBlock was used in the subsequent studies.

Spiked PBS Samples. The K-10 sonicate samples, with concentrations ranging from 1×10^2 to 5×10^5 ng/ml, were incubated with the capture platform (Figure 1B). After rinsing, the substrates were exposed to *ERL*s (Figure 1C). Importantly, these two steps, as well as those involved in sample preparation (e.g., sonication), require less than 24 h to complete. The resulting SERS spectra, read out in only 1 s, and calibration curve, prepared by subtracting the background at 1225 cm^{-1} from the intensity of $\nu_s(NO_2)$ at 1336 cm^{-1}, are shown in Figure 5. As evident, the SERS signals increased in a concentration-dependent manner with sonicated antigen. The lowest detectable signal, as defined by the blank signal plus three times its standard deviation, is denoted by the dashed line in the calibration curve.

The limit of detection (LOD), which corresponds to the intersection of these two curves, was calculated to be ~100 ng/ml. Since the original solution (5×10^6 MAP/ml) produced 1 mg/mL of protein, the LOD for the K-10 sonicate is ~500 MAP/ml.

Spiked Milk Samples. To determine the feasibility of analyzing relevant biological samples, an initial study was performed using a milk matrix. Room temperature, pasteurized, whole milk was spiked with the K-10 sonicate for concentrations up to 5×10^5 ng/ml. As before, the assay procedure was performed in fewer than 24 h, with the resulting calibration curve shown in Figure 6. Importantly, the milk matrix plot is strongly similar to that of the PBS matrix in Figure 5b. That is, the close agreement between the best fit lines (i.e., slopes and y-intercept) and precision (i.e., standard deviations for individual samples) indicate that the performance achieved in the clean, PBS matrix is not compromised when using the much more complex whole milk matrix. Furthermore, the plot in Figure 6 translates to a LOD of ~200×10^2 ng/ml (~1000 MAP/ml). These findings elucidate the robust nature of our assay system with respect to its potential application in complex matrices. These results also demonstrate that analysis in whole milk can be carried out with little sample workup.

DISCUSSION

There is a wide range of diagnostic tests for Johne's disease, each with the previously detailed strengths and limitations in performance. In order to protect healthy animals from this disease and minimize its spread, a more effective means to identify infected cattle, track disease development, and characterize clinical stages are necessary. The results herein demonstrate that our SERS-based immunoassay can potentially address these needs and be readily extended to complex matrices like milk. LODs for the K-10 sonicate, obtained in 24

h, are ~500 MAP/ml in PBS and ~1000 MAP/ml in pasteurized, whole milk. This level of performance is a direct result of our integration of the 13E1 antibody as a recognition element with SERS as a readout tool.

Several key features of this assay offer advantages over current detection techniques. First, INF-γ detection, as an indirect method, can be problematic because of false-positives. PCR, while a direct method, may yield false-negative results in complex matrices (55). Immunoassay techniques, including ELISA and our SERS-based immunoassay, show improvements over INF-γ detection and PCR by incorporation of antibody recognition. In our system, the 13E1 mAb targets a surface protein (MAP2121c) that plays a role in the MAP invasion of epithelial cells (3). The screening and cross reactivity studies carried out earlier (4) and in this work highlight the specificity of this mAb, which could allow for a low number of false-positive results in clinical samples. Of particular importance is the lack of detectable cross reactivity with *M. Bovis*, which is the other Mycobacterial pathogen in cattle.

Second, SERS, in conjunction with *ERL*s, is a highly sensitive readout tool. By taking advantage of the gold to disulfide linking chemistry, many DSNB reporter molecules are easily tethered to a single nanoparticle, amplifying the signal from a single binding event. In addition, the DSNB-derived monolayer can tether antibodies and thus form a biospecific label. By incorporating these *ERL*s in our sandwich immunoassay, the MAP concentration is quantified by the intensity of the intrinsically strong $\nu_s(NO_2)$ of the DSNB-derived monolayer, and low-levels of detection are obtained. In addition, the good precision/reproducibility in measurements seen in the sonicate immunoassay is partially due to recent advances in formation of uniform nanoparticles and preparation of optimized *ERL*s.

Another important feature of our SERS-based assay is its potential for integration into diagnostic laboratories. The instrumentation (a fiber-optic based Raman spectrometer) has no moving parts, is easy-to-use, and has a small footprint on the laboratory benchtop. In addition, breakthroughs in optical filters and detectors have decreased the costs of key hardware, with instrument pricing from several manufacturers on the order of $10,000-$15,000. Moreover, other components of the assay can be readily packaged into a kit that includes both pre-made capture substrates and *ERL*s. Based on this, an assay would be performed by capturing the antigen from milk and incubating *ERL*s in under 24 h, and research to extend our assay to fecal samples is in progress.

In summary, we believe that our assay is well positioned to address many of the challenges associated with Johne's disease detection, especially with respect to speed, specificity, and sensitivity. As such, experiments focused on the analysis of samples from animals clinically infected with MAP are underway. Ongoing work is also aimed at improvements in performance by examining approaches to reduce nonspecific adsorption and to further amplify the SERS signal from *ERL*s (e.g. better scatterers and tailored nanoparticles). Finally, the extension of this assay to the detection of whole MAP bacteria is detailed in the following companion paper (66).

ACKNOWLEDGMENTS

We acknowledge Dr. Jeremy Driskell for helpful conversations. This work was supported by the Institute for Combinatorial Discovery of Iowa State University. The Ames Laboratory is operated for the U.S. Department of Energy by Iowa State University under

contract W-7405-eng-82. We also acknowledge support from USDA-NRI-CAP program JDIP to JPB as well as support from the USDA's Agricultural Research Service.

REFERENCES

1. **Ansari, D. O., D. A. Stuart, and S. Nie.** 2005. Surface-enhanced Raman spectroscopic detection of cancer biomarkers in intact cellular specimens. Proc. SPIE **5699:**82-90.
2. **Bannantine, J. P., E. Baechler, Q. Zhang, L. Li, and V. Kapur.** 2002. Genome scale comparison of Mycobacterium avium subsp. paratuberculosis with Mycobacterium avium subsp. avium reveals potential diagnostic sequences. J. Clin. Microbiol. **40:**1303-10.
3. **Bannantine, J. P., J. F. Huntley, E. Miltner, J. R. Stabel, and L. E. Bermudez.** 2003. The Mycobacterium avium subsp. paratuberculosis 35 kDa protein plays a role in invasion of bovine epithelial cells. Microbiology **149:**2061-9.
4. **Bannantine, J. P., T. J. Radosevich, J. R. Stabel, S. Berger, J. F. Griffin, and M. L. Paustian.** 2007. Production and Characterization of Monoclonal Antibodies against a major Membrane Protein of Mycobacterium avium subsp. paratuberculosis. Clin. Vaccine Immunol. **14:**312-7.
5. **Bannantine, J. P., T. J. Radosevich, J. R. Stabel, S. Sreevatsan, V. Kapur, and M. L. Paustian.** 2007. Development and Characterization of Monoclonal Antibodies and Aptamers against Major Antigens of Mycobacterium avium subsp. paratuberculosis. Clin. Vaccine Immunol. **14:**518-526.
6. **Beard, P. M., M. J. Daniels, D. Henderson, A. Pirie, K. Rudge, D. Buxton, S. Rhind, A. Greig, M. R. Hutchings, I. McKendrick, K. Stevenson, and J. M. Sharp.** 2001. Paratuberculosis infection of nonruminant wildlife in Scotland. J. Clin. Microbiol. **39:**1517-21.
7. **Beard, P. M., S. M. Rhind, D. Buxton, M. J. Daniels, D. Henderson, A. Pirie, K. Rudge, A. Greig, M. R. Hutchings, K. Stevenson, and J. M. Sharp.** 2001. Natural paratuberculosis infection in rabbits in Scotland. J. Comp. Pathol. **124:**290-9.
8. **Burton, M. S., J. H. Olsen, R. L. Ball, and G. A. Dumonceaux.** 2001. Mycobacterium avium subsp. paratuberculosis infection in an addax (Addax nasomaculatus). J. Zoo. Wildl. Med. **32:**242-4.
9. **Cao, Y. C., R. Jin, and C. A. Mirkin.** 2002. Nanoparticles with Raman spectroscopic fingerprints for DNA and RNA detection. Science **297:**1536-40.
10. **Chacon, O., L. E. Bermudez, and R. G. Barletta.** 2004. Johne's disease, inflammatory bowel disease, and Mycobacterium paratuberculosis. Annu. Rev. Microbiol. **58:**329-63.
11. **Chiodini, R. J., H. J. Van Kruiningen, and R. S. Merkal.** 1984. Ruminant paratuberculosis (Johne's disease): the current status and future prospects. Cornell Vet. **74:**218-62.

12. **Clarke, C. J., I. A. Patterson, K. E. Armstrong, and J. C. Low.** 1996. Comparison of the absorbed ELISA and agar gel immunodiffusion test with clinicopathological findings in ovine clinical paratuberculosis. Vet. Rec. **139:**618-21.
13. **Colgrove, G. S., C. O. Thoen, B. O. Blackburn, and C. D. Murphy.** 1989. Paratuberculosis in cattle: a comparison of three serologic tests with results of fecal culture. Vet. Microbiol. **19:**183-7.
14. **Collins, M. T., S. J. Wells, K. R. Petrini, J. E. Collins, R. D. Schultz, and R. H. Whitlock.** 2005. Evaluation of five antibody detection tests for diagnosis of bovine paratuberculosis. Clin. Diagn. Lab. Immunol. **12:**685-92.
15. **Cousins, D. V., R. Whittington, I. Marsh, A. Masters, R. J. Evans, and P. Kluver.** 1999. Mycobacteria distinct from Mycobacterium avium subsp. paratuberculosis isolated from the faeces of ruminants possess IS900-like sequences detectable by IS900 polymerase chain reaction: implications for diagnosis. Mol. Cell. Probes **14:**431-442.
16. **Dargatz, D. A., B. A. Byrum, L. K. Barber, R. W. Sweeney, R. H. Whitlock, W. P. Shulaw, R. H. Jacobson, and J. R. Stabel.** 2001. Evaluation of a commercial ELISA for diagnosis of paratuberculosis in cattle. J. Am. Vet. Med. Assoc. **218:**1163-6.
17. **Diamandis, E. P., and T. K. Christopoulos (ed.).** 1996. Immunoassay. Academic Press, San Diego.
18. **Dong, Y., and C. Shannon.** 2000. Heterogeneous Immunosensing Using Antigen and Antibody Monolayers on Gold Surfaces with Electrochemical and Scanning Probe Detection. Anal. Chem. **72:**2371-2376.
19. **Dou, X., T. Takama, Y. Yamaguchi, and H. Yamamoto.** 1997. Enzyme Immunoassay Utilizing Surface-Enhanced Raman Scattering of the Enzyme Reaction Product. Anal. Chem. **69:**1492-1495.
20. **Driskell, J. D., K. M. Kwarta, R. J. Lipert, M. D. Porter, J. D. Neill, and J. F. Ridpath.** 2005. Low-level detection of viral pathogens by a surface-enhanced Raman scattering based immunoassay. Anal. Chem. **77:**6147-54.
21. **Driskell, J. D., R. J. Lipert, and M. D. Porter.** 2006. Labeled Gold Nanoparticles Immobilized at Smooth Metallic Substrates: Systematic Investigation of Surface Plasmon Resonance and Surface-Enhanced Raman Scattering. J. Phys. Chem. B **110:**17444-17451.
22. **Driskell, J. D., J. M. Uhlenkamp, R. J. Lipert, and M. D. Porter.** 2007. Surface-Enhanced Raman Scattering Immunoassays Using a Rotated Capture Substrate. Anal. Chem. **79:**4141-8.
23. **Dukes, T. W., G. J. Glover, B. W. Brooks, J. R. Duncan, and M. Swendrowski.** 1992. Paratuberculosis in saiga antelope (Saiga tatarica) and experimental transmission to domestic sheep. J. Wildl. Dis. **28:**161-70.
24. **Ellingson, J. L. E., J. R. Stabel, W. R. Bishai, R. Frothingham, and J. M. Miller.** 2000. Evaluation of the accuracy and reproducibility of a practical PCR panel assay for rapid detection and differentiation of Mycobacterium avium subspecies. Mol. Cell. Probes **14:**153-161.

25. **Faulds, K., W. E. Smith, and D. Graham.** 2005. DNA detection by surface enhanced resonance Raman scattering (SERRS). Analyst **130:**1125-31.
26. **Garrell, R. L.** 1989. Surface-enhanced Raman spectroscopy. Anal. Chem. **61:**401A-402A, 404A, 406A-408A, 410A-411A.
27. **Godfroid, J., C. Delcorps, L. M. Irenge, K. Walravens, S. Marche, and J. L. Gala.** 2005. Definitive differentiation between single and mixed mycobacterial infections in red deer (Cervus elaphus) by a combination of duplex amplification of p34 and f57 sequences and Hpy188I enzymatic restriction of duplex amplicons. J. Clin. Microbiol. **43:**4640-8.
28. **Graham, D., B. J. Mallinder, D. Whitcombe, N. D. Watson, and W. E. Smith.** 2002. Simple multiplex genotyping by surface-enhanced resonance Raman scattering. Anal. Chem. **74:**1069-74.
29. **Grant, I. R., H. J. Ball, and M. T. Rowe.** 2002. Incidence of mycobacterium paratuberculosis in bulk raw and commercially pasteurized cows' milk from approved dairy processing establishments in the United Kingdom. Appl. Environ. Microbiol. **68:**2428-2435.
30. **Grubisha, D. S., R. J. Lipert, H. Y. Park, J. Driskell, and M. D. Porter.** 2003. Femtomolar detection of prostate-specific antigen: an immunoassay based on surface-enhanced Raman scattering and immunogold labels. Anal. Chem. **75:**5936-43.
31. **Harris, N. B., and R. G. Barletta.** 2001. Mycobacterium avium subsp. paratuberculosis in Veterinary Medicine. Clin. Microbiol. Rev. **14:**489-512.
32. **http://johnes.vetmed.wisc.edu/** copyright 2001, Johne's Information Center. University of Wisconsin - School of Veterinary Medicine. accessed May 28, 2007.
33. **Judge, J., I. Kyriazakis, A. Greig, D. J. Allcroft, and M. R. Hutchings.** 2005. Clustering of Mycobacterium avium subsp. paratuberculosis in rabbits and the environment: how hot is a hot spot? Appl. Environ. Microbiol. **71:**6033-8.
34. **Kenseth, J. R., K. M. Kwarta, J. D. Driskell, M. D. Porter, J. D. Neill, and J. F. Ridpath.** in preparation. Strategies in the Use of Atomic Force Microscopy as a Multiplexed Readout Tool of Chip-Scale Protein Motifs. *In* S. Mallapragada and B. Narasimhan (ed.), Combinatorial Materials Science.
35. **Khare, S., T. A. Ficht, R. L. Santos, J. Romano, A. R. Ficht, S. Zhang, I. R. Grant, M. Libal, D. Hunter, and L. G. Adams.** 2004. Rapid and sensitive detection of Mycobacterium avium subsp. paratuberculosis in bovine milk and feces by a combination of immunomagnetic bead separation-conventional PCR and real-time PCR. J. Clin. Microbiol. **42:**1075-81.
36. **Kneipp, K., H. Kneipp, I. Itzkan, R. R. Dasari, and M. S. Feld.** 2002. Surface-enhanced Raman scattering and biophysics. J. Phys.: Condens. Matter **14:**R597-R624.
37. **Kwarta, K. M., J. D. Driskell, M. D. Porter, J. D. Neill, and J. F. Ridpath.** 2007. Heterogeneous Immunoassays Utilizing Atomic Force Microscopy as a Readout Method: Evaluation of Monoclonal Antibodies for Feline Calicivirus and Porcine Parvovirus. in preparation.

38. **Lambeth, C., L. A. Reddacliff, P. Windsor, K. A. Abbott, H. McGregor, and R. J. Whittington.** 2004. Intrauterine and transmammary transmission of Mycobacterium avium subsp paratuberculosis in sheep. Aust. Vet. J. **82:**504-8.
39. **Long, D.** 2002. The Raman Effect. Wiley, New York.
40. **Machackova-Kopecna, M., M. Bartos, M. Straka, V. Ludvik, P. Svastova, J. Alvarez, J. Lamka, I. Trcka, F. Treml, I. Parmova, and I. Pavlik.** 2005. Paratuberculosis and avian tuberculosis infections in one red deer farm studied by IS900 and IS901 RFLP analysis. Vet. Microbiol. **105:**261-8.
41. **Mackintosh, C. G., G. W. de Lisle, D. M. Collins, and J. F. Griffin.** 2004. Mycobacterial diseases of deer. N. Z. Vet. J. **52:**163-74.
42. **Mulvaney, S. P., M. D. Musick, C. D. Keating, and M. J. Natan.** 2003. Glass-Coated, Analyte-Tagged Nanoparticles: A New Tagging System Based on Detection with Surface-Enhanced Raman Scattering. Langmuir **19:**4784-4790.
43. **Muskens, J., D. Bakker, J. de Boer, and L. van Keulen.** 2001. Paratuberculosis in sheep: its possible role in the epidemiology of paratuberculosis in cattle. Vet. Microbiol. **78:**101-9.
44. **Ni, J., R. J. Lipert, G. B. Dawson, and M. D. Porter.** 1999. Immunoassay readout method using extrinsic Raman labels adsorbed on immunogold colloids. Anal. Chem. **71:**4903-8.
45. **Park, H.-Y.** 2005. Chip-scale Bioassays Based on Surface-enhanced Raman Scattering: Fundamentals and Applications. Ph.D. thesis. Iowa State University, Ames, IA.
46. **Park, H.-Y., J. D. Driskell, K. M. Kwarta, R. J. Lipert, M. D. Porter, C. Schoen, J. D. Neill, and J. F. Ridpath.** 2006. Ultrasensitive immunoassays based on surface-enhanced Raman scattering by immunogold labels. Top. Appl. Phys. **103:**427-446.
47. **Park, H.-Y., R. J. Lipert, and M. D. Porter.** 2004. Single Particle Raman Measurements of Gold Nanoparticles Used in Surface-Enhanced Raman Scattering (SERS)-Based Sandwich Immunoassays. Proc. SPIE **5593:**464.
48. **Porter, M. D., J. D. Driskell, K. M. Kwarta, R. J. Lipert, J. D. Neill, and J. F. Ridpath.** 2006. Detection of viruses: atomic force microscopy and surface enhanced Raman spectroscopy. Dev. Biol. **126:**31-9.
49. **Rohr, T. E., T. Cotton, N. Fan, and P. J. Tarcha.** 1989. Immunoassay employing surface-enhanced Raman spectroscopy. Anal. Biochem. **182:**388-98.
50. **Sergeant, E. S., R. J. Whittington, and S. J. More.** 2002. Sensitivity and specificity of pooled faecal culture and serology as flock-screening tests for detection of ovine paratuberculosis in Australia. Prev. Vet. Med. **52:**199-211.
51. **Sockett, D. C., T. A. Conrad, C. B. Thomas, and M. T. Collins.** 1992. Evaluation of four serological tests for bovine paratuberculosis. J. Clin. Microbiol. **30:**1134-9.
52. **Stabel, J. R.** 1998. Johne's disease: a hidden threat. J. Dairy Sci. **81:**283-8.

53. **Storset, A. K., I. Berg, and B. Djonne.** 2005. Evaluation of the gamma interferon test for diagnosis of paratuberculosis in goats. Vet Immunol. Immunopathol. **107:**87-94.
54. **Storset, A. K., H. J. Hasvold, M. Valheim, H. Brun-Hansen, G. Berntsen, S. K. Whist, B. Djonne, C. M. Press, G. Holstad, and H. J. Larsen.** 2001. Subclinical paratuberculosis in goats following experimental infection. An immunological and microbiological study. Vet Immunol. Immunopathol. **80:**271-87.
55. **Stratmann, J., B. Strommenger, K. Stevenson, and G.-F. Gerlach.** 2002. Development of a peptide-mediated capture PCR for detection of Mycobacterium avium subsp. paratuberculosis in milk. J. Clin. Microbiol. **40:**4244-4250.
56. **Sweeney, R. W.** 1996. Transmission of paratuberculosis. Vet. Clin. N. Am. Food Anim. Pract. **12:**305-12.
57. **USDA.** December 2003. Animal and Plant Health Inspection Service Info Sheet: Escherichia coli O157 on U.S. Dairy Operations, p. 1-3, http://www.aphis.usda.gov/vs/ceah/ncahs/nahms/dairy/dairy02/Dairy02Ecoli.pdf.
58. **USDA.** February 2005. Animal and Plant Health Inspection Service Info Sheet: Highlightes of NAHMS Johne's Disease on U.S. Dairy Operations, 2002, p. 1-4, http://www.aphis.usda.gov/vs/ceah/ncahs/nahms/dairy/dairy02/Dairy02_Johnes_highlights.pdf.
59. **USDA.** December 2003. Animal and Plant Health Inspection Service Info Sheet: Salmonella and Campylobacter on U.S. Dairy Operations, p. 1-3, http://www.aphis.usda.gov/vs/ceah/ncahs/nahms/dairy/dairy02/Dairy02SalCampy.pdf.
60. **USDA.** October 2005. Animal and Plant Health Inspection Service Info Sheet: Salmonella on U.S. Dairy Operations: Prevalence and Antimicrobial Drug Susceptibility, p. 1-4, http://www.aphis.usda.gov/vs/ceah/ncahs/nahms/dairy/dairy02/Dairy02_Salmonella.pdf.
61. **USDA, F. Garry, S. Wells, S. Ott, and D. Hansen.** March 1999. Animal and Plant Health Inspection Service Info Sheet: Who can afford a $200 loss per cow? OR Johne's disease - What do I need to know?, p. 1-7, http://www.aphis.usda.gov/vs/ceah/ncahs/nahms/dairy/dairy96/johnsart.htm.
62. **Waters, W. R., J. M. Miller, M. V. Palmer, J. R. Stabel, D. E. Jones, K. A. Koistinen, E. M. Steadham, M. J. Hamilton, W. C. Davis, and J. P. Bannantine.** 2003. Early induction of humoral and cellular immune responses during experimental Mycobacterium avium subsp. paratuberculosis infection of calves. Infect. Immun. **71:**5130-5138.
63. **Whitlock, R. H., S. J. Wells, R. W. Sweeney, and J. Van Tiem.** 2000. ELISA and fecal culture for paratuberculosis (Johne's disease): sensitivity and specificity of each method. Vet. Microbiol. **77:**387-98.

64. **Whittington, R. J., I. B. Marsh, and R. H. Whitlock.** 2001. Typing of IS 1311 polymorphisms confirms that bison (Bison bison) with paratuberculosis in Montana are infected with a strain of Mycobacterium avium subsp. paratuberculosis distinct from that occurring in cattle and other domesticated livestock. Mol. Cell. Probes **15:**139-45.

65. **Xu, S., X. Ji, W. Xu, X. Li, L. Wang, Y. Bai, B. Zhao, and Y. Ozaki.** 2004. Immunoassay using probe-labelling immunogold nanoparticles with silver staining enhancement via surface-enhanced Raman scattering. Analyst **129:**63-8.

66. **Yakes, B. J., R. J. Lipert, J. P. Bannantine, and M. D. Porter.** in preparation. Detection of Mycobacterium avium subsp. paratuberculosis using Surface-Enhanced Raman Scattering: Part II - Whole Cell Immunoassay and Protein Shedding. Clin. Vaccine Immunol.

67. **Zhang, X., M. A. Young, O. Lyandres, and R. P. Van Duyne.** 2005. Rapid detection of an anthrax biomarker by surface-enhanced Raman spectroscopy. J. Am. Chem. Soc. **127:**4484-9.

FIGURES

FIG. 1. Schematic of the preparation and procedure for the SERS readout, sandwich immunoassay.

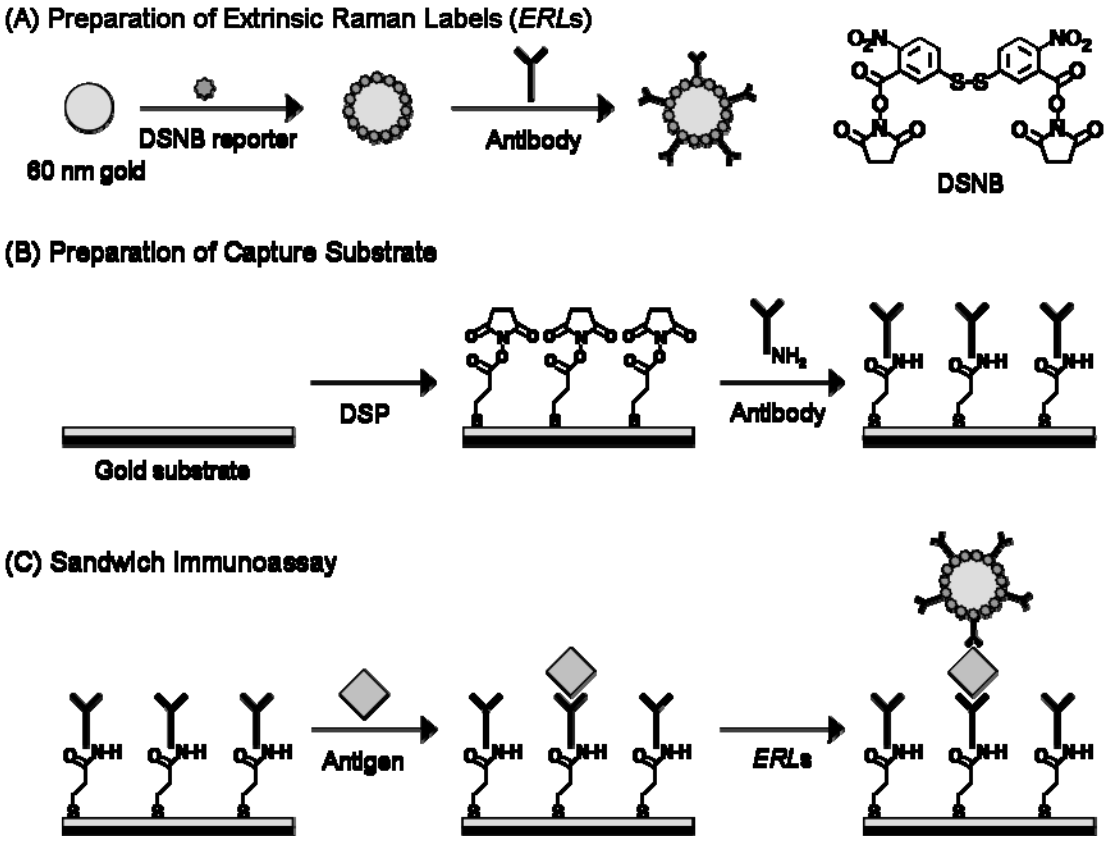

FIG. 2. Representative SERS spectra in screening studies using heterogeneous immunoassay (vertically offset for clarity) and 13E1 (PBS blank) and 8G2, 12C9 and 13E1 mAbs reacted with 1.0×10^{7} heat-killed MAP/ml. Data show 13E1 had the highest $\nu_s(NO_2)$ intensity. The blank spectrum was comparable to 12C9 and 8G2 spectra.

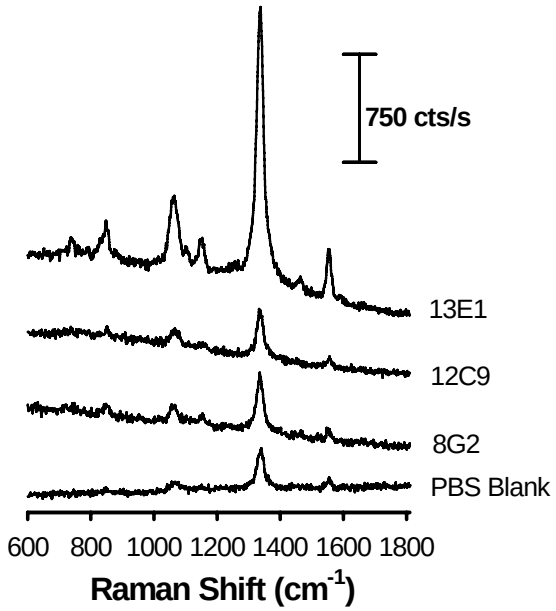

FIG. 3. 13E1 cross reactivity with commonly occurring bacteria in bovine feces. Each substrate exposed to 10^5 MAP/ml, PBS blank, *E. coli* O157:H7 (10^8 cells/ml), or *Salmonella* (10^7 cells/ml). 13E1 did not cross react with *E. coli* or *Salmonella* as signals were comparable to the PBS blank.

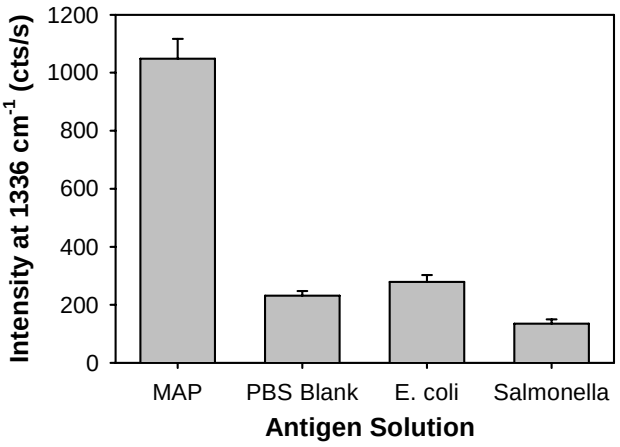

FIG. 4. SERS intensity for *ERL*s binding to MAP after various blocking solutions: (1) SuperBlock, (2) StartingBlock, (3) 5% BSA in PBS, (4) 2% dry milk in PBS, (5) Casein based blocker, (6) PBS/no blocker with either a PBS blank or 1.0×10^5 MAP/ml for the antigen step. SuperBlock yielded the largest SERS intensity and lowest blank signal.

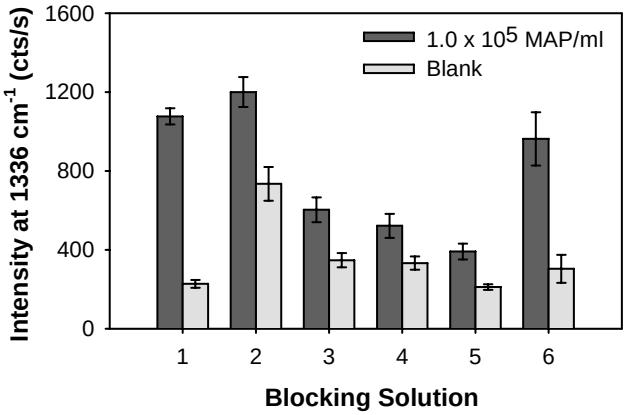

FIG. 5. Spectra and calibration curve for sonicate spiked PBS samples. (A) Spectra (vertically offset for clarity) and (B) corresponding calibration curve from SERS measurements. Dashed line corresponds to the blank plus three times its standard deviation. Best fit line is y=631x-1048, R^2=0.98.

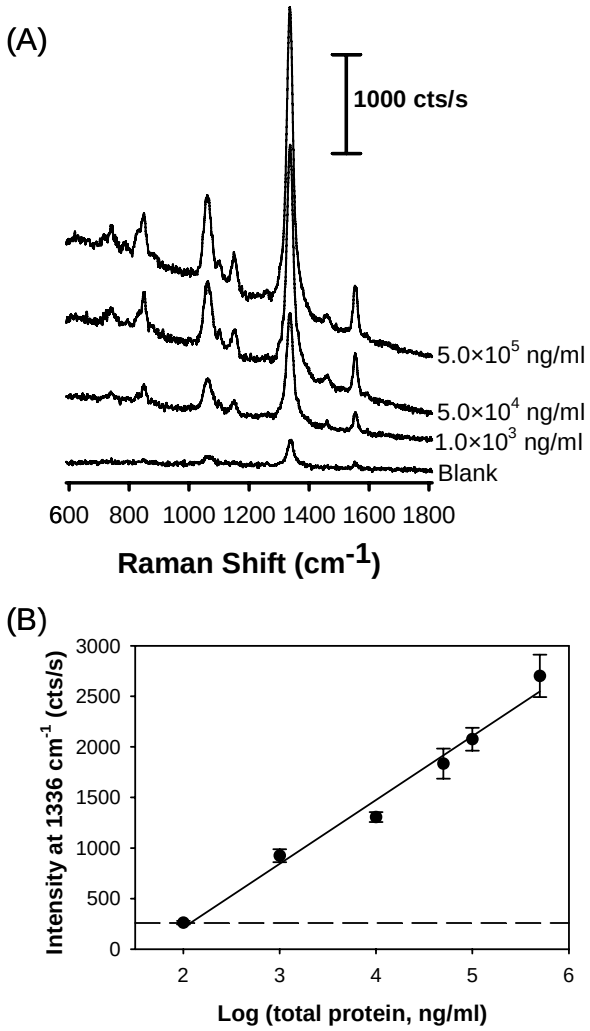

FIG. 6. Calibration curve for K10 sonicate performed in a milk matrix. Dashed line corresponds to the blank plus three times its standard deviation. Best fit line is y=592x-993, R^2=0.99.

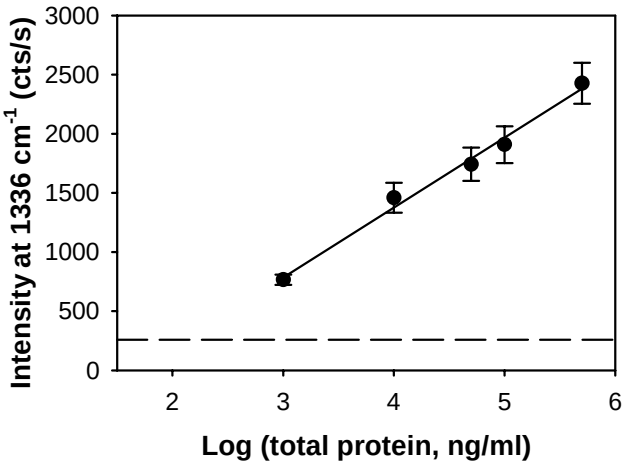

CHAPTER 3: Detection of *Mycobacterium avium* subsp. *paratuberculosis* using Surface-Enhanced Raman Scattering: Part II – Whole Cell Immunoassay and Protein Shedding

Betsy Jean Yakes[1], Robert J. Lipert[1], John P. Bannantine[2] and Marc D. Porter[1,*]

[1] Departments of Chemistry and Chemical and Biological Engineering, Ames Laboratory-USDOE, and Institute for Combinatorial Discovery, Iowa State University, Ames, IA 50011

[2] USDA/ARS/National Animal Disease Center, Bacterial Diseases of Livestock Research Unit, Ames, IA 50010

* Corresponding author. Current address: Center for Combinatorial Sciences, Biodesign Institute, Arizona State University, Tempe, AZ 85287-6401. Phone: (480-727-8598). Fax: (480-727-9499). E-mail: Marc.Porter@asu.edu

A paper to be submitted to *Clinical and Vaccine Immunology* in companion with Part I

ABSTRACT

The etiological agent of Johne's disease is *Mycobacterium avium* subspecies *paratuberculosis* (MAP). Controlling the spread of this disease, however, is hindered by the lack of sensitive, selective, and rapid detection methods for the bacteria in milk and feces. By using a recently optimized sandwich immunoassay (B. J. Yakes, R. J. Lipert, J. P. Bannantine, M. D. Porter, Clin. Vaccine Immunol., submitted) that incorporates newly prepared antibodies for MAP and surface-enhanced Raman scattering (SERS) for sensitive readout, a detection limit of ~630 and ~740 MAP/ml is achieved in phosphate buffered saline and whole milk samples, respectively, that were spiked with heat-treated MAP. Interestingly, these detection limits are much lower than expected based on a simple theoretical model for the assay. Efforts to reconcile this discrepancy produce evidence for the shedding of a major membrane protein from the heat treated bacilli. We show that the presence of shed protein

can be exploited as a mechanism for the design of a highly sensitive assay for MAP, which can potentially be applied to a wide range of other cell and virus assays.

INTRODUCTION

Mycobacterium avium subsp. *paratuberculosis* (MAP) is responsible for extensive losses in dairy production on a global scale (45). MAP is also found in other domestic ruminants (e.g., sheep (31, 35), and goats (47, 48)) and wildlife (e.g., deer (20, 32, 33), antelope (6, 16), bison (54), and rabbits (4, 5, 27)). Animals that are afflicted with MAP progress first from silent infection to a subclinical phase but do not yet show observable symptoms. Subtle levels of shedding during this time can, nonetheless, lead to the undetectable contamination of a herd. Unfortunately, once the physical symptoms associated with the clinical and advanced cellular disease phases (e.g., weight loss and chronic diarrhea) become evident, the damage is irreversible.

To control the spread of this disease, a detection method must be sensitive, rapid, field deployable, and cost effective. The assay must also be selective for MAP over other bacteria often found in milk and fecal samples from cattle. Currently available methods fall short of these combined goals. Specifically, bacteriologic culturing is lengthy (12-16 weeks) (25), serological tests lack sufficient sensitivity for detection at subclinical levels (8, 9, 11, 43, 53), and gamma interferon (23) and nucleic acid probe (10, 17) determinations can be limited by low specificity. PCR-based methods may also suffer from false-negatives in complex matrices (e.g., milk) (50). In the preceding paper (56), a method for detecting MAP sonicate in less than 24 h was designed, optimized, and yielded a limit of detection of ~500

bacilli/ml in a buffer matrix and ~1000 bacilli/ml in a milk matrix. The work herein examines the extension of this method to the analysis of samples containing whole MAP cells.

Surface-enhanced Raman scattering (SERS) has recently been shown to function as a sensitive detection method in bioanalytical sciences, especially in the area of chip scale assays [e.g., immunoassays (1, 13, 14, 22, 34, 36, 37, 41, 55, 59) and DNA (7, 18, 21)]. The basis of SERS lies in the use of a roughened metal surface to amplify normal Raman scattering, which is an inelastic scattering of light from vibrational transitions in a molecule that undergo a change in polarizability. The observed enhancement in Raman scattering (up to 10^{14} times (30)) is because of two effects: chemical and electromagnetic. The chemical component is based on the formation of a charge-transfer state between the metal surface and the adsorbed, Raman scattering molecule (51) and is viewed as contributing approximately two orders of magnitude to the overall enhancement.

The remainder of the enhancement is attributed to electromagnetic effects. When light is incident on a metal surface, conduction electrons in the metal can collectively oscillate. This process, known as surface plasmon resonance, has a wavelength dependence that is connected to the nanometeric roughness of metallic surfaces, and the size and shape of nanoparticles (28). There is also a significant body of theoretical work (19, 29, 30, 42, 58) that has proven invaluable to the fundamental understanding both mechanisms.

The method introduced in the previous paper (56), and further developed here, capitalizes on these theoretical considerations. By using extrinsic Raman labels (*ERL*s), Raman scattering molecules are chemisorbed to SERS active substrates (i.e., gold nanoparticle) and thus takes advantage of both chemical and electromagnetic effects. When incorporated into a novel SERS-based sandwich immunoassay (Figure 1), high sensitivity

can be achieved (e.g., pico- to femtomolar (22) and single binding event (38) detection). In this assay format, a biologically active molecule is selectively sandwiched between a metal surface and an extrinsic Raman label (*ERL*) by a capture antibody and a labeling antibody. The work herein evaluates this assay platform for the detection of whole MAP bacteria and presents a basis for the observed performance. The signal amplification achieved via shedding of a surface protein from MAP is also introduced with results indicating potential applicability to other pathogens.

MATERIALS AND METHODS

Bacteria Preparation. MAP, K-10 strain bacteria were cultured at the National Animal Disease Center (NADC, Ames, IA) in Middlebrook's 7H9 medium (Becton Dickinson, Cockeysville, MD) that was supplemented with mycobactin J (Allied Monitor Inc., Fayette, MO), oleic acid albumin-dextrose complex (Difco, Detroit, MI), and Tween 80 (Sigma-Aldrich, St. Louis, MO) (56). The bacilli were removed by centrifugation, washed with cold phosphate buffered saline solution (PBS; 0.15 M, pH 7.2), and heat treated at 80°C for 30 min. Whole cell bacterial concentrations were determined by flow cytometry using LIVE/DEAD® Bac*Light*™ Bacterial Viability and Counting Kit (Molecular Probes, Eugene, OR). These measurements yielded an average value of $1.3\pm0.3\times10^7$ bacteria/ml. These values were further verified by culturing live MAP and serial dilution plating on Herrold's egg yolk slants containing mycobactin J (2 mg/liter).

Preparation of PBS and Whole Milk Samples. Antigen solutions were prepared at room temperature by serial dilution of the MAP stock solution with either PBS (pH 7.4, 10 mM powder packs, Sigma-Aldrich) or pasteurized, whole milk. Between each dilution,

solutions were briefly vortexed to ensure homogeneity. Distilled water, subsequently deionized with a Millipore Milli-Q system (18 MΩ, Billerica, MA), was used for the preparation of all aqueous reagents. For the milk matrix, the initial dilution was made by adding 10 µl of 10^7 MAP/ml in PBS to 90 µl of whole milk; all further serial dilutions were performed from this 10^6 MAP/ml stock.

Antibodies. The monoclonal antibody (mAb), labeled 13E1, is specific to the major membrane protein MAP2121c (2). The MAP2121c protein was recombinantly produced in *E. coli* and subsequently used to immunize mice for production of mAbs (3). 13E1 was then purified from tissue culture supernatants at the Iowa State University Hybridoma Facility using Melon Gel (Pierce, Rockford, IL). The 13E1 concentration was determined by spectrophotometric measurements at 280 nm (ND-1000, ε=13.7 L g^{-1} cm^{-1}, NanoDrop, Wilmington, DE). All dilutions of 13E1 employed 50 mM borate buffer (pH 8.3 borate buffer packs, Pierce).

***ERL* Preparation.** Previous studies presented a detailed procedure for the formation of *ERL*s (14, 56). Briefly, 1.0 ml of 60-nm gold particles (<8% variation in diameter, 2.6 x 10^{10} particles/ml, Ted Pella, Redding, CA) was mixed with 40 µl of 50 mM borate buffer (pH 8.3). This step was followed by the addition of 10 µl of 1 mM 5,5'-dithiobis (succinimidyl-2-nitrobenzoate), DSNB, in acetonitrile (HPLC-grade, Fisher, Pittsburgh, PA). DSNB coats the nanoparticles as an adlayer of gold-bound thiolate and serves as the Raman scatter and linker molecule for antibody attachment. After 7 h of incubation, 20 µg of 13E1 were added and reacted for ~12 h, a step which tethers the mAb to the DSNB-derived coating via an amide linkage.(15, 26, 52) Finally, 100 µl of 10% bovine serum albumin (BSA, Sigma-Aldrich) in 2

mM borate buffer were pipetted into the suspension and reacted for 7 h to block unreacted succinimidyl esters.

For removal of excess reagents, the colloidal suspension was centrifuged (Eppendorf MiniSpin, Westbury, NY) at 2,000*g* for 10 min. The supernatant solution was removed, and the loose *ERL* pellet was resuspended in 1000 µl of 2 mM borate buffer containing 1% BSA. This process was repeated twice to maximize removal of unreacted materials, with a final resuspension volume of 500 µl. The next step added 50 µl of 10% w/v sodium chloride (Sigma-Aldrich) to the suspension in order to mimic biological conditions. Finally, to remove any large clusters of nanoparticles, the solution was passed through a 0.22-µm syringe filter (Costar, Fisher).

Capture Surface Formation. The capture substrates were constructed per earlier protocols (14, 22, 36, 37, 56). Gold substrates were prepared by resistive evaporation of ~300 nm of 99.9% pure gold at 0.1 to 0.2 nm/s onto a 4-in. p-type, test grade silicon [111] wafer (University Wafer, South Boston, MA) using an Edwards 306A evaporator. Cleaned 1×1 cm glass chips were then gently affixed to the gold surface via two-part epoxy (Epo-tek 377, Billerica, MA) and cured at 150°C for 1.75 h. Separation of glass chips from the wafer exposed the underlying gold surface. The gold chips were then modified by forming a hydrophobic barrier that surrounds the assay address. To this end, an octadecanethiol (Sigma-Aldrich) coated, poly(dimethyl siloxane) (Dow Corning, Midland, MI) stamp, with a 3.2-mm diameter centered hole, was used to ink the gold surface. The substrates were then exposed to a 1 mM, ethanolic (Aaper, Shelbyville, KY) solution of dithiobis(succinimidyl propionate) (DSP, Sigma-Aldrich) for 14 h. After rinsing the substrates with ethanol and drying under a stream of high purity nitrogen, 20 µl of 13E1 (100 µg/ml) were pipetted onto the substrate

and reacted for 7 h. This step linked the mAb to the substrate by the same mechanism used in the *ERL* preparation. The slides were then rinsed three times with 2 ml of 10 mM PBS buffer. Finally, unreacted succinimidyl endgroups were capped with SuperBlock (20 µl drop, Pierce).

Immunoassay Protocol. The capture substrates were exposed to varying concentrations of heat-killed, whole cell MAP (referred to hereafter simply as MAP) in 10 mM PBS buffer (pH 7.4) or pasteurized, whole milk. After incubating at room temperature in a humidity chamber for 7 h, the substrates were washed three times with 2 mM borate buffer (pH 8.3) with 150 mM NaCl. Next, the captured antigen was labeled with *ERL*s (20 µl drop) through a 14-h incubation step. Finally, the surfaces were rinsed with the borate buffer and gently dried with nitrogen.

SERS Measurements: *NanoRaman*™ I. SERS spectra for the immunoassay were collected using a *NanoRaman*™ I spectrometer (Concurrent Analytical, Waimanalo, HI) with a HeNe laser (632.8 nm, 30 mW output), fiber-optic-based probe head, an *f*/2.0 Czerny-Turner imaging spectrometer (6-8 cm^{-1} resolution), and a 0°C thermoelectrically cooled CCD (Kodak 0401E). Normal incidence laser light was focused onto the substrate surface via a 0.68 numerical aperture objective (25-µm diameter spot, 2-3 mW at surface), and exposure times of either 1- or 5-s were employed. The same objective and fiber optic probe collected the scattered radiation. All the data points in the resulting calibration curves are the average of five measurements at different locations on individual capture substrates.

SERS Measurements: Raman Microscope. The samples were also examined by using an in-house Raman spectroscopy microscope. This system was composed of an optical microscope (Olympus BH-2, Centervalley, PA) and spectrograph (SpectraPro, 300i, Acton

Research, Acton, MA) that was connected to a thinned, back-illuminated, liquid nitrogen-cooled CCD (LN/CCD-1100PB, Princeton Instruments, Trenton, NJ). For spectral measurements, a 60-mW HeNe laser (632.8 nm) was attenuated through a variable, neutral density filter (Thorlabs, Newton, NJ). The substrate was mounted on the microscope sample stage, and laser light was focused through a 100× objective to form a ~1.5-μm diameter spot size at an incident power of ~1 mW. The scattered light was collected through the same objective and directed to the spectrograph. All the microscopy-based spectra were collected with a 2-s integration time via WinSpec/32 (Princeton Instruments), and microscope images were obtained with ATI Multimedia video software (ATI Technologies, Markham, Ontario).

Scanning Electron Microscopy (SEM) Imaging. SEM images were obtained using a JEOL 59101v instrument (Tokyo, Japan). Each sample was sputter coated with a thin layer of gold prior to loading in the SEM chamber. A working distance of 10 mm and an accelerating voltage of 15 kV were used. All the images herein are from secondary electrons.

RESULTS

Spiked PBS Samples. As noted earlier, MAP solutions in PBS were incubated with the capture substrate, exposed to the *ERL*s, and read out with an integration time of 5 s (Figure 1: B1, C1). The overall process was completed in fewer than 24 h. The resulting SERS spectra and calibration curve are presented in Figure 2. All the spectral features evident in Figure 2a are consistent with vibrational modes for the DSNB-derived monolayer that coats the *ERL*s. The strongest band in the spectra is at 1336 cm^{-1} and is attributed to a symmetric nitro stretch, $\nu_s(NO_2)$, whereas the weaker bands at 1062 and 1554 cm^{-1} are

assigned to aromatic ring modes. In accord with Figure 1, the SERS intensities should track with the amount of bacteria in the antigen solution, and this trend is observed in Figure 2a.

To create the calibration curve in Figure 2b, the SERS intensity in each spectrum was calculated by subtracting the background at 1225 cm^{-1} from the signal maximum at 1336 cm^{-1} and plotted as a function of MAP concentration. The plot shows the expected increase in SERS intensity with an increase in MAP concentration, and a linear dynamic range, discussed in more detail later, spans at least five orders of magnitude. The lowest detectable signal, defined as the blank signal plus three times its standard deviation, is marked by the dashed line on the calibration plot. The intersection of this line with the best-fit to the data defines the limit of detection (LOD), which in this assay is ~630 MAP/ml.

Spiked Whole Milk. To assess performance in more complex matrices, milk was spiked with MAP at concentrations ranging from 0 to 5.0×10^6 MAP/ml. These assays followed the same procedure used for PBS but employed a readout time of 1 s. The resulting calibration curve is shown in Figure 3. Interestingly, the LOD in the whole milk matrix is ~740 MAP/ml, which is only slightly larger than that found when using PBS. Moreover, the results for PBS (Figure 2) and whole milk (Figure 3), as judged by the best fit lines, y-intercept, and precision are strikingly similar after taking into account the difference in integration times (5 s for spiked PBS and 1 s for spiked milk). These similarities argue that the presence of a complex matrix (whole milk) does not compromise the performance of our MAP assay.

MMP Shedding. While the performance of this assay is beginning to meet the multifaceted needs for MAP detection, a more in-depth examination of the data (e.g., LOD) raises questions as to the origins of the results. As discussed in detail shortly, the theoretical

LOD for our SERS-based assay is ~8×10^5 cells/ml. However, the experimentally determined LOD is more than three orders of magnitude lower than this prediction. This discrepancy led to investigations to evaluate the signal amplification per cell, with studies emphasizing the possibility of protein shedding.

Two experiments were performed to determine if free MAP2121c protein was present in the bacterial solution, which would potentially contribute to response via the pathway depicted in Figure 1:B2 and C2. The first experiment carried out assays using MAP-containing solutions before and after removal of MAP bacilli. The second study used capture substrates that had been exposed to solutions containing MAP and subsequently interrogated with a Raman microscope. This microscope has a focused laser spot that is comparable in size to that of a MAP bacillus, and can therefore be used for characterizations of the SERS response in areas with and without bacteria present.

To these ends, one set of substrates was exposed to MAP-containing solutions (20 μl). The remaining solutions were then centrifuged at 7,000 rpm (~3,300*g*) for 10 min to pellet out the bacteria. Next, 20 μl of the resulting supernatant were pipetted onto a second set of capture substrates. After completing the incubations with the antigenic solutions and *ERL*s, the SERS responses and light microscope images of each sample were obtained. The microscope images (data not shown) revealed that: (1) bacteria were bound to the substrates exposed to the whole cell MAP solutions, and (2) no bacteria were detectably captured on the substrates treated with only the supernatant solution. These results indicate that the centrifugation step effectively removes MAP from solution.

Figure 4 summarizes the data obtained from the assays of the whole cell MAP solutions and supernatant from the same solutions after centrifugation. The two data sets plot

SERS intensities of the $\nu_s(NO_2)$ versus the MAP concentration in the original solutions. The two plots, which exhibit an increase in signal with an increase in MAP concentration, are virtually indistinguishable. These findings begin to validate our hypothesis of protein shedding. In other words, there is major membrane protein (MMP) in the whole cell solutions, which can be captured and labeled. Furthermore, the remarkably strong similarity of the two plots argues that shed protein is the overwhelming contributor to the observed responses for the whole cell solutions.

The second experiment further tested the shedding hypothesis by using an in-house designed Raman Microscope and the capture substrates exposed to whole cell MAP. With this instrument, the capture substrate can be translated under the 1.5-μm laser spot to evaluate the signature of a single, captured bacterium or an area of the substrate devoid of bacilli. When the laser illuminated a location free of bacteria, the SERS spectra and calibration curve in Figure 5 were obtained. The spectra in Figure 5a not only have features characteristic of the DSNB-based label, but also undergo intensity changes in-line with the amount of bacteria in the antigen solution. This trend is also evident in the calibration curve in Figure 5b. These data are another strong indicator for the presence of shed protein on the capture surface which, in turn, points to free protein in the whole cell solution.

When the laser was focused on a single bacterium (Figure 6a), a weak, but distinct, spectrum is obtained (Figure 6b). While having a few bands indicative of the Raman reporter molecule, the spectrum also has a broad feature at 1600 cm^{-1}, which we believe originates from the underlying microorganism (57). Upon characterizing 11 individual bacilli from capture substrates exposed to different MAP concentrations, the average intensity for $\nu_s(NO_2)$ was only 170 ±11 cts/2 s.

There are two important conclusions that can be drawn from these results. First, captured bacteria appear to generate a SERS response after *ERL* labeling. Second, the response is much smaller than that observed when interrogating locations devoid of bacilli. In fact, the signal strength from an intact bacterium is on par with that from the blank spectra in Figure 5. These observations are consistent with the overlay of the two plots in Figure 4, and are again an indication that any captured whole cell MAP has, at best, a minor contribution to the SERS signal.

Lastly, these samples were imaged by SEM in order to establish the location of the *ERL*s and bacteria on the capture substrate. The samples were therefore briefly rinsed with deionized water to remove salt residue, dried, sputter coated with gold, and imaged. Shown in Figure 7 are SEM images (~12×9 μm and ~4×3 μm) of a capture substrate that was exposed to 1.3×10^7 MAP/ml. A single bacterium, identified by its rod-like shape (~1×0.5 μm), is evident in the center of both images. There are also several smaller, circular objects that have a size consistent with the 60-nm gold core of the *ERL*s. However, very few *ERL*s appear close enough to the microorganism to be irradiated by the laser when focused on the bacillus. Most of the nanoparticles are comparatively well removed from the bacillus. There were, however, very few nonspecifically bound *ERL*s (~15 in 100 μm^2) on blank samples (0 MAP/ml), and no visible bacteria. These findings further support the likelihood that shed protein is captured by the substrate and that the majority of the response for the whole cell MAP assay arises from *ERL*s bound to shed protein and not captured bacteria.

In summary, studies yield three important conclusions: (1) there is shed protein on the assay surface, (2) the amount of protein increases as the original amount of bacteria in the solution increases, and (3) captured, shed protein can bind *ERL*s. The implications of these

findings to assay performance and the fundamental detection mechanism are discussed in the next section.

DISCUSSION

The work herein, which was designed to build on our assay for MAP sonicate from the companion paper (56), has demonstrated the apparent ability to quantitate heat-killed, whole cell MAP in fewer than 24 hours and at LODs of ~630 MAP/ml in PBS and ~740 MAP/ml in whole milk. While we need to push performance to higher sensitivity to address the need for subclinical levels of detection, this work is our first step towards the creation of a platform for direct evaluation of bacteria levels in milk. Our approach has LODs that are comparable to that recently obtained (~500 CFU/mL) by Stratmann and coworkers, by applying a new peptide-mediated capture PCR method to artificially contaminated milk (49), but our method may potentially be in a more easy-to-use format.

We noted earlier, however, that the LOD for our MAP assay is a few orders of magnitude lower than theoretical expectations. The theoretical detection limit for this assay can be approximated by assuming the lowest level of detection corresponds to a single bacterium present in the laser spot. Since the surface area of the capture substrate is defined by its 3.2-mm diameter, and the laser has a diameter of 25 μm, one bacillus per laser spot equals 1.6×10^4 cells in the assay area. This number of bacteria, when placed in to a 20-μl sample droplet, translates to a detection limit of 8.2×10^5 cells/ml. The projected theoretical LOD is therefore over one thousand times greater than the experimentally determined LOD of ~700 MAP/ml. It is precisely this issue that triggered the investigations that confirmed the presence of the shed MMP targeted by the 13E1 mAb.

The next question rests with the mechanistic origin of shed MMP. Is the protein secreted by the bacillus or is shedding induced by sample preparation? Other *Mycobacteria*, specifically *M. bovis* BCG, are known to release cell wall lipids (40). However, MAP2121c has no signal sequence to suggest secretion and has been previously shown to be associated with the cell membrane (2). It would nonetheless be invaluable to determine if live *Mycobacteria* shed protein.

We believe the observed shedding is caused by sample preparation, with the surface protein being stripped from the bacteria by agitation during heat treatment and/or antigen solution preparation. In fact, a recent study has shown that surface proteins can be readily detached from MAP by brief sonication (44). It is possible that the vortexing step in our sample preparation does exactly that. Nonetheless, shedding leads to an effective approach to signal amplification from individual cells, and we believe is central to the reported detection limits.

These results point to an intriguing new strategy to increase the sensitivity and specificity of various diagnostic tests by harnessing protein shedding. Since it is likely that other MAP proteins are also shed, an approach to enhance the specificity and sensitivity of a test for MAP could potentially be devised by the concurrent detection of multiple surface proteins. To this end, work to further evaluate the shedding process and extend the concept of multiple protein detection is currently underway. In addition, efforts to investigate the applicability of the concept to other bacteria as a general mechanism for signal amplification are planned.

Another intriguing aspect of our MAP assay is its large linear dynamic range, which is at least five orders of magnitude on the log scale. Simple equilibrium models of two-site

immunoassays predict a linearity of only three orders of magnitude in antigen concentration (12). As discussed in work by Plowman *et al.* (39), larger dynamic ranges can arise by the existence of two different ligand-receptor interactions, for example, in the capture step. Thus, the breadth of the dynamic range would be larger than that typically predicted because the stronger interaction would dominate binding at the lower concentrations, followed by capture at the sites with the lower binding strength. Indeed, preliminary results that are based on the Plowman model for the MMP-13E1 interaction (i.e., one strong and one weak binding constant) begin to qualitatively extend the linear dynamic range by another two to three orders of magnitude. Work to fully model these findings is ongoing and will be reported elsewhere.

In conclusion, the performance of our heat-killed, whole cell MAP assay is dominated by the presence of shed surface protein. Due in part to this amplification, our assay allows for a rapid, selective, and sensitive test that can translate to complex sample matrices and thus possibly improve upon current diagnostic tests for Johne's disease. In addition, the quantitative nature of this assay may enable further refinement in definitions of disease stages and progression. Finally, studies to detect MAP from fecal samples as well as monitoring MAP levels in controlled Johne's disease herds are in progress.

ACKNOWLEDGMENTS

We acknowledge Dr. Rachel Millen for expert assistance in obtaining the SEM images and Dr. Jeremy Driskell for valuable discussions. This work was supported by the Institute for Combinatorial Discovery of Iowa State University. The Ames Laboratory is operated for the U.S. Department of Energy by Iowa State University under contract W-

7405-eng-82. We also acknowledge support from USDA-NRI-CAP program "JDIP" to JPB as well as support from the USDA's Agricultural Research Service.

REFERENCES

1. **Ansari, D. O., D. A. Stuart, and S. Nie.** 2005. Surface-enhanced Raman spectroscopic detection of cancer biomarkers in intact cellular specimens. Proc. SPIE **5699:**82-90.
2. **Bannantine, J. P., J. F. Huntley, E. Miltner, J. R. Stabel, and L. E. Bermudez.** 2003. The Mycobacterium avium subsp. paratuberculosis 35 kDa protein plays a role in invasion of bovine epithelial cells. Microbiology **149:**2061-9.
3. **Bannantine, J. P., T. J. Radosevich, J. R. Stabel, S. Berger, J. F. Griffin, and M. L. Paustian.** 2007. Production and Characterization of Monoclonal Antibodies against a major Membrane Protein of Mycobacterium avium subsp. paratuberculosis. Clin. Vaccine Immunol. **14:**312-7.
4. **Beard, P. M., M. J. Daniels, D. Henderson, A. Pirie, K. Rudge, D. Buxton, S. Rhind, A. Greig, M. R. Hutchings, I. McKendrick, K. Stevenson, and J. M. Sharp.** 2001. Paratuberculosis infection of nonruminant wildlife in Scotland. J. Clin. Microbiol. **39:**1517-21.
5. **Beard, P. M., S. M. Rhind, D. Buxton, M. J. Daniels, D. Henderson, A. Pirie, K. Rudge, A. Greig, M. R. Hutchings, K. Stevenson, and J. M. Sharp.** 2001. Natural paratuberculosis infection in rabbits in Scotland. J. Comp. Pathol. **124:**290-9.
6. **Burton, M. S., J. H. Olsen, R. L. Ball, and G. A. Dumonceaux.** 2001. Mycobacterium avium subsp. paratuberculosis infection in an addax (Addax nasomaculatus). J. Zoo. Wildl. Med. **32:**242-4.
7. **Cao, Y. C., R. Jin, and C. A. Mirkin.** 2002. Nanoparticles with Raman spectroscopic fingerprints for DNA and RNA detection. Science **297:**1536-40.
8. **Clarke, C. J., I. A. Patterson, K. E. Armstrong, and J. C. Low.** 1996. Comparison of the absorbed ELISA and agar gel immunodiffusion test with clinicopathological findings in ovine clinical paratuberculosis. Vet. Rec. **139:**618-21.
9. **Colgrove, G. S., C. O. Thoen, B. O. Blackburn, and C. D. Murphy.** 1989. Paratuberculosis in cattle: a comparison of three serologic tests with results of fecal culture. Vet. Microbiol. **19:**183-7.
10. **Cousins, D. V., R. Whittington, I. Marsh, A. Masters, R. J. Evans, and P. Kluver.** 1999. Mycobacteria distinct from Mycobacterium avium subsp. paratuberculosis isolated from the faeces of ruminants possess IS900-like sequences detectable by IS900 polymerase chain reaction: implications for diagnosis. Mol. Cell. Probes **14:**431-442.
11. **Dargatz, D. A., B. A. Byrum, L. K. Barber, R. W. Sweeney, R. H. Whitlock, W. P. Shulaw, R. H. Jacobson, and J. R. Stabel.** 2001.

Evaluation of a commercial ELISA for diagnosis of paratuberculosis in cattle. J. Am. Vet. Med. Assoc. **218:**1163-6.

12. **Diamandis, E. P., and T. K. Christopoulos (ed.).** 1996. Immunoassay. Academic Press, San Diego.
13. **Dou, X., T. Takama, Y. Yamaguchi, and H. Yamamoto.** 1997. Enzyme Immunoassay Utilizing Surface-Enhanced Raman Scattering of the Enzyme Reaction Product. Anal. Chem. **69:**1492-1495.
14. **Driskell, J. D., K. M. Kwarta, R. J. Lipert, M. D. Porter, J. D. Neill, and J. F. Ridpath.** 2005. Low-level detection of viral pathogens by a surface-enhanced Raman scattering based immunoassay. Anal. Chem. **77:**6147-54.
15. **Duhachek, S. D., J. R. Kenseth, G. P. Casale, G. J. Small, M. D. Porter, and R. Jankowiak.** 2000. Monoclonal antibody--gold biosensor chips for detection of depurinating carcinogen--DNA adducts by fluorescence line-narrowing spectroscopy. Anal. Chem. **72:**3709-16.
16. **Dukes, T. W., G. J. Glover, B. W. Brooks, J. R. Duncan, and M. Swendrowski.** 1992. Paratuberculosis in saiga antelope (Saiga tatarica) and experimental transmission to domestic sheep. J. Wildl. Dis. **28:**161-70.
17. **Ellingson, J. L. E., J. R. Stabel, W. R. Bishai, R. Frothingham, and J. M. Miller.** 2000. Evaluation of the accuracy and reproducibility of a practical PCR panel assay for rapid detection and differentiation of Mycobacterium avium subspecies. Mol. Cell. Probes **14:**153-161.
18. **Faulds, K., W. E. Smith, and D. Graham.** 2005. DNA detection by surface enhanced resonance Raman scattering (SERRS). Analyst **130:**1125-31.
19. **Garrell, R. L.** 1989. Surface-enhanced Raman spectroscopy. Anal. Chem. **61:**401A-402A, 404A, 406A-408A, 410A-411A.
20. **Godfroid, J., C. Delcorps, L. M. Irenge, K. Walravens, S. Marche, and J. L. Gala.** 2005. Definitive differentiation between single and mixed mycobacterial infections in red deer (Cervus elaphus) by a combination of duplex amplification of p34 and f57 sequences and Hpy188I enzymatic restriction of duplex amplicons. J. Clin. Microbiol. **43:**4640-8.
21. **Graham, D., B. J. Mallinder, D. Whitcombe, N. D. Watson, and W. E. Smith.** 2002. Simple multiplex genotyping by surface-enhanced resonance Raman scattering. Anal. Chem. **74:**1069-74.
22. **Grubisha, D. S., R. J. Lipert, H. Y. Park, J. Driskell, and M. D. Porter.** 2003. Femtomolar detection of prostate-specific antigen: an immunoassay based on surface-enhanced Raman scattering and immunogold labels. Anal. Chem. **75:**5936-43.
23. **Harris, N. B., and R. G. Barletta.** 2001. Mycobacterium avium subsp. paratuberculosis in Veterinary Medicine. Clin. Microbiol. Rev. **14:**489-512.
24. **Hendrick Steven, H., E. Duffield Todd, E. Kelton David, E. Leslie Ken, D. Lissemore Kerry, and M. Archambault.** 2005. Evaluation of enzyme-linked immunosorbent assays performed on milk and serum samples for detection of paratuberculosis in lactating dairy cows. J. Am. Vet. Med. **226:**424-8.

25. **http://johnes.vetmed.wisc.edu/** copyright 2001, Johne's Information Center. University of Wisconsin - School of Veterinary Medicine. accessed May 28, 2007.
26. **Jones, V. W., J. R. Kenseth, M. D. Porter, C. L. Mosher, and E. Henderson.** 1998. Microminiaturized immunoassays using atomic force microscopy and compositionally patterned antigen arrays. Anal. Chem. **70:**1233-41.
27. **Judge, J., I. Kyriazakis, A. Greig, D. J. Allcroft, and M. R. Hutchings.** 2005. Clustering of Mycobacterium avium subsp. paratuberculosis in rabbits and the environment: how hot is a hot spot? Appl. Environ. Microbiol. **71:**6033-8.
28. **Kelly, K. L., E. Coronado, L. L. Zhao, and G. C. Schatz.** 2003. The Optical Properties of Metal Nanoparticles: The Influence of Size, Shape, and Dielectric Environment. J. Phys. Chem. B **107:**668-677.
29. **Kneipp, K., H. Kneipp, I. Itzkan, R. R. Dasari, and M. S. Feld.** 2002. Surface-enhanced Raman scattering and biophysics. J. Phys.: Condens. Matter **14:**R597-R624.
30. **Kneipp, K., H. Kneipp, I. Itzkan, R. R. Dasari, and M. S. Feld.** 1999. Ultrasensitive chemical analysis by Raman spectroscopy. Chem. Rev. **99:**2957-2975.
31. **Lambeth, C., L. A. Reddacliff, P. Windsor, K. A. Abbott, H. McGregor, and R. J. Whittington.** 2004. Intrauterine and transmammary transmission of Mycobacterium avium subsp paratuberculosis in sheep. Aust. Vet. J. **82:**504-8.
32. **Machackova-Kopecna, M., M. Bartos, M. Straka, V. Ludvik, P. Svastova, J. Alvarez, J. Lamka, I. Trcka, F. Treml, I. Parmova, and I. Pavlik.** 2005. Paratuberculosis and avian tuberculosis infections in one red deer farm studied by IS900 and IS901 RFLP analysis. Vet. Microbiol. **105:**261-8.
33. **Mackintosh, C. G., G. W. de Lisle, D. M. Collins, and J. F. Griffin.** 2004. Mycobacterial diseases of deer. N. Z. Vet. J. **52:**163-74.
34. **Mulvaney, S. P., M. D. Musick, C. D. Keating, and M. J. Natan.** 2003. Glass-Coated, Analyte-Tagged Nanoparticles: A New Tagging System Based on Detection with Surface-Enhanced Raman Scattering. Langmuir **19:**4784-4790.
35. **Muskens, J., D. Bakker, J. de Boer, and L. van Keulen.** 2001. Paratuberculosis in sheep: its possible role in the epidemiology of paratuberculosis in cattle. Vet. Microbiol. **78:**101-9.
36. **Ni, J., R. J. Lipert, G. B. Dawson, and M. D. Porter.** 1999. Immunoassay readout method using extrinsic Raman labels adsorbed on immunogold colloids. Anal. Chem. **71:**4903-8.
37. **Park, H.-Y.** 2005. Chip-scale Bioassays Based on Surface-enhanced Raman Scattering: Fundamentals and Applications. Ph.D. thesis. Iowa State University, Ames, IA.

38. **Park, H.-Y., R. J. Lipert, and M. D. Porter.** 2004. Single Particle Raman Measurements of Gold Nanoparticles Used in Surface-Enhanced Raman Scattering (SERS)-Based Sandwich Immunoassays. Proc. SPIE **5593:**464.
39. **Plowman, T. E., W. M. Reichert, C. R. Peters, H. K. Wang, D. A. Christensen, and J. N. Herron.** 1996. Femtomolar sensitivity using a channel-etched thin film waveguide fluoroimmunosensor. Biosens Bioelectron **11:**149-60.
40. **Rhoades, E., F.-F. Hsu, J. B. Torrelles, J. Turk, D. Chatterjee, and D. G. Russell.** 2003. Identification and macrophage-activating activity of glycolipids released from interacellular *Mycobacterium bovis* BCG. Mol. Microbiol. **48:**875-888.
41. **Rohr, T. E., T. Cotton, N. Fan, and P. J. Tarcha.** 1989. Immunoassay employing surface-enhanced Raman spectroscopy. Anal. Biochem. **182:**388-98.
42. **Schatz, G. C., and R. P. Van Duyne.** 1980. Image field theory of enhanced Raman scattering by molecules adsorbed on metal surfaces: detailed comparison with experimental results. Surf. Sci. **101:**425-38.
43. **Sergeant, E. S., R. J. Whittington, and S. J. More.** 2002. Sensitivity and specificity of pooled faecal culture and serology as flock-screening tests for detection of ovine paratuberculosis in Australia. Prev. Vet. Med. **52:**199-211.
44. **Speer, C. A., M. C. Scott, J. P. Bannantine, W. R. Waters, Y. Mori, R. H. Whitlock, and S. Eda.** 2006. A novel enzyme-linked immunosorbent assay for diagnosis of Mycobacterium avium subsp. paratuberculosis infections (Johne's disease) in cattle. Clin. Vaccine Immunol. **13:**535-540.
45. **Stabel, J. R.** 1998. Johne's disease: a hidden threat. J. Dairy Sci. **81:**283-8.
46. **Stabel, J. R., S. J. Wells, and B. A. Wagner.** 2002. Relationships between fecal culture, ELISA, and bulk tank milk test results for Johne's disease in US dairy herds. J. Dairy Sci. **85:**525-531.
47. **Storset, A. K., I. Berg, and B. Djonne.** 2005. Evaluation of the gamma interferon test for diagnosis of paratuberculosis in goats. Vet Immunol. Immunopathol. **107:**87-94.
48. **Storset, A. K., H. J. Hasvold, M. Valheim, H. Brun-Hansen, G. Berntsen, S. K. Whist, B. Djonne, C. M. Press, G. Holstad, and H. J. Larsen.** 2001. Subclinical paratuberculosis in goats following experimental infection. An immunological and microbiological study. Vet Immunol. Immunopathol. **80:**271-87.
49. **Stratmann, J., K. Dohmann, J. Heinzmann, and G.-F. Gerlach.** 2006. Peptide aMptD-mediated capture PCR for detection of Mycobacterium avium subsp. paratuberculosis in bulk milk samples. Appl. Environ. Microbiol. **72:**5150-5158.
50. **Stratmann, J., B. Strommenger, K. Stevenson, and G.-F. Gerlach.** 2002. Development of a peptide-mediated capture PCR for detection of Mycobacterium avium subsp. paratuberculosis in milk. J. Clin. Microbiol. **40:**4244-4250.

51. **Vo-Dinh, T.** 1998. Surface-enhanced Raman spectroscopy using metallic nanostructures. Trends Anal. Chem. **17:**557-582.
52. **Wagner, P., M. Hegner, P. Kernen, F. Zaugg, and G. Semenza.** 1996. Covalent immobilization of native biomolecules onto Au(111) via N-hydroxysuccinimide ester functionalized self-assembled monolayers for scanning probe microscopy. Biophys. J. **70:**2052-2066.
53. **Whitlock, R. H., S. J. Wells, R. W. Sweeney, and J. Van Tiem.** 2000. ELISA and fecal culture for paratuberculosis (Johne's disease): sensitivity and specificity of each method. Vet. Microbiol. **77:**387-98.
54. **Whittington, R. J., I. B. Marsh, and R. H. Whitlock.** 2001. Typing of IS 1311 polymorphisms confirms that bison (Bison bison) with paratuberculosis in Montana are infected with a strain of Mycobacterium avium subsp. paratuberculosis distinct from that occurring in cattle and other domesticated livestock. Mol. Cell. Probes **15:**139-45.
55. **Xu, S., X. Ji, W. Xu, X. Li, L. Wang, Y. Bai, B. Zhao, and Y. Ozaki.** 2004. Immunoassay using probe-labelling immunogold nanoparticles with silver staining enhancement via surface-enhanced Raman scattering. Analyst **129:**63-8.
56. **Yakes, B. J., R. J. Lipert, J. P. Bannantine, and M. D. Porter.** in preparation. Detection of Mycobacterium avium subsp. paratuberculosis using Surface-Enhanced Raman Scattering: Part I - Sonicate Immunoassay. Clin. Vaccine Immunol.
57. **Zeiri, L., and S. Efrima.** 2005. Surface-enhanced Raman spectroscopy of bacteria: the effect of excitation wavelength and chemical modification of the colloidal milieu. J. Raman Spectrosc. **36:**667-675.
58. **Zeman, E. J., and G. C. Schatz.** 1987. An accurate electromagnetic theory study of surface enhancement factors for silver, gold, copper, lithium, sodium, aluminum, gallium, indium, zinc, and cadmium. J. Phys. Chem. **91:**634-43.
59. **Zhang, X., M. A. Young, O. Lyandres, and R. P. Van Duyne.** 2005. Rapid detection of an anthrax biomarker by surface-enhanced Raman spectroscopy. J. Am. Chem. Soc. **127:**4484-9.

FIGURES

FIG. 1. Schematic of sandwich immunoassay for MAP bacilli and illustration of shed protein assay format.

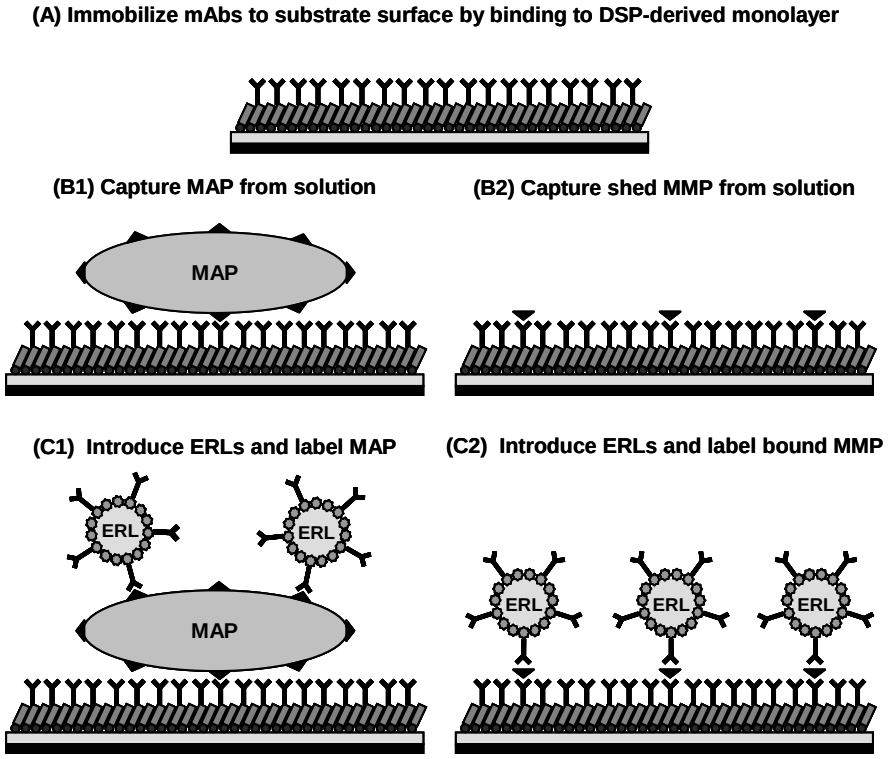

FIG. 2. Spectra and calibration curve for MAP spiked PBS samples. (A) Spectra (vertically offset for clarity) with intensity in counts (cts) per 5 s and (B) corresponding calibration curve using $\nu_s(NO_2)$ intensity. Dashed line corresponds to the blank plus three times its standard deviation. Best fit line is y=913x-1568, R^2=0.98.

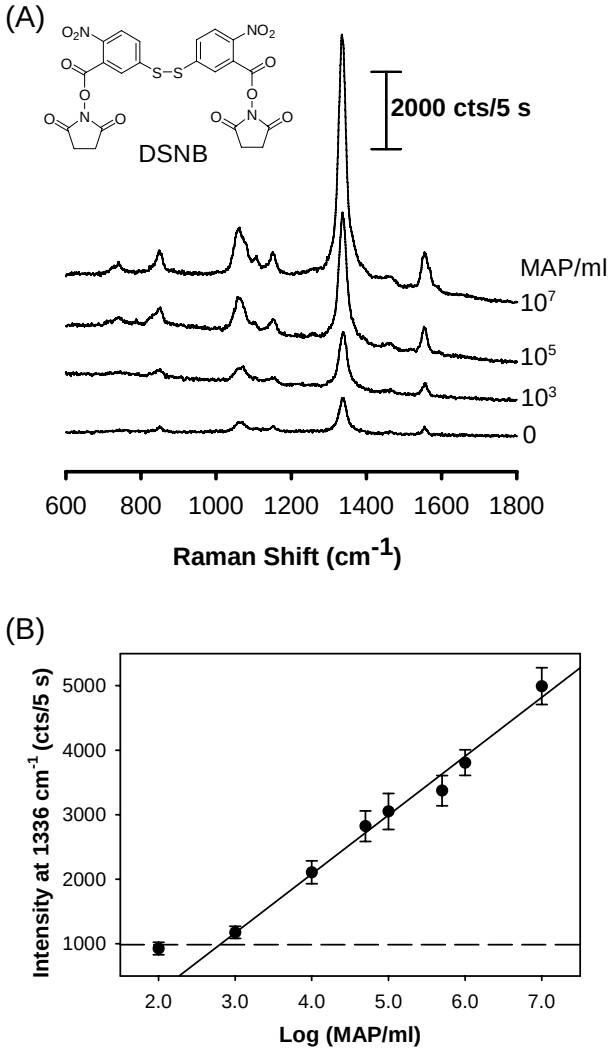

FIG. 3. Calibration curve for whole cell MAP in a milk matrix. Same trend as observed in FIG. 2 (1 s integration, y=281x-395, R^2=0.95) with increasing SERS intensity with increasing MAP in the antigen solution. Dashed line corresponds to the blank plus three times its standard deviation.

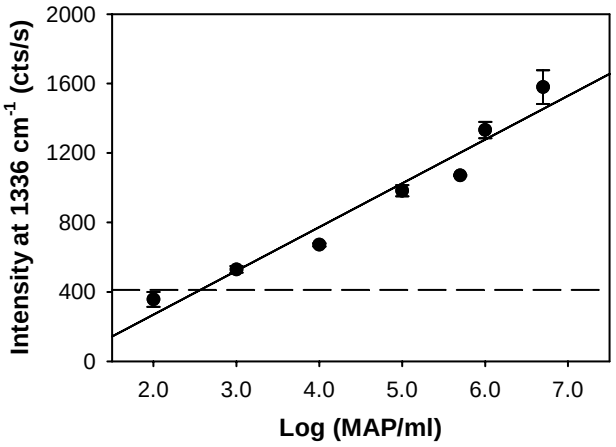

FIG. 4. SERS intensity of whole cell MAP solutions compared to supernatant of these solutions after bacteria have been pelleted out. The points from the two assays, whole cell MAP and supernatant without MAP, coincide. Dashed line corresponds to the blank plus three times its standard deviation.

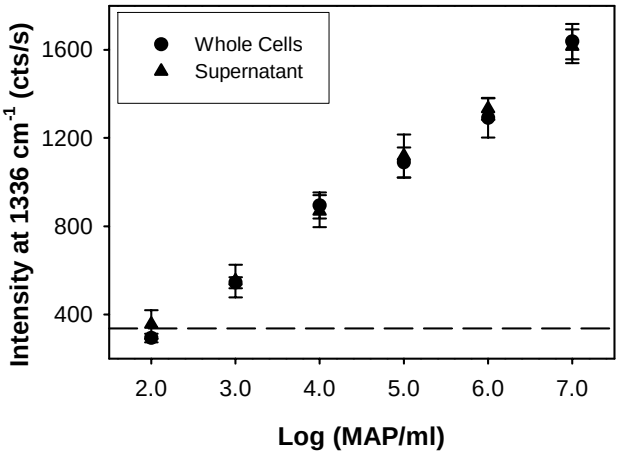

FIG. 5. (A) Spectra vertically offset for clarity and (B) corresponding calibration curve from Raman microscope measurements of areas between bacteria on the assay substrate. Signals from areas devoid of bacteria increased with increased MAP in the antigen solution indicating that *ERL*s were specifically bound to the substrate surface. Dashed line corresponds to the blank plus three times its standard deviation.

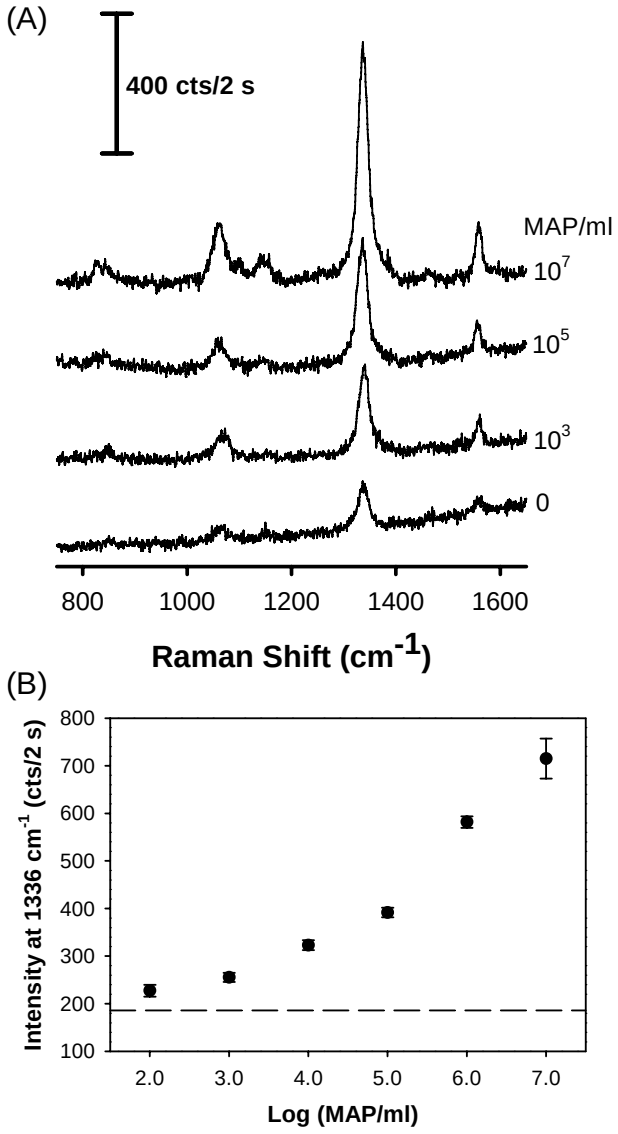

FIG. 6. (A) Laser spot from 100× objective over a single bacterium and (B) SERS spectrum from the single bacterium with bound *ERL*s obtained with the Raman microscope. The bacterium had a SERS spectrum containing the distinct spectra features of the DSNB-derived Raman reporter indicating that *ERL*s were also bound to the bacteria.

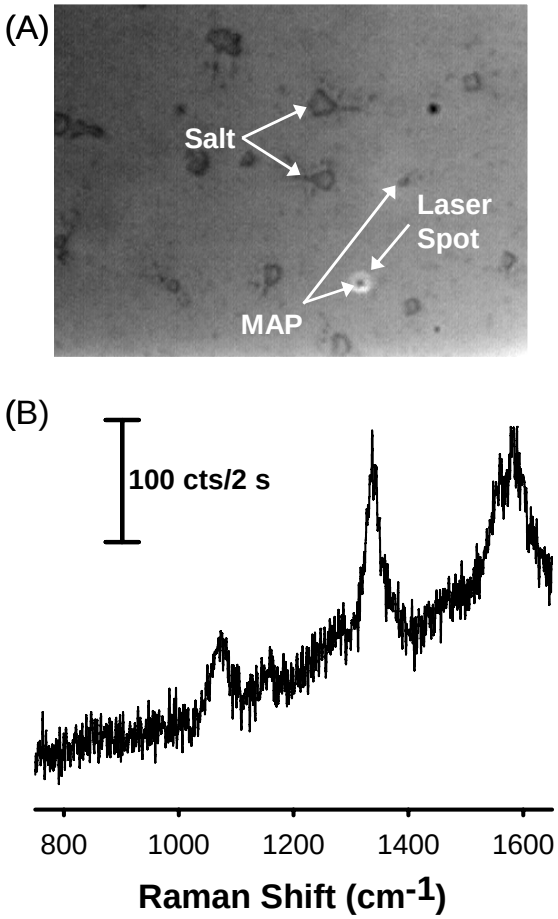

FIG. 7. SEM images of an assay platform exposed to 1.3×10^7 MAP/mL and 60-nm *ERL*s with (A) bacterium in the center and (B) and expanded area from box in (A). Results visually confirm spectroscopy measurements in FIG. 5 and 6.

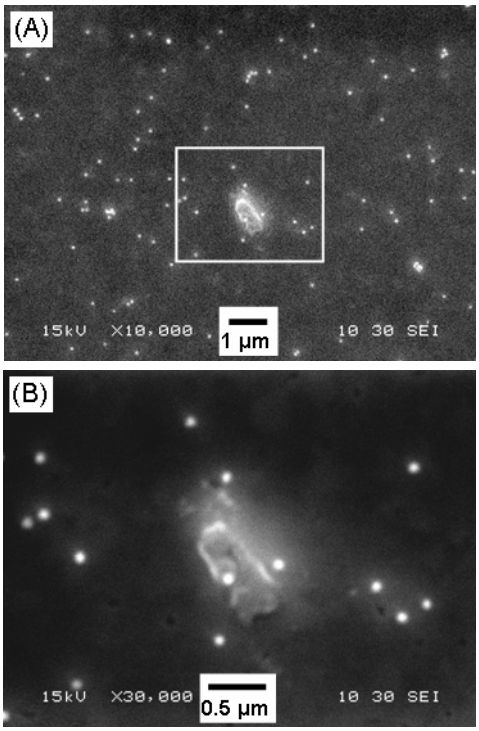

CHAPTER 4: Resonant Raman Labels for Improved Surface-Enhanced Raman Scattering Heterogeneous Immunoassays

Betsy Jean Yakes[a,b], Jeremy Driskell[c], Robert J. Lipert[1], and Marc D. Porter[a,b]

[a] Departments of Chemistry and Chemical and Biological Engineering, Ames Laboratory-USDOE, and Institute for Combinatorial Discovery, Iowa State University, Ames, IA 50011

[b] Biodesign Institute – Center for Combinatorial Sciences and Department of Chemistry and Biochemistry, Arizona State University, Tempe, AZ 85287-6401

[c] Department of Chemistry, University of Georgia, Athens, GA 30602-2556

A paper to be submitted to *Analytica Chimica Acta*

ABSTRACT

Assays based on surface-enhanced Raman scattering (SERS) as a readout tool have recently begun to incorporate the resonance Raman effect. By integrating this concept of surface-enhanced resonance Raman scattering (SERRS) into a heterogeneous immunoassay platform, stronger signals can be realized that may also lead to lower levels of detection. This paper therefore focuses on incorporating organic dyes as reporter molecules that are tethered to 60-nm colloidal gold which is also coated with antibodies. When performing assay comparisons, resonant molecules (i.e., Alexa Fluor 647, 5-(and-6)-carboxynaphthofluorescein, and Cy5, and malachite green isothiocyanate) yield signal enhancements of ~100 to 350 times compared to the nonresonant 5, 5'-dithiobis (succinimidyl-2-nitrobenzoate), which is used as a reference. This paper details the development of stable colloidal gold suspensions through the optimization of labeling reactions and pH, presents SERRS spectra for four resonant dyes, and examines the immunoassay performance with respect to detection limits and nonspecific adsorption.

Keywords: SERS, heterogeneous immunoassays, resonant Raman, enhancement, nanoparticle stability

INTRODUCTION

The importance of biomolecule detection is undergoing a nearly explosive growth in clinical, environmental, agricultural, and defense arenas.[1] The motivation behind this emerging emphasis reflects, in part, the role of rapid, cost-effective, sensitive, and selective immunoassays as applied to early disease detection and homeland security. One detection technique that has attributes in tune with these needs is surface-enhanced Raman scattering (SERS). In SERS, incident electromagnetic radiation couples with the surface plasmon oscillation of a roughened metal surface and an adsorbed Raman active molecule. SERS was first observed in 1974 by Fleischmann and coworkers,[2] but not fully recognized until 1977 by Jeamarie and Van Duyne[3] and by Albrecht and Creighton.[4] SERS relies on a combination of chemical[5-7] and electromagnetic[8-10] enhancement effects that combine to yield signals up to 10^{14} times larger than normal Raman scattering.[11]

SERS as a readout tool for immunoassays has several notable attributes that make it a potentially attractive alternative to traditional techniques such as colorimetry, radioisotope decay, and fluorescence.[8,12,13] First, SERS intensities have been shown to rival that of fluorescence while having much narrower bands. This advantage allows for sensitive (pico/femtomolar)[14] biolyte detection while enabling multiplexed detection[13] due to less spectral overlap. In addition, Raman scattering is a versatile technique that has minimal fluorophore photobleaching, since the excitation state has an extremely short lifetime. This

excitation wavelength is substrate but not scattering molecule dependent, so a single excitation source can be used.[15] Finally, SERS is a robust readout method that is unaffected by the surrounding environment (e.g., quenchers, pH, ionic strength) which then allows for a more reproducible signal intensity.

In an attempt to obtain stronger SERS signals and, by extension, possibly even higher sensitivities, approaches based on surface-enhanced resonant Raman scattering (SERRS) have begun to appear.[16-25] This phenomenon occurs when an immobilized Raman active molecule has an electronic transition that is in resonance with the excitation photon. This condition leads to the higher adsorption of the incident energy, a larger probability for scattering, and, therefore, larger signal intensities.[26]

Based on these attributes, SERRS has begun to gain popularity as a readout method in immunoassays and gene detection assays. Mirkin and colleagues[17,18,25] have prepared silver coated-gold nanoparticle probes that contain a Raman dye for SERRS detection of oligonucleotides and proteins. By selectively tagging DNA with a SERRS active molecule, Vo-Dinh and coworkers[19] have performed gene diagnostics through hybridization of the probes to complementary DNA-coated, silver chips. Graham and coworkers have reported the SERS-based detection of tagged PCR products[23] and dye-labeled oligonucleotides via silver nanoparticles.[21] In conjunction with that work, they have also developed benzotriazole dye-silver nanoparticle conjugation chemistry.[22] Advances in colloidal stability have been achieved by Natan and colleagues[24] through glass-coated, reporter encased, metal nanoparticles that are then used in bioassays. Furthermore, Nie and coworkers [16,20] have also used a silica shell – dye embedded, nanoparticle core approach for detection of cancer markers.

While demonstrating the strengths of using SERRS, many of the above methods do not optimally position the dye on the enhancing substrate. Minimizing the distance between the SERS surface and the reporter is essential because the electromagnetic SERS enhancement decays rapidly with respect to the distance, d, from the substrate (i.e., d^{-10} or d^{-12})[9,27]. Furthermore, when the dye is directly adsorbed on the nanoparticle, methods to stabilize the colloid against aggregation (i.e. silica encapsulation) are necessary. This paper seeks to address both challenges through investigating covalently attached dye molecules on a gold surface in an attempt to increase SERRS signals without any post-formation stabilization steps. These stabilized labels will then be incorporated into an immunoassay in order to determine the enhancement achieved.

As part of our interests in this area, we have used variants of the platform shown in Figure 1 for the detection of small proteins[13,28], cancer markers[14], viruses[29,30], bacteria[31-33], and spores[33]. For the work herein, the two site, heterogeneous immunoassay begins, as shown, by coupling mouse-IgG antibody to the adsorbed thiolate of dithiobis(succinimidyl propionate) (DSP) through succinimidyl ester chemistry. When the respective antigen is present, the capture substrate will selectively extract mouse-IgG from solution. After a rinse step, the substrate is exposed to a solution of extrinsic Raman labels (*ERL*s) which selectively label the captured antigen. In this case, the *ERL*s are formed by adsorbing anti-mouse IgG to a portion of the gold nanoparitcle surface and then coating the remaining gold surface with the Raman reporter molecule.

As few studies have focused on comparing SERRS immunoassays with their nonresonant counterpart via changing only the molecular label, four commercially available organic dyes that have excitation maxima near resonance with the HeNe laser wavelength

(632.8 nm) will be compared with our well-characterized, nonresonant label 5,5'-dithiobis (succinimidyl-2-nitrobenzoate) (DSNB). The resonant molecules, given in Table 1, were chosen to represent the diversity of commercially available dyes. As such, multiple functional groups (i.e., succinimidyl ester or isothiocyanate) and charge states (i.e., net positive or negative charge) were tested. This work details the development of stable resonant dye *ERL*s without the need for post-formation modification procedures, integrates the four resonant and one nonresonant (DSNB) label into an immunoassay, and evaluates the performance of the resonant *ERL*s versus the DSNB *ERL*s.

EXPERIMENTAL

2.1. Chemicals and Reagents

Colloidal, 60-nm gold nanoparticles (2.6×10^{10} particles/mL, <8% variation in diameter), were purchased from Ted Pella (Redding, CA). ImmunoPure® mouse IgG and ImmunoPure® Goat anti-mouse IgG (minimum cross reactivity with human, bovine, and horse serum proteins) were obtained from Pierce Biotechnology (Rockford, IL). Porcine parvovirus (PPV, 6.4×10^6 $TCID_{50}$/10 mL of 10 mM PBS) and PPV antibody (~1.4 mg/mL in 50 mM borate buffer) were provided by the National Animal Disease Center (Ames, IA). Bovine serum albumin (BSA), 2-aminoethanethiol (AET), octadecanethiol (ODT), dithiobis(succinimidyl propionate) (DSP), and sodium chloride were procured from Sigma-Aldrich (St. Louis, MO).

For preparation of template stripped gold (TSG), silicon wafers (4-in, p-type, [111] test grade wafer) were obtained from University Wafer (South Boston, MA), Epo-tek 377

part A and B epoxy was supplied by Epo-tek (Billerica, MA), and poly(dimethylsiloxane) (PDMS) was purchased from Dow Corning (Midland, MI).

The nonresonant Raman label (DSNB) was synthesized according to our previous procedure.[14] Resonant Raman dyes were purchased from Molecular Probes (malachite green isothiocyanate (M689), Alexa Fluor® 647 carboxylic acid, succinimidyl ester (AF647), and 5-(and-6)-carboxynaphthofluorescein, succinimidyl ester (CNF); Carlsbad, CA) or Amersham Biosciences (Cy5 Mono NHS ester (Cy5); Piscataway, NJ).

Distilled water, subsequently deionized with a Millipore Milli-Q system (18 MΩ, Billerica, MA), was used for the preparation of all aqueous reagents and buffers. Ethanol was acquired from Aaper (Shelbyville, KY). Acetonitrile was procured from Fisher (Pittsburgh, PA). Borate buffer powder packs (50 mM, pH 8.3) were purchased from Pierce while phosphate buffered saline powder packs (PBS, 10 mM, pH 7.4) were obtained from Sigma-Aldrich; both were diluted as needed. SuperBlock was obtained from Pierce.

Buffers were prepared according to standard protocol with PBS used for pH 7-7.5, borate buffer for pH 8-9, sodium tetraborate decahydrate (certified ACS, Fisher) buffer for pH 9.5-10, and sodium carbonate (Fisher) buffer for pH 10.5-11. An Orion model 520A pH meter (Boston, MA), calibrated with pH 7.00 and 10.00 standards, was used for all measurements with slight pH adjustments made by addition of aqueous sodium hydroxide (certified ACS, Fisher) or sulfuric acid (ACS grade, EMD Chemicals, Gibbstown, NJ).

2.2. Thiol Modification of the Dyes

To direct the immobilization of the dyes to the gold nanoparticles, AET was used to convert the succinimidyl ester terminated compounds (Cy5, AF647, CNF) or isothiocyanate

molecules (M689) to thiols or thioureas, respectively, as shown in Figure 2.[34] For these reactions, Cy5 was dissolved in water while all other dyes used DMSO; the resulting concentrations spanned 0.2 to 1 mM. AET was selected as the tethering molecule since its two-carbon chain minimizes the gap between the surface of the gold nanoparticle and label. For these reactions, one mole of dye was mixed with 0.9 moles of AET for ~90 min. Once prepared, the thiol-modified dye solutions were stored in the dark at 4°C and could be used for six months with no observable decrease in Raman signal. We note that the slight excess dye molecules proved important, as the presence of unreacted AET destabilized the nanoparticle suspension.

2.3. Extrinsic Raman Label (ERL) Preparation

Labeling procedures to determine optimum conditions for nanoparticle stability were studied, and the outcomes of the investigations are presented in the Results section. Briefly, the six labeling methods tested are summarized in Table 2. All nanoparticle solutions consisted of 500 µL of 60-nm colloidal gold mixed with 20 µL of 50 mM borate buffer. The AF647 and AF647-AET solutions had a final concentration of 0.2 mM in DMSO. Method 1 is our standard *ERL* preparation in which the nanoparticles were reacted with 5 µL of DSNB (8 h incubation) followed by 10 µL of Ab (14 h incubation). Method 2 consisted of: (1) 3.5 µL of 1 mg/mL AF647 in DMSO reacting with 50 µL of PPV Ab in borate buffer for 1 h; and (2) adding 10 µL of the antibody-AF647 solution to the suspension. Methods 3 and 4 started by absorbing 10 µL of Ab to the nanoparticles (8 h) and were followed by reacting either 5 µL of AF647 or 5 µL of AET-coupled AF647 for 14 h. Methods 5 and 6 reversed

Methods 3 and 4 by incubating AF647 or AF647-AET for 8 h and then adding antibody (14 h).

From this and other studies discussed in more detail in the Results section, an optimum labeling procedure was determined to consist of first adding 1 mL of 60-nm particles to a centrifuge vial and buffering the solution with 40 µL of 50 mM borate buffer (pH 8.3) or 200 µL of 10 mM sodium borate buffer (pH 9.5). To this solution, 11.1 µL of anti-mouse IgG (1.8 mg/mL) were added and incubated for 7 h. After adsorbing the antibody, 20 µL of 1 mM reporter solution (DSNB in acetonitrile; Cy5-AET in water; or AF647-AET, CNF-AET, M689-AET in DMSO) were reacted for ~14 h. This process formed a gold-bound thiolate between the nanoparticles and Raman scatterers. Finally, 100 µL of a 10% BSA in 2 mM borate buffer were added to the solution in order to minimize nonspecific binding.

In order to remove excess, reagents, the mixture was first centrifuged at 2,000*g* for 10 min (Eppendorf MiniSpin, Westbury, NY). Next, the supernatant solution was removed, and the loose *ERL* pellet was resuspended in 1000 µL of 2 mM borate buffer with 1% BSA. This process was repeated three times with the final resuspension in 500 µL. Finally, 50 µL of 10% NaCl were added to the colloidal suspension to match biological conditions, and the solution was filtered through a 0.22-µm syringe filter (Costar, Fisher) in order to remove large clusters of nanoparticles.

2.4. Capture Substrate Preparation

The substrate platform and immunoassay protocol have been reported previously.[13,14,29,33] Briefly, gold templates were prepared by resistively evaporating 99.9% pure gold (~300 nm, 0.1 to 0.2 nm/s rate) onto a silicon wafer using an Edwards 306A

evaporator (Wilmington, MA). Clean 1×1 cm glass slides were affixed to the gold surface by Epo-tek 377 part A and B epoxy and cured at 150°C for 1.75 h. The resulting template stripped gold (TSG) slides were then gently removed from the wafer. The freshly exposed TSG surface was then stamped with an ODT-soaked PDMS stamp that contained a 3.2-mm diameter centered hole. This process forms a hydrophobic barrier surrounding the 3.2-mm assay area. TSG was then exposed to 1 mM, ethanolic DSP for 14 h and subsequently to 20 μL of anti-mouse IgG (100 μg/mL, 7 h) thus forming an amide linkage through the succinimidyl esters of the DSP and primary amines on the antibody. The substrates were then rinsed with 2 mL of 10 mM PBS buffer, and the unreacted succinimidyl endgroups of the DSP-derived monolayer were blocked with SuperBlock overnight.

2.5. Immunoassay Procedure

Capture substrates were exposed to varying concentrations of mouse IgG in 10 mM PBS buffer (pH 7.4) for 6 h (room temperature) in a humidity chamber. After rinsing three times with 2 mM borate buffer (pH 8.3) with 150 mM NaCl, the *ERL*s were added and allowed to react ~14 h. Finally, the substrates were rinsed with the same borate buffer and gently dried under a stream of nitrogen.

2.6. UV-Vis Spectroscopy

UV-Visible transmission spectra of nanoparticle solutions were collected using a Hewlett-Packard model 8435 spectrophotometer. The pathlength of the quartz cuvette was 1.0 cm. The sample cell was rinsed twice with deionized water and dried between measurements. The reference solution consisted of 2 mM borate buffer and 1% BSA.

2.7. Zeta Potential Measurements

A Malvern ZetaSizer Nano Z (Southboro, MA) was used to correlate the zeta potential of the *ERL*s and colloidal stability. The instrument was calibrated with the Malvern Zeta transfer solution, and the -46.1 mV result was within the accepted -50±5 mV range. *ERL*s were prepared following the standard procedure, including centrifugation and resuspension, but without salt addition and filtration. Three replicate measurements at 25°C were performed in all cases. Between samples, the cell was rinsed five times with deionized water (5 mL per wash). By measuring the electrophoretic mobility of the particles, the zeta potential can be calculated by the Henry equation and the Smoluchowski approximation.[35]

2.8. SERS Instrument

SERS spectra for the immunoassay were collected using a *NanoRaman*^{TM}I (Concurrent Analytical, Waimanalo, HI). This instrument consists of a HeNe laser (632.8 nm, 30 mW, 491 μm^2 spot size), fiber-optic-based probe head, thermoelectrically cooled CCD (Kodak 0401 E, 0°C), and an *f*/2.0 Czerny-Turner imaging spectrometer (6-8 cm^{-1} resolution). Normal incident laser light was focused onto the substrate surface with a 0.68 numerical objective that also collected the scattered radiation. Exposure times were 1-s for DSNB and 0.2-s for the dye-labeled nanoparticles, and spectral data were evaluated with the TRCommander 1.3.0 software. Spectra were baseline corrected with Omnic 6.2 (Thermo Electron Corporation) software to remove the continuum underneath Raman lines.[36]

RESULTS AND DISCUSSION

3.1. Preparation of ERLs

The Raman reporter molecule, DSNB, was used to prepare *ERL*s that served as a comparative standard. This nonresonant molecule chemisorbs to the gold surface through cleavage of the disulfide bond and subsequent formation of a gold-bound thiolate. Since the dye reporter molecules do not have a functional group for direct binding to the gold surface, methods to allow both the Abs and the reporter molecule to adsorb to the nanoparticles were investigated. In addition, the order of adding Abs and reporter molecules was investigated to determine the optimum *ERL* formation procedure with respect to stability and SERS signal intensity.

Six labeling methods were compared and are outlined in Table 2. For these studies, PPV antibody and PPV (a nonenveloped, 25-nm virus) were used in place of anti-mouse and mouse IgG, but the immunoassay protocol remained the same. This study asked three fundamental questions: (1) Is it possible to label the antibody with the dye molecule prior to being added to the nanoparticles (Method 2) and obtain a SERS signal, (2) Does the dye have to be preconjugated with AET in order to react with the nanoparticles (Method 3 compared with Method 4 (i.e. Methods 3/4) and Methods 5/6), and (3) What order of addition of Ab and dye yields stable *ERL*s and large SERS signals (Methods 3/5 and Methods 4/6)? Method 1 represents the DSNB labeled nanoparticles as a standard solution.

Following Steps 1 and 2, BSA blocking, centrifugation/resuspension, and NaCl additions were all performed, and the UV-Vis spectra of the *ERL* solutions were recorded. All *ERL*s, except for Method 5, were red in color and had a single UV-Vis band at ~538 nm. These characteristics indicate that the nanoparticles were not detectably aggregated.

However, the *ERL*s from Method 5 (AF647 and then Ab) were aggregated as indicated by the purple color, and the presence of two UV-Vis bands (528 and 575 nm). These data indicate that if the dye is added in Step 1, it must first be reacted with the AET in order to avoid particle instability.

The stable nanoparticles were then filtered and used in an immunoassay with PPV (6.4×10^6 $TCID_{50}$/mL). Each SERS spectra were evaluated to determine if bands characteristic of the reporter were visible. As expected, the DSNB standard *ERL*s yielded bands attributable to the reporter molecule, as will be discussed later.[29] In addition, the particles modified by Methods 4 and 6 have bands representative of AF647, whereas those derived by Methods 2 and 3 had no visible bands. These results indicate that: (1) labeling the antibody prior to addition to nanoparticles does not yield a SERS signal; and (2) when AF647 was not coupled to AET, no SERS spectrum was observed. These results can be attributed to the SERS scatterer being too removed from the nanoparticle for the former and the dye molecule not adhering to the nanoparticle in the latter. Furthermore, the *ERL*s formed by Method 4 (Ab then AF647-AET) had larger SERS signals and were more stable over time than those formed by Method 6 (AF647-AET then Ab)

In conclusion, stable *ERL*s can be formed when antibody is first adsorbed to the colloidal gold surface through ionic and hydrophobic interactions and then thiol terminated dye (AF647-AET) is chemisorbed to the gold nanoparticle surface. As a result, the following experiments used particles modified by Method 4.

3.2. Stabilization of ERLs Coated with Positively Charged Dyes

As previously demonstrated,[37] gold nanoparticles formed by citrate reduction have a net negative surface charge which plays a key role in colloidal stability. Upon applying Method 4 and using the positively charged M689-AET molecule, the nanoparticles aggregated. This observation can be attributed to the adsorbed cations disrupting the stability of the suspension as the repulsive, negative interparticle interactions were reduced. This description can be theoretically predicted by the Derjaguin-Landau-Vervey-Overbeek (DLVO) theory.[38,39] This aggregation has previously been evaluated with positively charged indolenine cyanine dyes.[40] Specifically, when these cationic molecules reacted with negatively charged gold nanoparticles, electrostatic dye-particle interactions occurred and J-aggregated bridged assemblies formed due to π-π interactions. These interactions may also be occurring with M689-AET. In order to possibly counteract the positive charge of the dye and decrease aggregation, the nanoparticle solutions were made more basic with buffers.

As such, nanoparticles were conjugated with anti-mouse IgG and buffered to the desired pH (7-7.5 with 200 μL of 10 mM PBS, 8-9 with 20 μL of 50 mM borate buffer, 9.5-10 with 200 μL of 10 mM borate buffer, and 10.5-11 with 20 μL of 50 mM carbonate buffer). Following Method 2, M689-AET was then reacted for 5 h. Finally, UV-Vis spectra of the solutions were obtained, and the results are shown in Figure 3. As previously demonstrated,[29,41,42] a single band at ~535 nm is indicative of a colloidal solution composed of isolated 60-nm gold particles, while band broadening or splitting as well as shifting to longer wavelengths is diagnostic of aggregate formation. At pH 7.5, the band is split. Upon buffering at pH 10.5, a single feature at ~535 nm is obtained. At pH 9, an intermediate spectrum is obtained with features indicative of particle aggregation. These

results, as well as the spectra from the other pH values tested, indicated that a stable nanoparticle suspension is achieved with positive dyes when the pH≥9.5. Because high pH values can denature antibodies and lower their binding affinity[43] as well as decrease the number of IgG molecules adsorbed to the gold surface,[44] the lowest pH that allowed for stable nanoparticles (pH 9.5) was chosen for the remainding studies involving M689-AET *ERL*s.

The *ERL*s were also characterized by zeta potential measurements. The zeta potential, which is the potential at the slipping plane of a particle, can be used to determine the charge of the particles as well as the stability of the colloidal suspension. Upon taking measurements with each type of *ERL*, the data in Figure 4 were obtained. These data indicate that the *ERL*s are all negatively charged and at a comparable magnitude. From this, we speculate that the *ERL*s charge is dominated by the antibody coated nanoparticles and are stable as the pH is above the antibody pI (6.6-7.2, [45]).

3.3. Mouse-IgG Immunoassay Spectra and Calibration Curves

Immunoassays were first performed with the nonresonant DSNB as a label to obtain a comparative performance metric. The results of the heterogeneous, two-site immunoassay for mouse IgG concentrations ranging from 0.01 to 1000 ng/mL are shown in Figure 5. As evident, the representative SERS spectra in Figure 5a, which were obtained at 1-s integration times, have characteristics of the DSNB-derived monolayer. The strongest band in each spectrum (1336 cm^{-1}) is attributed to a symmetric nitro stretch ($\nu_s(NO_2)$), while the less intense feature (1588 cm^{-1}) is associated with an aromatic ring mode. In addition, other features are indicative of the DSNB-modified *ERL*s including a nitro scissoring vibration at

851 cm^{-1} and a succinimidyl N-C-O stretch overlapping with an aromatic ring mode at ~1075 cm^{-1}.[14] Moreover, as the amount of antigen in solution increases, the intensity of all spectral features also increase, demonstrating a corresponding increase in the number of *ERL*s bound to the surface. By plotting the intensity of $\nu_s(NO_2)$ versus the log of the antigen concentration, the calibration curve in Figure 5b is obtained. As expected, this curve has the characteristic shape and approximately three orders of linear magnitude associated with equilibrium models of a two-site assay.[43]

After performing the DSNB *ERL* immunoassay, the dye-AET *ERL*s were tested using the same assay platform. The SERS spectra for each reporter molecule, taken at 0.1 ng/mL mouse IgG and baseline corrected, are shown in Figure 6a. Each reporter has a distinct Raman spectral signature, but Cy5 and AF647 have comparable features which can be attributed to the similarity of these fluorophores. While the spectra taken of the dye molecule *ERL*s used an integration time of 0.2 s, spectral features for the nonresonant DSNB *ERL* are comparatively weaker even though collected at an exposure time of 1-s, indicating that indeed the resonant labels are stronger SERS scatters.

Upon plotting the intensity for the bands labeled by stars in Figure 6a versus the log of the antigen solution concentration, the calibrations curves in Figure 6b are obtained. These bands are chosen because of their high SERS intensity and lack of overlapping bands. In this format, SERS spectra were normalized to 1-s integration times, and it is clear that the signals for the dye molecules far surpass those of the nonresonant DSNB at each antigen concentration. In addition, the dye molecule assays qualitatively follow the characteristic concentration-dependent signal with larger SERS intensities from higher mouse IgG concentrations.

3.4. Enhancement of Resonant Raman Labels Over Nonresonant DSNB

In order to more fully investigate the performance of the resonant molecules, enhancement factors and limits of detection were determined. To evaluate the enhancement factor, the calibration curves for the dye molecules versus DSNB were compared. Through plotting intensity versus the antigen solution concentration, a calibration curve can be obtained and a linear trend established. An example of this is shown in Figure 7a for DSNB and Figure 7b for Cy5. By comparing the slopes of the best-fit lines between 0.01 ng/mL and 0.1 ng/mL, relative enhancement factors can be determined. In this example, the slope of the Cy5-AET coated *ERL* is just over 300 times greater than that for the DSNB modified *ERL*.

The limit of detection (LOD) is the lowest antigen concentration expected to produce a SERS signal distinct from the blank. The dashed line in each curve represents this signal and is calculated from the signal of blank plus three times the standard deviation in the blank signal. From this, the LOD can be determined from the intersection of the best-fit line with the dashed line in each calibration curve. Numerically, the intersection is at 46 pg/mL for DSNB and 24 pg/mL for Cy5, which corresponds to approximately 200 fM of mouse IgG.

The results of this analysis for all the *ERL*s are summarized in Table 3. Each resonant reporter yields an enhanced SERS signal that is approximately two orders of magnitude over that of DSNB. The limit of detection, however, is not significantly improved for the resonant dyes. At a first pass, one can speculate that if a signal is two orders of magnitude higher, then the LOD of would be one hundred times improved if the blank signal for each system was of the same magnitude and standard deviation. However, the improvement in signal strength also applies to the *ERL*s that are present in the blank from nonspecific adsorption. Thus,

while the Cy5-AET *ERL* has 300 times the signal of the DSNB *ERL*, the blank is also 300 times stronger.

From this, it can be concluded that while resonant molecules do yield much stronger signals, the LODs are dominated not by reporter signal strength but by nonspecific adsorption. In order to take advantage of the enhanced signals resonant labels offer, nonspecific adsorption must be minimized to the point where the blank signal is truly blank and dominated only by instrument noise and sample variability.

CONCLUSIONS

Increased signal intensities during detection hold promise for creating more sensitive assays. In SERS-readout assays, one technique to improve signals is to achieve resonant conditions with the Raman active molecule. In our system, *ERL*s can be used to integrate dye molecules that have an adsorption band in tune with the laser wavelength (~633 nm). By adapting current methods for forming *ERL*s, specifically conjugation order and solution pH, stable and nonaggregated SERS labels can be obtained for both positive and negatively charged resonant dye molecules. The resonant labeled *ERL*s behaved similarly to the standard DSNB reporter as indicated by the calibration curves. In addition, enhancement factors for the resonant molecules were determined to be on the order of two magnitudes over the nonresonant DSNB, but limits of detection did not show the same improvements due to nonspecific adsorption. Studies to improve upon current protocols with respect to nonspecific binding are currently underway in order fully realize the potential of the resonant molecule labeled *ERL*s.

ACKNOWLEDGEMENTS

We acknowledge Julia Ridpath and Ann Vorwald for providing PPV and anti-PPV. This work was funded by a grant from CEROS/DARPA, and by support from the Institute for Combinatorial Discovery of Iowa State University. The Ames Laboratory is operated for the United States Department of Energy through Iowa State University under contract W-7405-eng-82.

REFERENCES

[1] O. Lazcka, F.J. Del Campo, F.X. Munoz, Biosens. Bioelectron. 22 (2007) 1205.
[2] M. Fleischmann, P.J. Hendra, A.J. McQuillan, Chem. Phys. Lett. 26 (1974) 163.
[3] D.L. Jeanmaire, R.P. Van Duyne, J. Electroanal. Interfacial Electrochem. 84 (1977) 1.
[4] M.G. Albrecht, J.A. Creighton, J. Am. Chem. Soc. 99 (1977) 5215.
[5] M. Moskovits, Rev. Mod. Phys. 57 (1985) 783.
[6] A. Otto, J. Timper, J. Billmann, G. Kovacs, I. Pockrand, Surf. Sci. 92 (1980) L55.
[7] T. Vo-Dinh, Trends Anal. Chem. 17 (1998) 557.
[8] R.L. Garrell, Anal. Chem. 61 (1989) 401A.
[9] K. Kneipp, H. Kneipp, I. Itzkan, R.R. Dasari, M.S. Feld, J. Phys.: Condens. Matter 14 (2002) R597.
[10] G.C. Schatz, Acc. Chem. Res. 17 (1984) 370.
[11] K. Kneipp, H. Kneipp, I. Itzkan, R.R. Dasari, M.S. Feld, Chem. Rev. 99 (1999) 2957.
[12] D.A. Long, The Raman Effect: A Unified Treatment of the Theory of Raman Scattering by Molecules, John Wiley and Sons, Ltd., West Sussex, England, 2002.
[13] J. Ni, R.J. Lipert, G.B. Dawson, M.D. Porter, Anal. Chem. 71 (1999) 4903.
[14] D.S. Grubisha, R.J. Lipert, H.Y. Park, J. Driskell, M.D. Porter, Anal. Chem. 75 (2003) 5936.
[15] J.D. Driskell, R.J. Lipert, M.D. Porter, J. Phys. Chem. B 110 (2006) 17444.
[16] D.O. Ansari, D.A. Stuart, S. Nie, D.V. Nicolau, J. Enderlein, R.C. Leif, D.L. Farkas, R. Raghavachari (Editors), SPIE - Imaging, Manipulation, and Anaylsis of Biomolefules and Cells: Fundamentals and Applications III, Bellingham, WA, 2005, p. 82.
[17] Y.C. Cao, R. Jin, C.A. Mirkin, Science 297 (2002) 1536.
[18] Y.C. Cao, R. Jin, J.-M. Nam, C.S. Thaxton, C.A. Mirkin, J. Am. Chem. Soc. 125 (2003) 14676.
[19] M. Culha, D. Stokes, R. Allain Leonardo, T. Vo-Dinh, Anal. Chem. 75 (2003) 6196.
[20] W.E. Doering, S. Nie, Anal. Chem. 75 (2003) 6171.
[21] K. Faulds, W.E. Smith, D. Graham, Anal. Chem. 76 (2004) 412.
[22] D. Graham, K. Faulds, W.E. Smith, Chem. Commun. (2006) 4363.

[23] P.B. Monaghan, K.M. McCarney, A. Ricketts, R.E. Littleford, F. Docherty, W.E. Smith, D. Graham, J.M. Cooper, Analytical Chemistry (Washington, DC, United States) 79 (2007) 2844.
[24] S.P. Mulvaney, M.D. Musick, C.D. Keating, M.J. Natan, Langmuir 19 (2003) 4784.
[25] J.-M. Nam, C.S. Thaxton, C.A. Mirkin, Science 301 (2003) 1884.
[26] J.D. Ingle, S.R. Crouch, Spectrochemical Analysis, Prentice Hall, Upper Saddle River, New Jersey, 1988.
[27] B.J. Kennedy, S. Spaeth, M. Dickey, K.T. Carron, J. Phys. Chem. B 103 (1999) 3640.
[28] J.D. Driskell, J.M. Uhlenkamp, R.J. Lipert, M.D. Porter, manuscript in preparation (2006).
[29] J.D. Driskell, K.M. Kwarta, R.J. Lipert, M.D. Porter, J.D. Neill, J.F. Ridpath, Anal. Chem. 77 (2005) 6147.
[30] K.M. Kwarta, J.D. Driskell, M.D. Porter, J.D. Neill, J.F. Ridpath, in preparation (2007).
[31] B.J. Yakes, R.J. Lipert, J.P. Bannantine, M.D. Porter, in preparation.
[32] B.J. Yakes, R.J. Lipert, J.P. Bannantine, M.D. Porter, in preparation.
[33] H.-Y. Park. 2005. Chip-scale Bioassays Based on Surface-enhanced Raman Scattering: Fundamentals and Applications. Anal. Chem., Iowa State University, Ames.
[34] G.T. Hermanson, Bioconjugate Techniques, Academic Press, San Diego, California, 1996.
[35] Malvern, ZetaSizer Nano Series User Manual, Worcestershire, UK, 2003.
[36] A.M. Michaels, M. Nirmal, L.E. Brus, J. Am. Chem. Soc. 121 (1999) 9932.
[37] D.A. Weitz, M.Y. Lin, C.J. Sandroff, Surf. Sci. 158 (1985) 147.
[38] B. Deryagin, L. Landau, Acta Physicochimica URSS 14 (1941) 633.
[39] E.J.W. Verwey, J.T.G. Overbeek, Theory of the Stability of Lyophobic Colloids, 1948.
[40] I.I.S. Lim, F. Goroleski, D. Mott, N. Kariuki, W. Ip, J. Luo, C.-J. Zhong, J. Phys. Chem. B 110 (2006) 6673.
[41] J.A. Creighton, in R.K. Chang, T.E. Furtak (Editors), Surface Enhanced Raman Scattering, Plenum Press New York, 1982, p. 315.
[42] T.J. Norman, Jr., C. Grant, D. Magana, R.W. Anderson, J. Zhang, D. Cao, F. Bridges, J. Liu, T. van Buuren, Proc. SPIE 4807 (2002) 51.
[43] E.P. Diamandis, T.K. Christopoulos (E.P. Diamandis, T.K. Christopoulos(E.P. Diamandis, T.K. Christopouloss), Immunoassay, Academic Press, San Diego, 1996.
[44] W.D. Geoghegan, J. Histochem. Cytochem. 36 (1988) 401.
[45] Pierce Technical Support, 2007.

FIGURES

Fig. 1. Formation of *ERL*s and heterogeneous immunoassay procedure.

Table 1. Reporter names, acronyms, spectral characteristics, and molecular charges.

Fig. 2. Reactive endgroup formation.

Table 2. *ERL* labeling strategies.

Fig. 3. *ERL* stabilization: UV-Vis spectra of *ERL*s, containing α-mouse IgG and M689-AET, buffered to varying pH values.

Fig. 4. Zeta potential measurements of *ERL*s showing similar charges and stability for each nanoparticle/dye-AET combination.

Fig. 5. Mouse IgG immunoassay with DSNB reporter: (a) spectra for individual antigen concentrations (1-s integration, offset for visual clarity) and (b) corresponding calibration curve with each data point an average of five measurements per slide.

Fig. 6. Mouse IgG immunoassay for all reporters: (a) representative spectra for each reporter at an antigen concentration of 0.1 ng/mL, integration times as listed (offset and baseline corrected for visual clarity) and (b) corresponding calibration curves for low concentration antigen solutions. All dye molecules were in the dye-AET reacted form.

Fig. 7. Calibration curve for mouse IgG immunoassay, lower concentration ranges for (a) DSNB and (b) Cy5-AET form. Average of five measurements per slide and dashed lines indicating the level of detection based on blank + 3σ of blank.

Table 3. Enhancement (normalized to DSNB) and limit of detection (LOD, pg/mL) as determined from the intersection of the slope of the best-fit line (between 0.01 and 0.1 ng/mL) and the (blank+3σ) level for each reporter tested. All dye molecules were in the dye-AET reacted form.

Fig. 1.

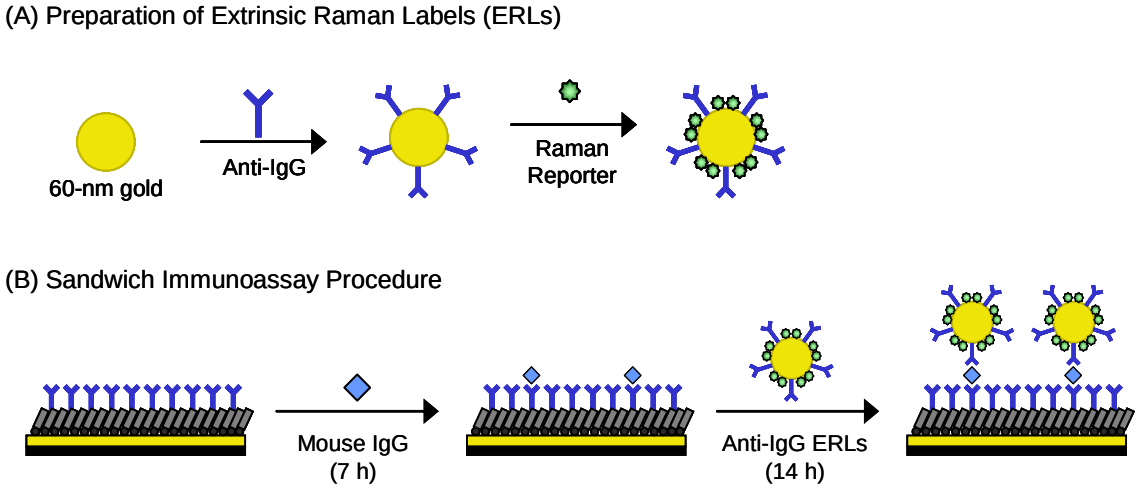

Table 1.

Molecule Name	Abbrev.	Ex Max (nm)	Em Max (nm)	Charge
Dithiobis (succinimidyl nitrobenzoate)	DSNB	320	400	Neutral
Cy5 monofunctional, succinimidyl ester (SE)	Cy5	646	664	Negative
Alexa Fluor 647 SE	AF647	650	665	[1]
Malachite green isothiocyanate	M689	629	None	Positive
5-(and 6-) carboxynaphthofluorescein, SE	CNF	602	672	Negative[2]

[1] No structure available for Alexa Fluor

[2] CNF has a pK_a of 7.6

Fig. 2.

(A) Succinimidyl Ester Reaction

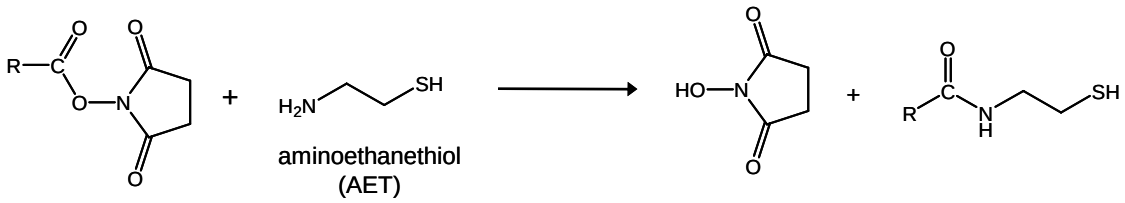

(B) Isothiocyanate Reaction

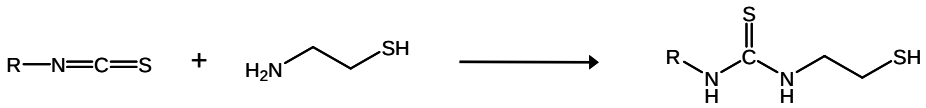

Table 2.

Method	Step 1	Step 2
1	React nps[1] with DSNB	Add Ab
2	React Ab with AF647	Add 10 µL of Step 1 to nps
3	Adsorb Ab to nps	Add AF647
4	Adsorb Ab to nps	Add AF647-AET
5	React nps with AF647	Add Ab
6	React nps with AF647-AET	Add Ab

[1] nanoparticle solutions (nps)

Fig. 3.

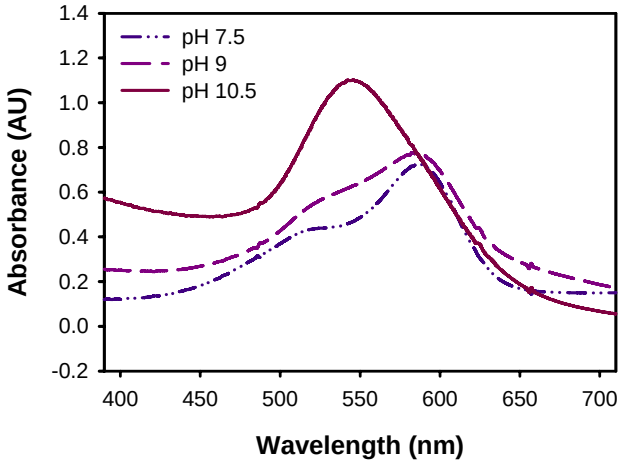

Fig. 4.

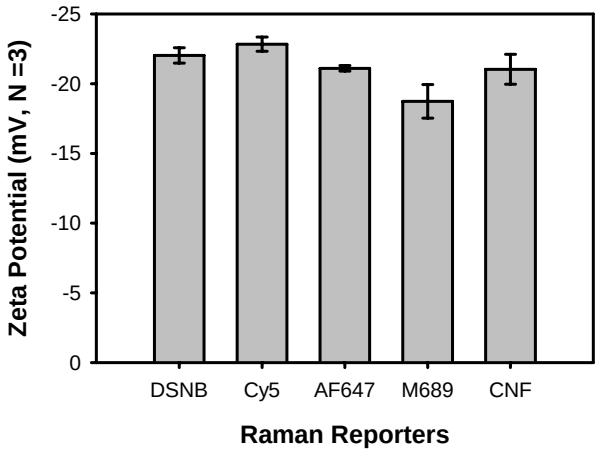

Fig. 5.

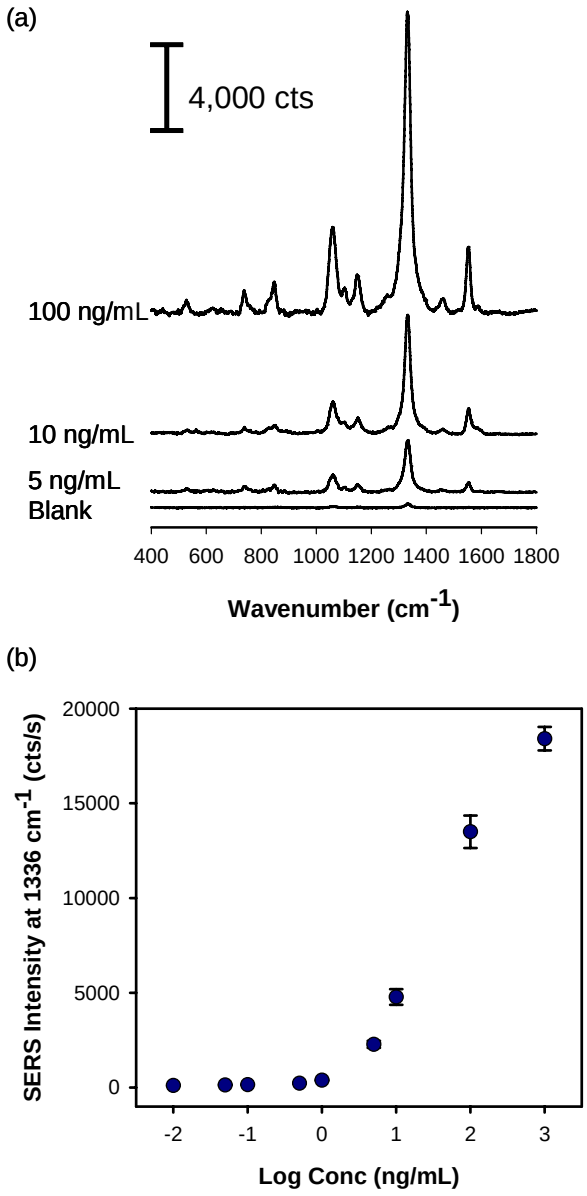

Fig. 6.

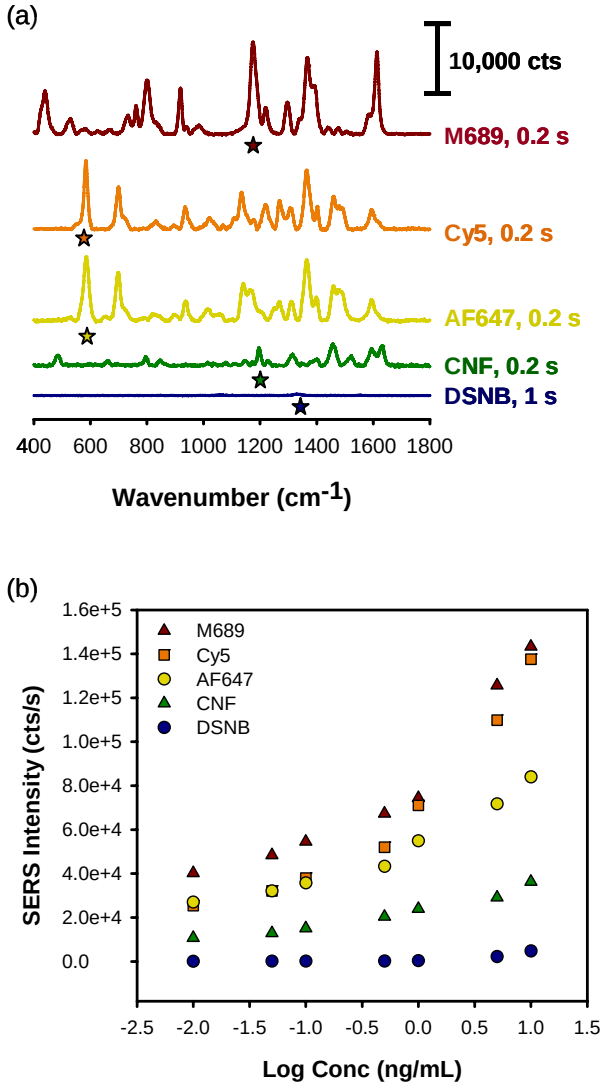

Fig. 7.

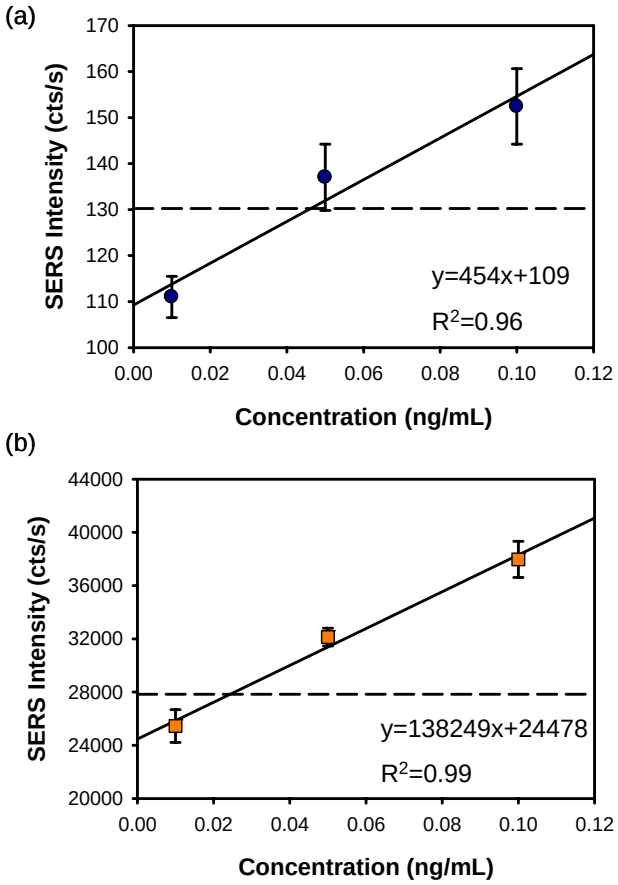

Table 3.

Reporter	Enhancement	LOD (pg/mL)
DSNB	1	46
M689	346	35
Cy5	305	24
AF647	212	24
CNF	107	27

CHAPTER 5: Electrochemically modulated liquid chromatographic separation of triazines and the effect of pH on their retention

Betsy Jean Yakes[a], David W. Keller[b], Marc D. Porter[a,*]

[a] Departments of Chemistry and Chemical and Biological Engineering, Ames Laboratory – USDOE, and Institute for Combinatorial Discovery, Iowa State University, Ames, IA 50011

[b] Current Address: AMRI, 26 Corporate Circle, PO Box 15098, Albany, NY 12212-5098

* Corresponding Author. Current Address: Center for Combinatorial Discovery, Biodesign Institute, Arizona State University, Tempe, AZ 85287-6401. Phone: (480-727-8598). Fax: (480-727-9499). E-mail: Marc.Porter@asu.edu

A paper to be submitted to the *Journal of Chromatography A*

ABSTRACT

Electrochemically modulated liquid chromatography (EMLC) manipulates analyte retention by changing the potential applied (E_{app}) to a conductive stationary phase. This paper applies EMLC to the separation of triazines, a commonly used, but environmentally hazardous, class of herbicides. Experiments herein examine the influence of mobile phase pH on retention, in combination with tuning E_{app}, to take advantage of the ionizablity of the triazine ring nitrogen. Results discussed include: (1) the merits of using EMLC to separate this class of compounds; (2) the retention mechanism for triazines of dissimilar acid strengths; and (3) the rapid separation of a seven-component triazine mixture.

Keywords: electrochemically modulated liquid chromatography; potential control; herbicides; triazines; pH

INTRODUCTION

Electrochemically modulated liquid chromatography (EMLC) combines liquid chromatography and electrochemistry as a unique approach to manipulate retention. In EMLC, a three-electrode electrochemical cell is reconfigured to simultaneously function as an HPLC column (Figure 1). In most cases, EMLC columns are packed with porous graphitic carbon (PGC) which serves both as a conductive stationary phase and as a working electrode. As a result, retention can be fine tuned by changes in the potential applied (E_{app}) to the column, adding another dimension to LC separations.

Several laboratories,[1-11] including our own,[12-27] have investigated a wide range of separations with EMLC. To date, EMLC has been applied to the separation of aromatic sulfonates,[13] monosubstituted benzenes,[17] pyridines/anilines,[20] corticosteroids,[14] benzodiazepines,[15,18] optical isomers,[19] short-chain carboxylic acids,[3] metal-ion complexes,[10] inorganic anions,[26] and amino acids.[2,23] This paper extends this list to include herbicides, while also exploring the integration of EMLC and pH-modified mobile phases.

One of the driving forces behind agrochemical research is the need for effective, low-cost weed control using compounds which are environmentally benign. The *s*-triazines are a class of compounds that have been used for over forty years to control broadleaf and grassy weeds through disruption of photosynthesis pathways.[28] These molecules, as shown in Table 1, are based on a six-membered ring with nitrogen and carbon atoms linked by alternating single and double bonds. *s*-Triazines can also be grouped into subclasses based on their substituents: (1) atrazine, propazine and simazine are chloro-*s*-triazines; (2) prometon is a methoxy-*s*-triazine; and (3) ametryn, prometryn and terbutryn are methylthio-*s*-traizines.

The chlorinated triazines and their metabolites are, unfortunately, associated with possible cancer risks in humans and tumor incidence in animals,[29] and the methylthio-*s*-triazines are potentially toxic to aquatic organisms. As a consequence, the United States Environmental Protection Agency instituted a Special Review in 1994 that called for more research into the long-term environmental effects and metabolite degradation of these compounds.[30]

While the gas chromatographic analysis of triazines is commonplace,[31] the polarity and low volatility of these compounds often dictate the use of derivatization steps prior to separation.[32] With recent advances in packing materials, liquid chromatography can be readily applied to separate herbicides without derivatization.[33,34] Drawing on this capability, liquid chromatography studies on triazine herbicides and their metabolites[35-43] have focused on realizing rapid and efficient separations. In addition to the LC work, research on optimizing extraction of triazines from soil [37,38,40,41] and utilizing mass spectrometry to better evaluate degradation products is enabling better herbicide monitoring.[39] Despite the advantages of LC, the separations can still be challenged by low resolution, owing to the strong interactions of these polar compounds with many stationary phases. Moreover, the structural similarity of the triazines and their metabolites can often lead to overlapping of elution bands.

It has recently been shown that a highly effective separation of *s*-triazine herbicides in capillary zone electrophoresis can be achieved by optimizing the pH of the running buffer.[44] This approach takes advantage of the basicity of the nitrogens on the *s*-triazine aromatic ring, which can be protonated to impart a net positive charge.[45] Table 1, which lists the compounds that will be examined herein, summarizes this chemistry. This paper

investigates the impact of varying the pH of the mobile phase, as well as E_{app}, on the separation of a mixture of *s*-triazines. These separations will employ a PGC stationary phase, which is stable between pH 1 and 14 and in a wide range of solvents,[27,46,47] as the column packing. The findings will also be examined with respect to the role of the mobile phase pH on the retention mechanism.

EXPERIMENTAL

2.1. Chemicals and Reagents

The seven triazines, their abbreviations, and numeric labels are given in Table 1; all were purchased as the Triazine Neat Kit (49092) from Supelco (Bellefonte, PA, USA). The compounds were dissolved in methanol (HPLC-grade, Fisher, Pittsburgh, PA, USA) to a final concentration of 25 μM. Acetonitrile (HPLC-grade, Fisher) and deionized water (MilliPore Milli-Q system, 18Ω, Billerica, MA, USA), along with lithium perchlorate (Sigma-Aldrich, St. Louis, MO, USA), were used for all mobile phase preparations. In addition, 85% *o*-phosphoric acid (certified ACS, Fisher), glacial acetic acid (reagent grade, Fisher), sodium tetraborate decahydrate (ACS reagent, Sigma-Aldrich), and lithium hydroxide (reagent grade, Fisher) were employed to modify the pH of the mobile phase. Solutions of pH 4.00 (potassium hydrogen phthalate), 7.00 (potassium phosphate monobasic/sodium hydroxide), and 10.00 (potassium carbonate/potassium tetraborate/potassium hydroxide/disodium EDTA dihydrate) were acquired from Fisher.

2.2. Mobile Phase Preparation

A series of preliminary experiments were performed to determine the most effective isocratic mobile phase composition for these separations. Separations were carried out with 60%, 70%, 80% or 90% acetonitrile in water as mobile phases. These results indicated that a 70% acetonitrile and 30% water mixture was a reasonable starting point based on tradeoffs between the duration and efficiency of separation. Thus, the standard mobile phase was prepared by dissolving lithium perchlorate (for solution conductivity) in 300 mL deionized water/700 mL acetonitrile to yield a 0.1 M solution. Prior to use, all mobile phases were: (1) passed through a 0.5-μm glass fiber filter (GE-Osmonics, Minnetonka, MN, USA) to remove any particulates; and (2) degassed for 30 min with high purity helium.

Three 100 mM buffer solutions were used [48-51]; phosphate buffer for pH 2, acetate buffer for pH 3 and 4, and borate buffer for pH 9. These buffers were chosen due to their solubility in the mixed mobile phase and optical transparency above 220 nm.[52] First, 300 mL of buffer in water was prepared, and small adjustments in pH were made by addition of 1 M (aq) lithium hydroxide. This step was followed by addition of lithium perchlorate (10.6 g) and 700 mL of acetonitrile in order to match the standard mobile phase.

Measurements of pH were made with a standard glass electrode and meter (Orion model 520 A pH meter, Boston, MA, USA) and calibrated using pH 4.00, 7.00, and 10.00 standards. After calibration, the pH of the buffer in the initial 300 mL of water (${}^{w}_{w}pH$, purely aqueous mobile phase and water standards), as well as after organic modifier (acetonitrile) and lithium perchlorate (${}^{s}_{w}pH$, mobile-phase solvent relative to water standards), was

measured.[53] All pH values reported herein are as ${}^{w}_{w}pH$, which is the most commonly used scale in the reverse phase HPLC literature.[48]

2.3. EMLC Column

The design of the EMLC column is shown in Figure 1, and the column construction has been detailed elsewhere.[16] In brief, 5-µm porous graphitic carbon (PGC, Thermo Hypersil, Runcorn, UK) is packed into a porous stainless steel (Mott Corp., Farmington, CT, USA) column (3.2 mm ID x 110 mm length) that has been lined with a Nafion (Perma Pure Inc., Toms River, NJ, USA) cation exchange membrane. The PGC stationary phase serves the working electrode (WE) while the Nafion tubing functions as the salt bridge to the external reservoir. This reservoir contains a silver/silver chloride (saturated sodium chloride) reference electrode, and all values of E_{app} will be reported with respect to this reference. The Nafion membrane also electrically isolates the PGC and the porous stainless steel tube, which functions as a high surface area auxiliary electrode (AE). The connection to the WE is made through a stainless steel frit. The WE is, however, electronically isolated from the AE by a Kel-F ring that is inserted in a PEEK union and a PAT frit at the top of the column.

2.4. Instrumentation

The column was connected through standard, stainless steel endfittings to an Agilent Technologies (Palo Alto, CA, USA) model 1050 HPLC system, equipped with a solvent cabinet, autosampler, quaternary pumping system, and UV-Vis diode array detector. The samples were injected using a 5.0-µL loop, and elution profiles were monitored at 220, 230,

and 254 nm. The potential applied to the stationary phase was controlled with a Model 174A Polarographic Analyzer (Princeton Applied Research, Oak Ridge, TN, USA).

2.5. Mode of Operation

The mobile phases were passed through the column at 0.4 mL/min until a constant baseline was reached after each change in mobile phase or E_{app}. Duplicate injections were performed to assess the reproducibility of the separation. Individual analyte injections were used to determine the identity and elution times of each chromatographic band. Void time was determined by a methanol injection at each potential/mobile phase composition and was used for the calculation of the capacity factor (*k'*). To compensate for band tailing, retention times were determined from the first statistical moment analysis. In addition, resolution (R_s), as defined by the half-width peak method, with a value of 1.5 or greater is termed baseline resolution[54] and values between 1.0 and 1.5 are referred to as "effective resolution."[26]

RESULTS AND DISCUSSION

3.1. Studies with pH Controlled Mobile Phases

As shown in Table 1, triazines can be protonated at the aromatic ring nitrogens. The acid strength of these compounds is strongly influenced by the substituents on the triazine ring: chlorotriazines have a pK_a of ~2 and methoxy- and methylthiotriazines have a pK_a of ~4.[44,45,55,56] The differences in pK_a values can be attributed to the high electronegativity of the chlorine group and resonance effects for the methoxy- and methylthiotriazines.[56] Since retention at PGC is manipulated by EMLC through a combination of donor-acceptor, dispersive, and solvophobic interactions,[13] this section of the paper examines the effects of

varying E_{app} and changing the pH of the mobile phase on the separation of a seven-component mixture.

3.1.1. Mobile Phase pH of 2

The results for the separation of the mixture with the pH 2 mobile phase (phosphate buffer, ${}^{w}_{w}pH$ =1.8) are presented in Figure 2. At the most positive value of E_{app} (+400 mV), PZ, PY, and TY have overlapping elution profiles; AZ and AY have a similar problem. When moving to +200 mV, bands for all seven analytes become distinguishable, but the total time for separation is only marginally effected. By applying more negative potentials, the elution time of the methoxy- (PO) and methylthiotriazines (PY, TY and AY) become longer, whereas those of the chlorinated triazines (PZ, AZ, and SZ) are only marginally changed. Interestingly, the difference in the dependence of retention on E_{app} causes a change in the elution order of the components in the mixture.

The results from this experiment are summarized in the top set of graphs of Figure 3 in which the natural log of the capacity factor (ln k') is plotted versus E_{app}. Figure 3 also documents the sensitivity of retention (i.e., $\Delta \ln k'/\Delta E_{app}$) for each compound. Qualitatively, the triazines with a pK_a of ~4 should be protonated at pH 2, with AY, TY, PY, and PO then being positively charged. The elution times for these compounds should therefore increase as E_{app} becomes more negative, reflecting the importance of electrostatic interactions on retention. This trend is observed in Figure 3. This behavior, however, is in contrast to that of the chlorotriazines (pK_a ~2) which exist as a mixture with nearly equal proportions of their unprotonated and protonated conjugates. In this case, the retention of SZ, AZ, and PZ has smaller potential dependence.

3.1.2. Mobile Phase pH of 9

Next, the potential dependent retention of the triazines was evaluated at a mobile phase pH of 9 (borate buffer, ${}^{w}_{w}pH$ =9.2). At this pH, all the components of the mixture should be exhaustively deprontated and thus present as neutrals. The retention of the neutral molecules should then be governed mainly by interactions between the π-systems of the *s*-triazine aromatic rings and the graphitic carbon stationary phase. Interestingly, the retention dependence on E_{app} at pH 9 (bottom graph in Figure 3) is in stark contrast to that at pH 2. All seven compounds now undergo an increase in retention as E_{app} moves to more positive values.

There is another interesting point to draw from these data – the elution order of the analytes. As previously hypothesized,[13] neutral aromatic compounds interact with the carbonaceous stationary phase via an orientation that maximizes the π-system interactions. It then follows that triazine retention would be affected by any steric effects associated with bulky substituents. The plots at pH 9 are qualitatively consistent with this expectation in that shorter retention times are observed for the triazines with more bulky alkyl groups. In other words, PO, PZ, and PY elute first (R_1=R_2=isopropyl), followed by TY (R_1=ethyl, R_2=tert-butyl), then AZ and AY (R_1=ethyl, R_2=isopropyl), and finally SZ (R_1=R_2=ethyl).

3.1.3. Mobile Phase pH of 4

To further investigate the dependence of the EMLC separation on the acid-base chemistry of the triazines, the mobile phase was changed to pH 4 (acetate buffer, ${}^{w}_{w}pH$ = 3.9). The results from this intermediate pH value are summarized by the middle set of plots

in Figure 3. In this scenario, the methylthiotriazines (AY, TY, and PY) should exist in a nearly equal distribution of their protonated and unprotonated forms. As found at pH 2, there is very little change in retention upon varying E_{app} when the triazine exists in close to an equal proportion of its charged and neutral forms. PO, a methoxytriazine with pK_a of 4.2, has a small, negatively valued sensitivity, which is qualitatively consistent with a slight excess of cations as opposed to the neutral form. For the chlorotriazines (SZ, AZ, PZ), which at pH 4 should be present mainly in their unprotonated form, the sensitivity is slightly positive, with retention times tracking the π-interactions discussed in section 3.1.2.

The separations at this transitional pH, shown in Figure 4, also illustrate an unusual dependence on E_{app}. As is evident, the methylthiotriazines (PY, TY, AY) remain at approximately the same elution time regardless of E_{app}. However, as E_{app} becomes more negative, the retention time of the chlorotriazines (PZ, AZ, SZ) decrease and that of the methoxytriazine (PO) increases. This "pulling apart" of the chromatogram leads to an effective resolution of the seven components at 0 mV. This phenomenon occurs because each analyte, as dictated by their equilibrium composition, respond differently to changes in E_{app}. That is to say, the retention of PO will be manipulated mainly by electrostatics, the neutral compounds (PZ, AZ, SZ) will be governed by π-system interactions, and the equilibrium mixtures (PY, TY, AY) will be retained by the opposing competition of both types of interactions. This retention dependence is another of the unique features of EMLC as a separation technique, and we will look to take advantage of this effect in future work.

3.2. Effect of Acid-Base Equilibrium on k'

The acid-base equilibria of an analyte can affect *k'* in a predictable manner.[57] In general, the equilibrium constant, K_a, for the mobile phase (m, solution concentrations) reactions in Table 1 between a triazine (*Tr*) and its corresponding cation (TrH^+) can be expressed as

$$K_a = \frac{[Tr]_m [H^+]_m}{[TrH^+]_m} \quad (1)$$

For retention at the stationary phase (s, interfacial concentrations), the equilibrium between the active sites on the carbon surface $[C]_s$ and the two forms of the triazine can be written as:

$$K_{C-Tr} = \frac{[C-Tr]_s}{[Tr]_m [C]_s} \quad (2)$$

$$K_{C-TrH^+} = \frac{[C-TrH^+]_s}{[TrH^+]_m [C]_s} \quad (3)$$

where $[C\text{-}Tr]_s$ and $[C\text{-}TrH^+]_s$ signify the reversible association between the neutral and protonated forms of the triazines, respectively, and PGC. These theoretical considerations neglect any acid-base chemistry for PGC.[46] The overall capacity factor can then be determined by the distribution of the analyte between the stationary and the mobile phases:

$$k' = \phi \frac{[C-TrH^+]_s + [C-Tr]_s}{[TrH^+]_m + [Tr]_m} \quad (4)$$

where ϕ is the phase ratio for the stationary and mobile phase volumes. By solving equations 1-3 for $[TrH^+]$, [C-Tr], and $[C\text{-}TrH^+]$, respectively, and substituting these results into equation 4, the dependence of *k'* on the acid-base chemistry can be written as:

$$k' = \phi \frac{K_{C-TrH^+}[C]_s \frac{[H^+]_m}{K_a} + K_{C-Tr}[C]_s}{\frac{[H^+]_m}{K_a} + 1} \quad (5)$$

This expression can be further refined by defining the capacity factors for the unprotonated (k'_{Tr}) and protonated (k'_{TrH^+}) forms of the triazines through equations 2 and 3:

$$k'_{Tr} = \phi \frac{[Tr]_s}{[Tr]_m} = \phi [C]_s K_{C-Tr} \quad (6)$$

$$k'_{TrH^+} = \phi \frac{[TrH^+]_s}{[TrH^+]_m} = \phi [C]_s K_{C-TrH^+} \quad (7)$$

Upon substitution of equations 6 and 7 into equation 5, we arrive at:

$$k' = \frac{k'_{Tr} + k'_{TrH^+} \frac{[H^+]_m}{K_a}}{1 + \frac{[H^+]_m}{K_a}} = \frac{k'_{Tr} + k'_{TrH^+} \frac{[TrH^+]_m}{[Tr]_m}}{1 + \frac{[TrH^+]_m}{[Tr]_m}} \quad (8)$$

The two forms of equation 8 can therefore be used to qualitatively explain the dependencies observed in Figure 3. The results for AY, summarized in Figure 5, serve as an example. At pH 1.8, which is about two pH units less than the pK_a, AY is cationic and therefore migrates largely via the k'_{TrH^+} term in Equation 8. As a consequence, as more negative values of E_{app} are used, the cationic triazine is more strongly retained by PGC. Upon adjusting the pH to more basic values, the distribution of AY shifts towards its neutral form, and k'_{TrH^+} contributes less to the overall capacity factor. This dependence was verified by adjusting the mobile phase pH from 1.8 to 2.6 (both pH<pK_a), which decreases the importance of electrostatic interactions but increases the role of π-system interactions. Indeed, the separations at pH 2.6, as shown for AY in Figure 5, exhibited a less negative

slope. At pH 3.9, the two conditions essentially compete, and the overall capacity factor does not have a significant change with respect to the potential applied.

At pH 9.2, all the analytes are neutral, and equation 8 is controlled by k'_{Tr}. The positively sloped dependence of retention on E_{app} is primarily due to interactions from the π-system of the triazine ring and PGC. It is important to note, however, that the retention times, and thus ln *k'*, for the separations at different pH mobile phases cannot be directly compared because, as previous work has shown,[24,25] dissimilar electrolytes have varied elution strengths.

Another interesting result can be developed by plotting the sensitivities from the data in Figure 3 versus the mobile phase pH. Figure 6 shows such a plot for AY. This graph illustrates via Equation 8 that the pK_a of the molecule can be determined at the inflection point of curve to the sensitivities at each mobile phase pH. To obtain the inflection point, the best fit line for each retention regime (i.e., electrostatic domain at low pH and π-systems interactions at high pH) was determined and the intersection of these two lines was calculated. The intersection is at pH 3.4 pH indicates that the pK_a is slightly lower than the published value of 4.05.[44] This analysis was also applied to the other triazines, with PO, PY, and TY having respective pK_a values of 3.5, 3.3, and 3.3. These results are lower than the published pK_a values, which we attribute to the presence of acetonitrile, a lower dielectric solvent than water, in the mobile phase.[46] We note that assessments for PZ, AZ, and SZ were not possible because the mobile phase solutions were not acidic enough to determine a transition. This result indicates that EMLC can also be used to determine fundamental properties of molecules, an avenue of exploration which in currently underway.

3.3 Rapid Separation of Triazines

As a final set of experiments, the EMLC conditions were optimized and a rapid separation was performed under normal mobile phase conditions. As discussed previously, the retention of uncharged *s*-triazines is strongly affected by interactions between the π-systems of the triazines and those of PGC. Representative chromatograms from the separation of the triazine mixture are presented in Figure 7. The open-circuit potential (OCP) for this column and mobile phase is +150 mV. When operating slight more positive than the OCP (+200 mV), two sets of analytes have overlapping elution profiles, and the separation requires 14 min. These results elucidate the challenge posed by the separation of these polar, structurally similar compounds.

By taking advantage of the ability to manipulate the interactions between the column packing and analyte via changes in E_{app}, elution times can be decreased, and, interestingly, the resolution of the separation can be improved due to altered selectivity at different potentials. This effect is in contrast to conventional LC in that a decrease in retention usually results in a loss of resolution. This advantage of EMLC provides improvements in both time and resolution in the separation of this mixture to the extent that at -600 mV near baseline resolution (R_s between 1.3 and 4.7 for adjacent bands) of the seven components solution occurs in under eight minutes. Recent examples using reverse phase packing, however, require roughly twice the time, with little improvement over the resolution seen at -600 mV.[36,37,39]

CONCLUSIONS

The separation and retention characteristics of the triazine molecules were found to be strongly influenced by mobile phase pH. Under pH control, the separation of the triazine analytes showed marked changes in their sensitivity toward E_{app} that reflected the distribution of the conjugated acid-base forms of the compounds. We believe these results show that EMLC can not only be used to perform separations but also as a research tool to probe physical properties and processes. From the separation standpoint, near-baseline resolution of the seven triazines was realized in under eight minutes by taking advantage of the ability to manipulate E_{app}. Further work to extend the use of pH in EMLC to other systems is currently being performed. Research is also underway to more fully understand the mechanisms that govern the retention of the triazine compounds, with the ultimate goal being to form a set of global pH/EMLC retention rules.

ACKNOWLEDGEMENTS

The authors express their appreciation to Dr. Jennifer Granger for her insights and assistance in manuscript preparation. This work was supported by the US Department of Energy – Ames Laboratory. The Ames Laboratory is operated for the USDOE by Iowa State University under contract No. W-7405-eng-82.

REFERENCES

[1] J.L. Hern, J.H. Strohl, Anal. Chem. 50 (1978) 1954.
[2] F. Kocak, K. Vuorilehto, J. Schrader, D. Sell, J. Appl. Electrochem. 35 (2005) 1231.
[3] M.W. Knizia, K. Vuorilehto, J. Schrader, D. Sell, Electroanalysis 15 (2003) 49.
[4] T. Nagaoka, M. Fujimoto, Y. Uchida, K. Ogura, J. Electroanal. Chem. 336 (1992) 45.

[5] T. Nagaoka, K. Kakuno, M. Fujimoto, H. Nakao, J. Yano, K. Ogura, J. Electroanal. Chem. 368 (1994) 315.
[6] H. Ge, G.G. Wallace, J. Liq. Chromatogr. 13 (1990) 3245.
[7] H. Ge, P.R. Teasdale, G.G. Wallace, J. Chromatogr. 544 (1991) 305.
[8] T. Fujinaga, S. Kihara, CRC Crit. Rev. Anal. Chem. 6 (1977) 223.
[9] A.R. Ghatak-Roy, C.R. Martin, Anal. Chem. 58 (1986) 1574.
[10] M. Shibukawa, A. Unno, T. Miura, A. Nagoya, K. Oguma, Anal. Chem. 75 (2003) 2775.
[11] P. Nikitas, J. Electroanal. Chem. 484 (2000).
[12] R.S. Deinhammer, E.-Y. Ting, M.D. Porter, J. Electroanal. Chem. 362 (1993) 295.
[13] R.S. Deinhammer, E.-Y. Ting, M.D. Porter, Anal. Chem. 67 (1995) 237.
[14] E.-Y. Ting, M.D. Porter, Anal. Chem. 69 (1997) 675.
[15] E.-Y. Ting, M.D. Porter, J. Chromatogr. A 793 (1998) 204.
[16] E.-Y. Ting, M.D. Porter, Anal. Chem. 70 (1998) 94.
[17] E.-Y. Ting, M.D. Porter, J. Electroanal. Chem. 443 (1998) 180.
[18] S. Wang, M.D. Porter, J. Chromatogr. A 828 (1998) 157.
[19] M. Ho, S. Wang, M.D. Porter, Anal. Chem. 70 (1998) 4314.
[20] H. Takano, M.D. Porter, Proceedings - Electrochemical Society, 1999, p. 50.
[21] M.D. Porter, H. Takano, in I.D. Wilson, E.R. Adlard, M. Cooke, C.F. Poole (Editors), Encyclopedia of Separation Science, Academic Press, London, 2000, p. 636.
[22] J.A. Harnisch, M.D. Porter, Analyst 126 (2001) 1841.
[23] L. Deng. 1998. Thesis: Masters of Science. Applications of Electrochemically-Modulated Liquid Chromatography (EMLC): Separations of Aromatic Amino Acids and Polycyclic Aromatic Hydrocarbons. Chemistry, Iowa State University, Ames, IA.
[24] D.W. Keller, M.D. Porter, Anal. Chem. 77 (2005) 7399.
[25] D.W. Keller, L.M. Ponton, M.D. Porter, J. Chromatogr. A 1089 (2005) 72.
[26] L.M. Ponton, M.D. Porter, J. Chromatogr. A 1059 (2004) 103.
[27] L.M. Ponton, M.D. Porter, Anal. Chem. 76 (2004) 5823.
[28] L.P. Gianessi, in L.G. Ballantine, J.E. McFarland, D.S. Hackett (Editors), Triazine Herbicides: Risk Assessment; ACS Symposium Series 683, Oxford University Press, 1998, p. 1.
[29] J.W. Hauswirth, L.T. Wetzel, in L.G. Ballantine, J.E. McFarland, D.S. Hackett (Editors), Triazine Herbicides: Risk Assessment; ACS Symposium Series 683, Oxford University Press, 1998, p. 370.
[30] EPA, United States Environmental Protection Agency: Federal Register, November 23, 1994.
[31] S. Stipicevic, S. Fingler, L. Zupancic-Kralj, V. Drevenkar, J. Sep. Sci. 26 (2003) 1237.
[32] R.B. Geerdink, W.M. Niessen, U.A. Brinkman, J. Chromatogr. A 970 (2002) 65.
[33] E. Hogendoorn, P. van Zoonen, J. Chromatogr. A 892 (2000) 435.
[34] A.C. Hogenboom, W.M. Niessen, U.A. Brinkman, J. Sep. Sci. 24 (2001) 331.
[35] I. Ali, H.Y. Aboul-Enein, Intern. J. Envrion. Anal. Chem. 81 (2001) 315.
[36] A. Tanabe, K. Kawata, Anal. Sci. 20 (2004) 227.
[37] S.-D. Huang, H.-I. Huang, Y.-H. Sung, Talanta 64 (2004) 887.

[38] M.S. Dopico G, M.V. Gonzalez R, J.M. Castro R, E. Gonzalez S, J. Perez I, M. Rodriguez T, A. Calleja, J.M.L. Vilarino, Talanta 59 (2003) 561.
[39] A.C. Borba da Cunha, M.J. Lopez de Alda, D. Barcelo, T.M. Pizzolato, J.H. dos Santos, Anal. Bioanal. Chem. 378 (2004) 940.
[40] R. Tajuddin, R.M. Smith, J. Chromatogr. A 1084 (2005) 194.
[41] M.S. Dopico, M.V. Gonzalez, J.M. Castro, E. Gonzalez, J. Perez, M. Rodriguez, A. Calleja, J. Chromatogr. Sci. 40 (2002) 523.
[42] M.E. Leon-Gonzalez, L.V. Perez-Arribas, L.M. Polo Diez, C. Panis, M.P. San Andres, Anal. Chim. Acta 445 (2001) 29.
[43] B.A. Buchholz, E. Fultz, K.W. Haack, J.S. Vogel, S.D. Gilman, S.J. Gee, B.D. Hammock, X. Hui, R.C. Wester, H.I. Maibach, Anal. Chem. 71 (1999) 3519.
[44] P. Schmitt, A.W. Garrison, D. Freitag, A. Kettrup, J. Chromatogr. A 723 (1996) 169.
[45] N.M.J. Vermeulen, Z. Apostolides, D.J.J. Potgieter, P.C. Nel, N.S.H. Smit, J. Chromatogr. 240 (1982) 247.
[46] J.H. Knox, B. Kaur, G.R. Millward, J. Chromatogr. 352 (1986) 3.
[47] T.E. Corporation, 2005.
[48] S. Espinosa, E. Bosch, M. Roses, Anal. Chem. 74 (2002) 3809.
[49] S. Espinosa, E. Bosch, M. Roses, Anal. Chim. Acta 454 (2002) 157.
[50] S. Espinosa, E. Bosch, M. Roses, J. Chromatogr. A 964 (2002) 55.
[51] X. Subirats, E. Bosch, M. Roses, J. Chromatogr. A 1059 (2004) 33.
[52] Supelco, The Reporter 19.2 (2001) 1.
[53] M. Roses, J. Chromatogr. A 1037 (2004) 283.
[54] C.F. Poole, The Essence of Chromatography, Elsevier, Boston, 2003.
[55] V. Pacakova, K. Stulik, M. Prihoda, J. Chromatogr. 442 (1988) 147.
[56] J.B. Weber, Spectrochim. Acta 23A (1967) 458.
[57] C. Horvath, W. Melander, I. Molnar, Anal. Chem. 49 (1977) 142.

FIGURES

Fig. 1. Schematic of EMLC column

Table 1
s-Triazine analyte names, acronyms, structures, and pKa values along with the corresponding equilibrium.

Fig. 2. Separation of standard triazine mixture with mobile phase at pH 2 (phosphate buffer). Flow rate 0.4 mL/min with 0.1 M LiClO4, 70% acetonitrile, 30% water mobile phase. Potential applied versus Ag/AgCl sat'd NaCl with λ_{det} at 220 nm. Analyte concentrations are 25 μM with 5-μL injection volume.

Fig. 3. Separation of standard triazine mixture with mobile phase at pH 2 (phosphate buffer), pH 4 (acetate buffer), and pH 9 (borate buffer). Experimental conditions same as Figure 2 and N=3 for each data point.

Fig. 4. Separation of standard triazine mixture with mobile phase at pH 4 (acetate buffer). Experimental conditions same as Figure 2 but λ_{det} at 230 nm.

Fig. 5. Effect of changing mobile phase pH on the retention of ametryn with the natural log of capacity factor versus applied potential for pH 1.8 (phosphate buffer), pH 2.6 and 3.9 (acetate buffer), and pH 9.2 (borate buffer). Other conditions same as Figure 2.

Fig. 6. Slope from natural log of capacity factor versus applied potential (Figure 5) for ametryn. Smooth curve through these points crosses x-axis at pH ~4.1.

Fig. 7. Separation of standard triazine mixture with no pH control. Experimental conditions same as Figure 2. Elution order for separations at E_{app} of -200 through -600 mV is: PO, PZ, PY, TY, AZ, AY, and SZ.

Fig. 1.

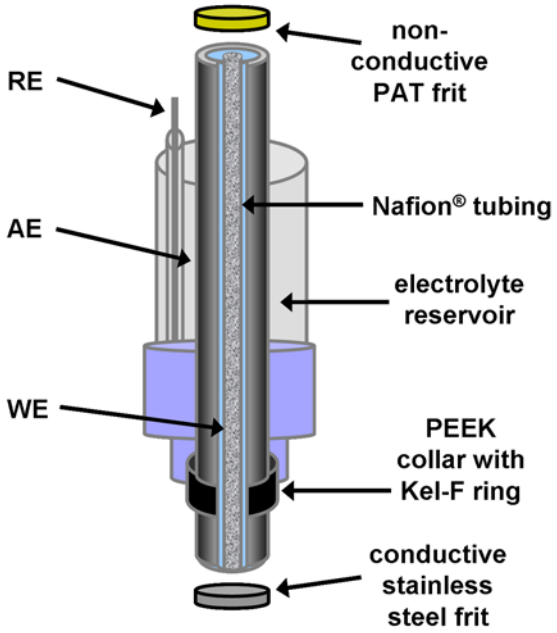

Table 1

Analyte	Acronym	R_1	R_2	X	pK_a*
Ametryn	AY	A	B	SCH_3	4.0-4.1
Atrazine	AZ	A	B	Cl	1.68-1.85
Prometon	PO	B	B	OCH_3	4.2-4.3
Prometryn	PY	B	B	SCH_3	4.05-4.1
Propazine	PZ	B	B	Cl	1.5-1.85
Simazine	SZ	A	A	Cl	1.65-1.8
Terbutryn	TY	A	C	SCH_3	4.4

A is CH_2CH_3; **B** is $CH(CH_3)_2$; **C** is $C(CH_3)_3$
* pK_a values from Ref. 44, 45, 55, 56

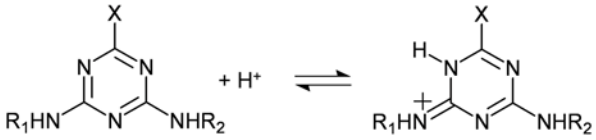

Fig. 2.

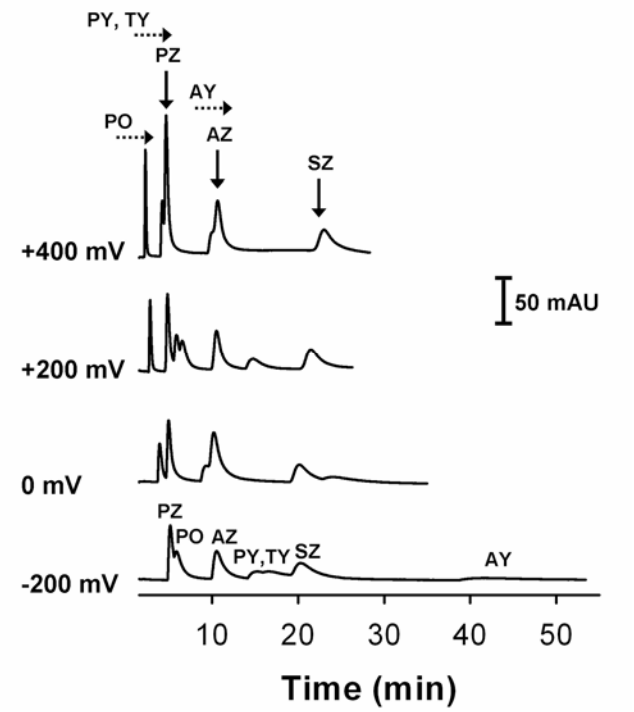

Fig. 3.

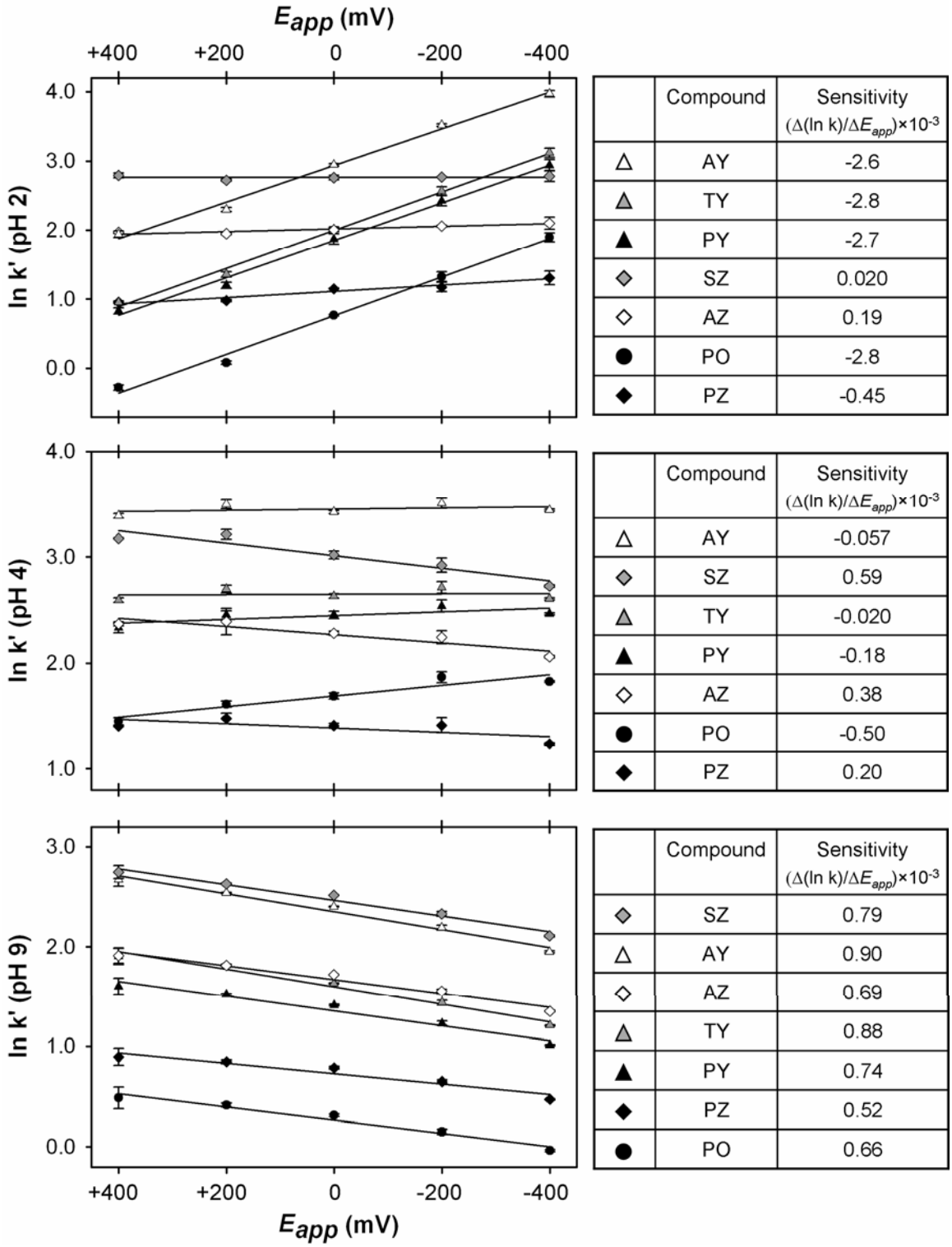

	Compound	Sensitivity ($\Delta(\ln k)/\Delta E_{app}$)×10^{-3}
△	AY	-2.6
◬	TY	-2.8
▲	PY	-2.7
◈	SZ	0.020
◇	AZ	0.19
●	PO	-2.8
◆	PZ	-0.45

	Compound	Sensitivity ($\Delta(\ln k)/\Delta E_{app}$)×10^{-3}
△	AY	-0.057
◈	SZ	0.59
◬	TY	-0.020
▲	PY	-0.18
◇	AZ	0.38
●	PO	-0.50
◆	PZ	0.20

	Compound	Sensitivity ($\Delta(\ln k)/\Delta E_{app}$)×10^{-3}
◈	SZ	0.79
△	AY	0.90
◇	AZ	0.69
◬	TY	0.88
▲	PY	0.74
◆	PZ	0.52
●	PO	0.66

Fig. 4.

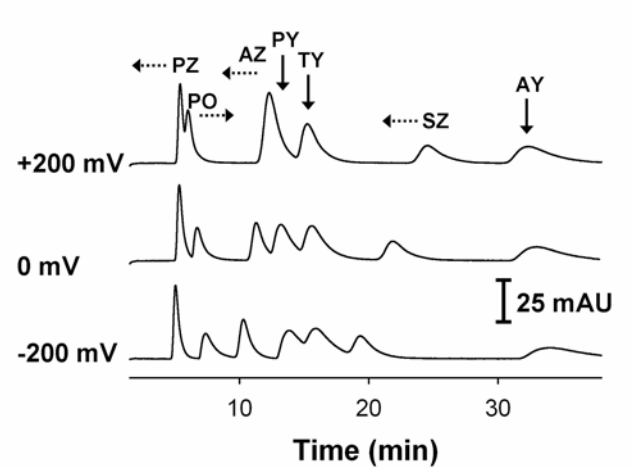

Fig. 5.

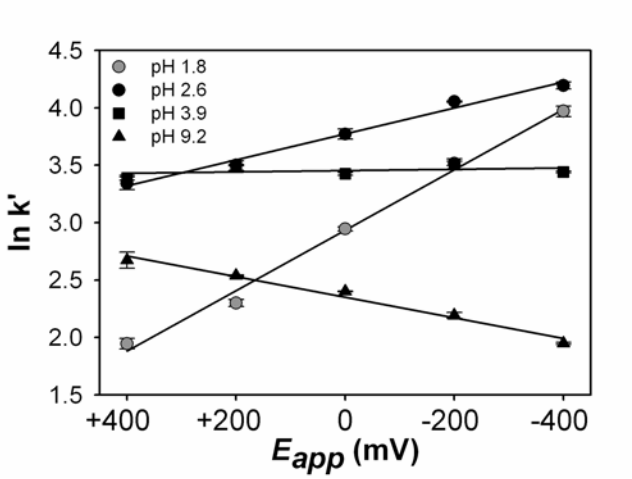

Fig. 6.

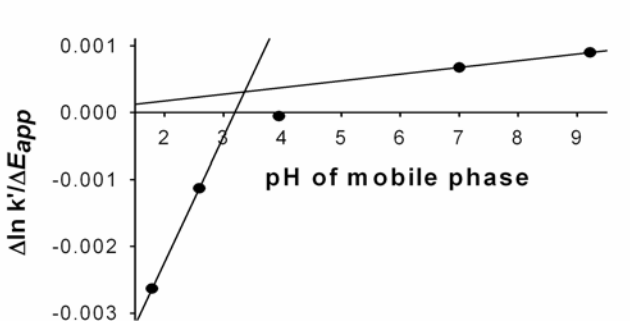

Fig. 7.

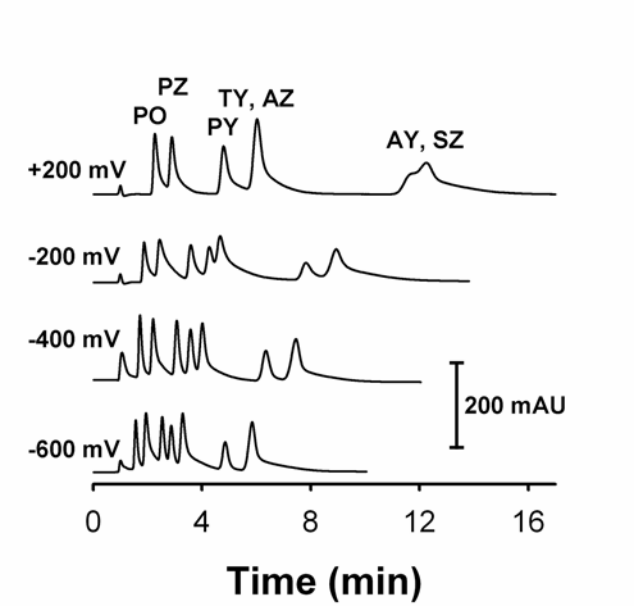

CHAPTER 6: Conclusions

This dissertation focused on research aimed at advancing two analytical techniques. Chapter 1 gave a general introduction to detection techniques for bacteria as well as an overview of Raman spectroscopy and instrumentation. Work to improve heterogeneous immunoassays that rely on surface-enhanced Raman scattering (SERS) readout was the focus of Chapters 2-4 while electrochemically modulated liquid chromatography (EMLC) method development and applications were investigated in Chapter 5 and the Appendix.

Advances in SERS readout immunoassays. The first body of work focused on the modification of a SERS-based sandwich immunoassay, previously developed in our group, in order to detect *Mycobacterium avium* subspecies *paratuberculosis* (MAP). This bacterium is the etiological agent of Johne's disease and is responsible for large economic losses in the cattle industry. Current diagnostic measures, however, do not adequately detect the bacteria and many are not readily field deployable, and thus timely implementation of counteractions to control the spread of disease is not possible. To improve upon current transduction methods, a SERS readout assay for the detection of MAP was developed and discussed in Chapters 2 and 3.

Chapter 2 focused on optimizing the current immunoassay with attention on antibody selection and blocking buffer conditions. Results for the K-10 MAP sonicate showed levels of detection (LOD) on the order of 1500 ng/mL which translated to ~750 MAP/mL. This assay was extended to the corresponding heat-killed, whole cell bacteria in Chapter 3 and had a LOD of ~500 MAP/mL. An interesting discovery revealed during the course of this investigation was the possibility of protein shedding from the surface of a bacterium cell. When viewed as an internal amplification mechanism, this development holds the potential

for improvements in LODs in other bacterial assays. The limits of detection achieved by these sensors, as well as the specificity and quantitative nature of the method, will allow for earlier diagnosis of infection and enhanced tracking of disease progression.

As a pathway to achieving improved limits of detection, methods to increase the signal intensity from our extrinsic Raman labels (*ERL*s) were investigated in Chapter 4. Research has shown that when a molecule has an electronic band in tune with the excitation laser wavelength, the scattering probability is increased and thus the Raman signal intensity also increases. Based on this, research was conducted on incorporating commercially available dyes (resonant molecules) into the *ERL*s. One of the major challenges in this work centered on maintaining the stability of the colloidal suspension during incorporation of the resonant molecules. Through adjusting the nanoparticle labeling protocol, a stable colloidal suspension was achieved. When the new *ERL*s were used in the SERS readout immunoassay, signals for the resonant Raman labels were ~300 times more intense than their nonresonant counterpart. However, improved limits of detection were not realized in this study, as the blank signals used to calculate the LOD were dominated by nonspecific binding.

Investigations of EMLC mobile and stationary phases. The second portion of this dissertation described advances made to EMLC. This analytical tool combines liquid chromatographic methods with potential control of the stationary phase. To further advance this technique, methods to implement pH modified mobile phases into EMLC were discussed in Chapter 5. By performing separations under different pH conditions, changes in elution order could possibly be achieved. To investigate this, seven triazine herbicides that are potentially hazardous to humans and the environment were utilized, as the pK_a values of these molecules are dominated by their individual substituents. As such, this class of

compounds was used to model pH control in EMLC, and equilibrium considerations were discussed. An interesting outcome of this research was the elucidation of "pulling apart" a chromatogram. That is to say, when potential was changed two previously coeluting compounds could be separated as one analyte had a decrease and one had an increase in elution time. This unique aspect of EMLC could allow for improved separations of structurally similar compounds.

Finally, the Appendix briefly discussed the integration of novel, monolithic stationary phases into EMLC. The column was redesigned and preliminary studies were performed with porous, rod-like stationary phases. While these investigations did not lead to improvements in the current system, the results have allowed a redirection in the focus of EMLC column construction and synthesis of monolithic phases for EMLC.

APPENDIX. Monolithic Carbon as a Novel Stationary Phase for Electrochemically Modulated Liquid Chromatography

Betsy Jean Yakes and Marc D. Porter

INTRODUCTION

Stationary phase development in liquid chromatography is essential for improvements in chromatographic performance. Traditional, particulate packed phases are limited by large void volumes, slow mass transfer of large molecules, or high back pressure.[1] To improve upon these limitations, an exciting new area of study focuses on transitioning from slurry packed materials to contiguous foam-like phases.[2] While multiple names exist to describe these materials, the term monolith, stemming from the Greek μονολιτηοσ for single (μονο) stone (λιτηοσ), has become the most widely accepted.[3] The fused design of these materials yields both high permeability and high efficiency while also having low resistance to fluid flow. An additional attribute, which could be advantageous with electrochemically modulated liquid chromatography (EMLC), is that monolithic phases may lead to a lower solution resistance and, with more consistent pore size, more uniform resistance across the column.

Monoliths are generally classified as polymer- or silica-based and are further grouped by the derivatives used during synthesis or any subsequent surface modification. There are a diversity of pathways for the preparation of these phases with hydrogels, polyurethane foams, compressed beads, thin disks, and rigid columns being the most popular formats.[3] Unlike polymer- and silica-based materials, purely carbon monolithic stationary phases (i.e., monolithic carbon, MC) have been introduced only recently. These monoliths are generally

synthesized by using a silica template and a carbon precursor.[4-8] After the precursor is carbonized under non-oxidizing conditions, the silica framework is dissolved. Since the shape of the MC is based solely upon the silica template and the surrounding support, the rod length, width, shape, and internal pore diameter can be tailored to suit many column designs. One such carbon monolith by Guiochon and coworkers is formed through high-temperature graphitization of a phenolic resin rod with embedded sacrificial silica beads. The resulting porous rod consists of a bridged framework of highly ordered carbon with both micro- and mesopores.[5] With the goal of exploring the benefits of MC, we investigated this and similar monolithic columns, in collaboration with Guiochon and coworkers, with our EMLC system.

EMLC, as introduced in Chapter 5, is a unique combination of liquid chromatography and electrochemistry. In EMLC, analyte retention is manipulated by changing the potential applied (E_{app}) to a conductive stationary phase such as porous graphitic carbon (PGC). While MC is a conductive material like PGC, its structure provides a packing with more regular channels than slurry packed columns, yielding a lower level of axial dispersion and potentially improved separations. The focus of this appendix is on attempts to assess the potential of these MC stationary phases in EMLC. This report is intended to serve as a record of the research, with experimental conditions and prospective studies as guidelines for future investigations.

GLASSY CARBON PARTICULATE ROD

Our first attempt at incorporating monoliths as stationary phases used a preformed particulate rod synthesized through phase separation procedures. This fused material was similar to, but easier to synthesize than, a skeletal monolithic rod and functioned as a good

mechanical model for use in redesigning the column. SEM images of this rod, shown in Figure 1, indicated that the material was composed of clusters of ~1-μm beads that were stacked together. These rods were composed of ungraphitized, glassy carbon and had a surface area of ~200 m^2/g, determined by BET measurements (C. Liang and S. Dai, Oak Ridge National Laboratory). In addition, their studies showed chromatographic performance with this material was poor due to micropores in the particle surface (unpublished data). To improve performance, the number of micropores can be decreased through graphitization or surface modification. For the scope of this investigation, this rod was used as a model for redesigning the column; however, since the material was not capped, the rod was not extensively used for separations.

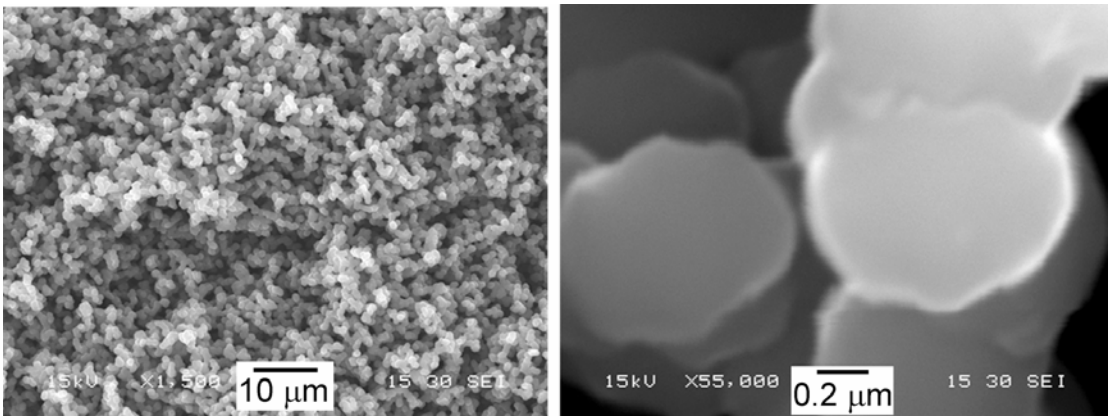

Figure 1. Glassy carbon rod SEM images.

REDESIGNED EMLC COLUMN

The standard EMLC column and HPLC instrumentation have been detailed in Chapter 5. This basic column[9] format, having been optimized for slurry packing particulate stationary phases, required redesign for incorporation of the MC rods. In the traditional EMLC column, a stationary phase is packed into a porous stainless steel column housing that

has been lined with a Nafion cation exchange membrane. The conductive stationary phase serves as the working electrode (WE), while the Nafion tubing functions as the salt bridge and electronic insulator between the working and auxiliary electrodes. The porous stainless steel provides the structural support for the column and provides the high surface area auxiliary electrode (AE). To complete the three electrode electrochemical cell, a silver/silver chloride (saturated sodium chloride) reference electrode (RE) is placed in an external electrolyte reservoir. This setup of building the column from the outside-in, however, was not readily amenable to use with preformed rods. As such, the standard EMLC column needed to be rebuilt from the inside-out. Throughout the alteration process, efforts were made to ensure the column housing remained as close as possible to the traditional setup so that comparisons between the monolithic phases and PGC could be made.

The first step in modifying the column was machining the stainless steel housing. In this case, the rods encapsulated with Nafion were a larger diameter (~3.8 mm) than the column body (3.2-mm internal diameter, i.d.), so the stainless steel was bored out to a ~3.9-mm i.d. with the 11-cm length maintained. Next, one end of the Nafion tubing that encases the stationary phase was flanged. After flanging, a wooden rod was inserted into the tubing, and the Nafion tubing was completely immersed in isopropanol. This process maintained the shape of the tubing while swelling the polymer to make it more pliable. Once this occurred, the wooden rods were removed, and the monolithic rod was

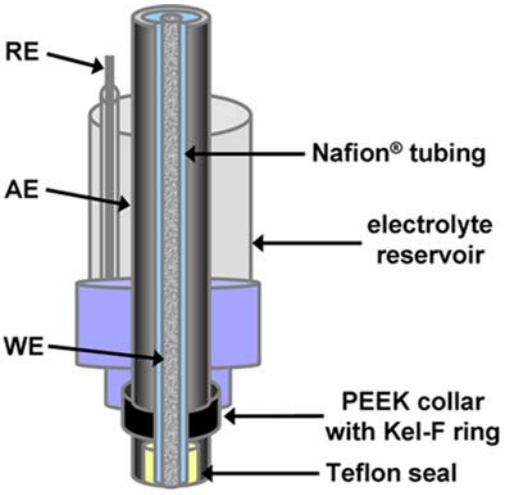

Figure 2. Modified EMLC column

inserted into the Nafion tubing. This procedure was done by manually sliding/twisting Nafion tubing over the rod while continuously wetting the Nafion/rod structure with isopropanol to decrease friction. During this process, special care was taken to ensure the Nafion tubing did not wrinkle and that the flange was not distorted. When the top of the rod was flush with the flange, the assembly was dried (2 h, room temperature), placed in the column body, and the nonflanged end of the Nafion/rod cut flush with the end of the column. To form a seal at the bottom of the column, a flange was formed from heat-shrink Teflon, inserted between the Nafion tubing and stainless steel, and then heated to form a seal. The finalized column, shown schematically in Figure 2, was fitted with standard frits and end fittings and attached to the HPLC instrumentation and potentiostat as described in Chapter 5.

Results from experiments with this rod indicated that the material was a poor chromatographic stationary phase as expected based on the unblocked micropores. When using a 100 mM lithium perchlorate, 95% water, 5% acetonitrile mobile phase at a flow rate of 1.0 mL/min, the backpressure was only 30 bar. In addition, injections of acetonitrile and benzene sulfonate had the same elution times as shown in Figure 3. These results indicated that the analytes did not sufficiently interact with stationary phase. Based on this, further separations were not performed with this material. However, the EMLC column modification did allow for incorporation of the rod, so skeletal monoliths were tested next.

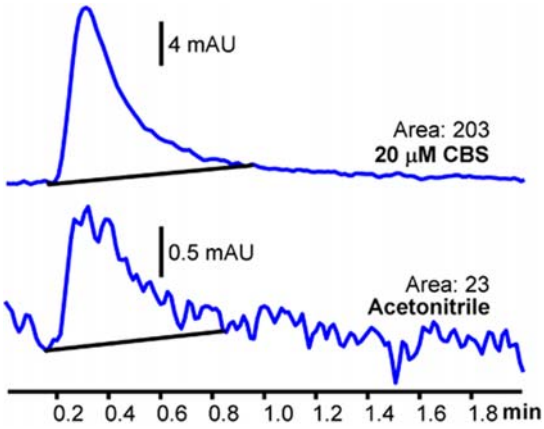

Figure 3. Experiments with glassy carbon rod.

MONOLITHIC CARBON

The MC rod used for separation studies is shown in the SEM images in Figure 4. SEM images illustrated the skeletal structure (Figure 4a and 4c) as well as the mesoporous features observed with a lower accelerating voltage (Figure 4b). Characterization of this material by Raman spectroscopy (Figure 4d) gave two broad bands. The lower energy band is attributed to carbon disorder and is characteristic of nongraphitic carbon; however, the presence of the E_{2g} breathing mode at 1526 cm^{-1} indicates a degree of microcrystallinity.[10] This conductive material was inserted into the redesigned EMLC column and separations were performed with a mixture of aromatic sulfonates. As shown in Figure 5a, the analytes had no detectable retention and appeared to coelute with the void volume. In addition, at the flow rate of 1 mL/min, the back pressure was only 45 bar, and the void volume was calculated to be ~0.3 mL. This situation may reflect gaps between the Nafion and stationary phase, creating a low resistance flow path for the mobile phase that would allow the analyte to flow past the stationary phase. In addition, this material was nongraphitized and contained micropores similar to the glassy carbon, particulate rod. As mentioned above, these micropores lead to poor chromatographic efficiency but can be capped by either graphitization or surface modification; however, these procedures were not preformed within the scope of this investigation.

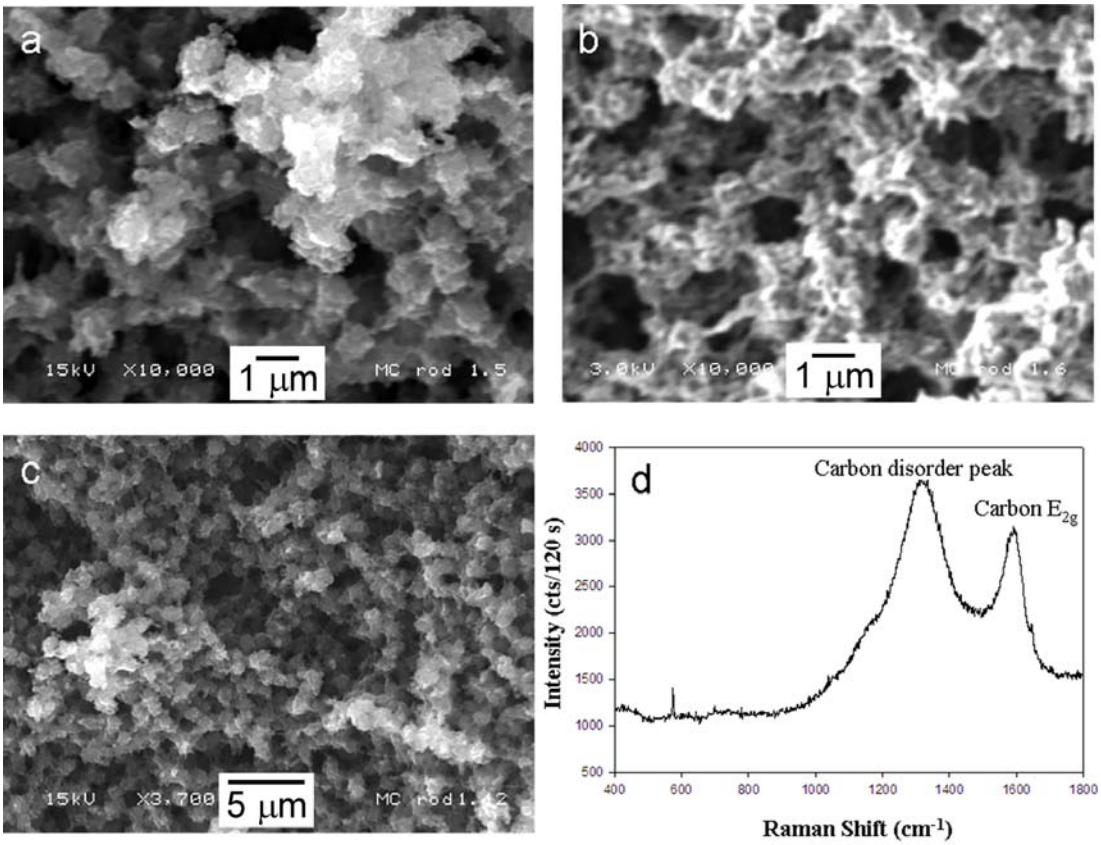

Figure 4. SEM images and Raman spectrum of nongraphitic, monolithic carbon rod.

Another possible explanation of the lack of retention is the complete adsorption of the analytes to the stationary phase. To test this hypothesis, experiments were performed with varying concentrations of benzene sulfonate. The only elution band found was at the void volume. In addition, as shown in Figure 5b, the area under the elution band tracked linearly with the benzene sulfonate concentration, supporting the premise of the analyte eluting in the void band. This result points to either gaps between the stationary phase and Nafion/column housing and/or the existence of micropores as the complication. The presence of gaps has been the primary challenge in integrating monolithic materials into chromatography, but could be overcome by monolith formation in-situ and the subsequent covalent bonding of the monolith to the support (e.g., column housing).[11] For the possibility of micropores hindering

retention, this would be best overcome by graphitizing the carbon surface, as surface modification could interfere with the conductivity of the carbon surface.

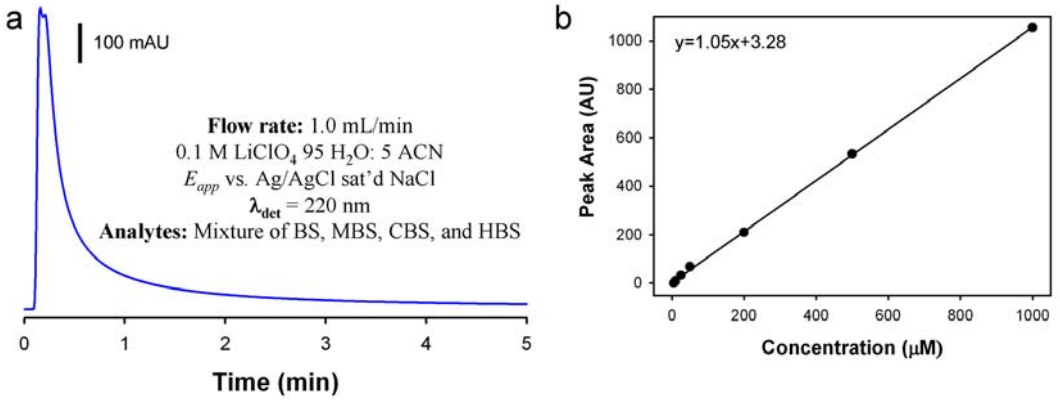

Figure 5: (a) Separation with a mixture of benzene sulfonate (BS), methyl- (MBS), chloro-BS (CBS), and hydroxy-BS (HBS), each 20 μM. **(b)** BS injects at varying concentrations and corresponding peak area at ~0.3 min (other conditions in **a**).

FUTURE DIRECTIONS

As these initial studies show, redesigning our traditional EMLC column to incorporate rod stationary phases did not readily result in a functioning chromatographic system. The main challenges to this approach included chipping or cracking the rod during insertion into the Nafion tubing and ensuring that there were no gaps between the monolith and Nafion membrane. There are two avenues to potentially mitigate these difficulties. The first path addresses a dramatic column redesign that would not only allow simpler encapsulation, versus insertion, of preformed stationary phases but also include a completely enclosed electrolyte reservoir. The self-contained electrolyte reservoir will also enable easier column integration (e.g., incorporation into standard HPLC column compartments) and use in high temperature environments with limited evaporation of electrolyte. The second area takes advantage of monolith stationary phase formation and will focus on developing

methods for synthesizing carbon monoliths within the Nafion, or similar, encasings. Such an approach would potentially avoid the formation of gaps possibly encountered during this study. In addition, since micropores may have limited the chromatographic ability of the rods used herein, the next generation of monolithic materials should be graphitized.

REFERENCES

(1) Svec, F.; Huber, C. G. *Anal. Chem.* **2006**, *78*, 2100-2108.
(2) Belenkii, B. G. *Russ. J. Bioorg. Chem.* **2006**, *32*, 323-332.
(3) Svec, F.; Tennikova, T. B.; Deyl, Z., Eds. *Monolithic Materials: Preparation, Properties and Applications*; Elsevier: Amersterdam, 2003.
(4) Kruk, M.; Dufour, B.; Celer, E. B.; Kowalewski, T.; Jaroniec, M.; Matyjaszewski, K. *J. Phys. Chem. B* **2005**, *109*, 9216-9225.
(5) Liang, C.; Dai, S.; Guiochon, G. *Anal. Chem.* **2003**, *75*, 4904-4912.
(6) Lu, A.-H.; Smatt, J.-H.; Backlund, S.; Linden, M. *Microporous Mesoporous Mater.* **2004**, *72*, 59-65.
(7) Shi, Z.-G.; Feng, Y.-Q.; Xu, L.; Da, S.-L.; Liu, Y. *Mater. Chem. Phys.* **2006**, *97*, 472-475.
(8) Taguchi, A.; Smatt, J.-H.; Linden, M. *Adv. Mater.* **2003**, *15*, 1209-1211.
(9) Ting, E.-Y.; Porter, M. D. *Anal. Chem.* **1998**, *70*, 94-99.
(10) Tuinstra, F.; Koenig, J. L. *J. Chem. Phys.* **1970**, *53*, 1126-1130.
(11) Jacoby, M. In *Chemical and Engineering News*, 2006; Vol. 84, pp 14-19.